Title
Exciton-Phonon Interactions in Complex Materials

Author
Haber, Jonah

Publication Date
2022

Exciton-Phonon Interactions in Complex Materials

By

Jonah Haber

A dissertation submitted in partial satisfaction of the

requirements for the degree of

Doctor of Philosophy

in

Physics

in the

Graduate Division

of the

University of California, Berkeley

Committee in charge:

Professor Jeffrey B. Neaton, Chair
Professor Steven G. Louie
Professor David Limmer

Summer 2022

Exciton-Phonon Interactions in Complex Materials

Abstract

Exciton-Phonon Interactions in Complex Materials

by

Jonah Haber

Doctor of Philosophy in Physics

University of California, Berkeley

Professor Jeffrey B. Neaton, Chair

The interaction between excitons and phonons is fundamental to the nature and fate of photoexcitatons in solids, with important implications for spectroscopy and transport measurements, and for applications in optoelectronics and clean energy. In this dissertation, we present recent advances in computing exciton-phonon interactions from first principles. We implement a recently proposed linear-response reciprocal space-based framework which involves contracting electron-phonon matrix elements computed from density functional perturbation theory (DFPT) with exciton expansion coefficients obtained after building and diagonalizing the *ab initio* Bethe-Salpeter Hamiltonian, which is built on density functional theory and the GW approximation. We apply this formalism in unique ways to study phenomena related to exciton-phonon interactions, namely the nature of exciton diffusion in acene crystals, the dynamical screening of excitons in halide perovskites due to lattice vibrations, and the asymmetric lineshapes in MoS_2 stemming from off-diagonal exciton-phonon coupling.

For my father Alan, and in memory of my mother Marian,
for all their help and support along the way.

Contents

List of Figures

List of Tables

Acknowledgments

First and foremost, I'd like to thank my advisor, Jeff Neaton, for his wisdom, guidance, extreme patience, and endless support over the course of my Ph.D. The breadth and depth of your scientific knowledge and curiosity is inspirational. I marvel at your ability to conduct world-class research while simultaneously fostering an inclusive and collaborative research environment. The academic freedom you have given me to pursue my own ideas, at my own pace, has given me the room to grow into the scientist I am today. It is rare to find a mentor who is as compassionate and genuinely interested in the well-being and success of his students as you are. I count myself fortunate to have stumbled into your group. Academia would undoubtedly be a better place with more PIs like you. Thank you for the example you set.

I'd like to thank my many collaborators. I am especially grateful to: Prof. Steven Louie, for both giving an excellent introductory course on condensed matter physics and for many fruitful discussions with him and his students over the years; Prof. Leeor Kronik, for his kindness and for sharing his deep knowledge of all things DFT as well as hosting me on several occasions at the Weizmann Institute; and Prof. Naomi Ginsberg for her insights, encouragement, and her help in connecting theory with experiment.

A special thanks to my mentors: Sivan Refaely-Abramson, for helping me take my first steps in research, many pep-talks over the years, and her infectious spirit and passion for the work we do; Felipe da Jornada, for selflessly sharing his broad scientific and technical insights, often in a humorous manner, and for giving me a home at Stanford in recent months; and Gab Antonius for teaching me about phonons and sharing his work on exciton-phonon interactions, which ultimately served as the catalyst for this dissertation.

Special thanks also to: Sophie Weber, for being the new kid on the block with me, for her dry sense of humor, and for her ability to consistently down a pint of beer before I've managed to start my own; Marina Filip, for many joyful hours spent discussing physics together, for generously sharing her knowledge and work with me, and for the many excursions with her and Tony to Santa Cruz, Napa, and beyond when we needed a break from physics; Liz Peterson, for encouraging my literary pursuits (notably Jane Austin), for trusting me to officiate her wedding, and for being a near and dear friend whom I can always count on to empathize with me when I share my troubles; Stephanie Mack, for sharing valuable advice as an older graduate student, for the happiness she brought to all in the lab, and for the playfully teasing when I needed to be taken down a peg or two; Aurelie Champagne, for many productive scientific discussions and for the joyful spirit which she brings to work daily; and finally Antonios Alvertis, for his scientific insight on all things phonon related, his last minute help editing this dissertation, and his impeccable sense of style.

There are many others who have passed through the Neaton (and Louie) group who have profoundly shaped my graduate school experience, and I wish to thank them by name here. In no particular order: Tonatiuh Rangel, Linn Leppert, Se Young Park, Tess Smidt, Zhenfei Liu, Sinead Griffin, Jun-Hoon Lee, Florian Altvater-Brown, Samia Hamed, Chenchen Song, Caroline McKeon, Sijia Ke, Eric Taw, Alex Smith, Tyler Reichanadter, Vish Ravi, Armin

Eghdami, Ella Banyas, Stephen Gant, Yusuf Shaidu, Fancisca Sagredo, Fancesco Ricci, Diana Qiu, Mit Naik, Zhenglu Li, and Yang-Hao Chen.

To the incredible administrative staff, Meg Holm, Marisa Davis, and Arica Chhay, thank you for going above and beyond your duties, and cheering me on at all major milestones. Special thanks to Marisa Davis, for helping me whenever I messed up a form or missed a deadline, and for repeatedly reminding me to record my work hours so that I was paid throughout graduate school.

And to friends outside the Neaton group. Thanks to Sam Watkins for running with me in the morning, "tuna-sammy's" on Wednesdays, and reminding me that no matter how old you get, you are never too old to shotgun a beer. To Robert McGehee, thanks for your general goofiness, for dragging me to the gym in the early days of grad school, and for the many dinners with you Carol, Ada (potata), and Hugo in the later years. To Noman Paya, thank you for schlepping up and down the bay to hang, for organizing the annual Tahoe trip, and for grabbing Sunday brunch with me at La Note more than a few times.

To my very new and very special friend Lillian. Without you the last 6 months would have been a drag. Thank you for welcoming me into your life and supporting me and my work even as I fail miserably to explain what it is I actually do. And thank you for waiting until after I finished the first draft of this thesis to share Covid with me. There is no one I would rather spend ten days in isolation with during the waning moments of my Ph.D.

To my "OG" siblings, Leora, Gideon, and Rafael. You already know I love you guys but I'd be in so much trouble if I didn't publicly acknowledge it here. Thank you for the phone calls (because you know the oldest brother never initiates the call) and many visits to Berkeley. As I finish this chapter I am proud not only of what I have accomplished but also what each of you have accomplished over the same period of time. Lets just say there are a couple doctors in the Haber family these days. Thank you to my step-mom and my littlest sisters who graciously welcomed me back home for 15 months during a global pandemic. Sara, thank you for your support, advice, and willingness to commiserate with me about all things academia over a bottle of wine. Hannah and Rachel thank you for putting up with a very weird and much older brother.

And finally to my parents Alan and Marian. In one way or another this work is a byproduct of everyone mentioned above but you two have played the largest role. As a child who needed more than a little help getting started in school, you worked tirelessly to make sure I had the tools I needed to succeed. Since then, you've always encouraged me to follow my dreams, rooting for me at every step along the way. Thank you for your love and support. I dedicate this dissertation to you.

Chapter 1

Introduction

Condensed matter physics is the study of emergent properties and phases which arise in systems of many interacting particles, e.g. solids, liquids, etc. For a large class of physical systems it is possible to reduce the problem of many strongly interacting constituents to a theory of weakly interacting quasiparticles and collective excitations [1]. Often these quasiparticles behave much like their non-interacting (bare) counterparts but with altered (renormalized) physical properties. In other instances the quasiparticle may have no bare counterpart and their existence is intimately tied to the many-electron system in which it lives.

This thesis is centered on the interaction between a specific quasiparticle and collective excitation: the exciton and phonon. The former can be thought of as a bound electron-hole pair, and often dominates the low energy optical response of semiconducting materials manifesting physically as resonances in the absorption spectra [2]. The latter is a quantized lattice vibration and in contrast to the exciton involves the collective motion of all ions in the system [3].

The exciton concept was established nearly 100 years ago with models of Mott/Wannier [4, 5] and Frenkel [6], which describe excitons in the weakly- and strongly-bound limit, respectively. Today these models serve as useful touchstones for understanding optical excitations at lowest order. At the same time they are understood to be phenomenological descriptions appropriate only in extreme limits and often fail to give quantitative results in real materials. This failure is especially palpable in complex materials, e.g. low-dimensional transition metal dichalcogenides [7], organic semiconductors [8], and lead-based halide perovskites [9], all of which show great promise for next generation optoelectronic applications. As these materials exhibit a large degree of structural and chemical heterogeneity, it is unsurprising that they support a variety of excitons and the need for a predictive framework flexible enough to describe excitons across a diverse set of materials is self-evident.

Over the last two decades, computational excited state methods have established themselves as robust tools for accurately describing excitonic properties across a wide range of complex materials including the set given above [10]. The GW method, where G is the Green's function and W the screened Coulomb interaction, and Bethe-Salpeter equation approach [11, 12], grounded in many-body perturbation theory (MBPT), has proven to be particularly successful in this regard. At the time of writing this dissertation, computational capabilities have matured to the point where many static properties such as the exciton binding energy and optical absorption spectra are readily computed for systems with hundreds of electrons using standard codes such as BerkeleyGW [13]. In this sense, the time is ripe to move beyond calculations of static excitonic properties and turn towards dynamics. This venture starts with a careful study of interactions between exciton and other fundamental particles. While many such interactions exist, e.g. exciton-exciton, exciton-electron, exciton-photon (polariton), etc. [14], perhaps the most relevant for understanding exciton dynamics is the exciton-phonon interaction [15]. The interaction between excitons and phonons is fundamental to the nature and fate of photoexcitatons in solids, with important implications for spectroscopy and transport measurements, and for applications in optoelectronics and clean energy. While there exists a relatively mature framework for computing electron-phonon interactions and derived properties including transport coefficients, spectral functions, and superconducting critical temperatures [16], similar computational methodologies for computing exciton-phonon interactions are only now just beginning to become available and the consequence of such interactions have not yet been fully explored in a first principle context.

Further, from the early work of Toyozawa [15] at the model Hamiltonain level, we expect this coupling to be fundamentally different from either electron-phonon or hole-phonon coupling due to the correlated nature of the exciton which in turn gives rise to non-trivial correlation effects between the electron and hole channels. One of the most striking examples of this is a phenomenon which we refer to as polaron interference [17, 18]. Here, the polaron clouds associated with a bound electron-hole pair overlap and partially cancel with sometimes drastic consequences for the exciton binding energy even in “simple” semiconductors. We will elaborate more on this in Chap. 5.

In this dissertation we detail our work to both (i) extend first principles methodology to study exciton-phonon interactions in complex materials and (ii) apply our formalism in novel ways to complex systems to both rationalize existing experimental findings and predict new phenomena. This dissertation is organized as follows.

In Chap. 2, we review the relevant parts of electronic structure theory we require for the rest of the dissertation devoting special attention to the Bethe-Salpeter equation approach for computing exciton energies and coefficients and density functional perturbation theory for computing electron-phonon matrix elements, two critical ingredients for constructing the exciton-phonon matrix element [19].

Chapter 3 focuses on a novel scheme we developed for constructing a maximally-localized Wannier function representation of the exciton. In essence, this work is a generalization of the usual maximally localized Wannier scheme for single particle excitations [20]. While not directly related to exciton-phonon coupling, this work sets the stage for Chap. 4 where we require a localized basis for studying phonon based exciton hopping. Further, as discussed in more detail at the end of this chapter, this formalism has direct consequences for the efficient interpolation of the exciton-phonon matrix element throughout the Brillouin zone in a manner analogous to what is done at the electron-phonon level [16].

In Chap. 4, we put forward an *ab initio* framework for predictive calculations of exciton diffusion coefficients in the weak and strong exciton-phonon coupling limits. In the latter limit, we generalize the Lang-Firsov [21] transformation to the multi-band case, introducing gauge freedom into the formalism. We fix this gauge freedom using the maximally localized Wannier technology developed in the previous chapter. We use this framework to predict exciton-polaron energies and exciton diffusion coefficients of low-lying spin triplets in the organic semiconductors naphthalene, anthracene, tetracene, and pentacene, elucidating trends with increasing acene size. Our theory leads to phonon renormalized exciton energies and diffusion coefficients in good agreement with experiment, and illustrate the general utility of this framework.

In Chap. 5, we focus on how lattice vibrations couple to the internal structure of the exciton, extending the standard *ab initio* BSE formalism to include phonon screening effects at lowest order in the electron-phonon interaction. We introduce an additive, $\mathbf{q}$- and ω-dependent contribution to the screened Coulomb interaction, W, associated with phonons, adopting a general form developed by Hedin and Lundquist [22] but neglected in contemporary calculations. We apply this framework to a set of all-inorganic lead-halide perovskite crystals in the low temperature, orthorhombic phase using the *ab initio* Fröhlich electron-phonon vertex introduced in Ref. [23], and we show that phonon screening plays a major, but not exclusive, role in the exciton binding energies of this emergent class of optoelectronic materials. Finally, we develop a simple but general expression for the phonon-screened exciton binding energy for arbitrary isotropic semiconductors in terms of μ, ε_∞, ε_0, and ω_{LO}, providing a means for identifying semiconductors for which phonon screening effects will be significant.

In Chapter 6, we develop and apply a first-principles approach to study exciton-phonon coupling in monolayer MoS_2 and reveal the highly selective nature of exciton-phonon coupling due to the internal spin structure of excitons, which leads to a surprisingly long lifetimes of the lowest energy bright A exciton. Moreover, we show that optical absorption processes rigorously require a second-order perturbation theory approach, with photon and phonon treated on an equal footing, as proposed by Toyozawa [24]. Such a treatment, thus far neglected in first-principles studies, gives rise to off-diagonal exciton-phonon coupling matrix elements, which are critical for the description of dephasing mechanisms, and yields exciton linewidths in excellent agreement with experiment.

Chapter 2

Electronic Structure Methods

2.1 Introduction

The coupling between electronic and ionic degrees of freedom is central to many studies in this dissertation. As is such, in this section we focus primarily on aspects of electronic structure related to this interactions. After giving a high-level overview of ground and excited state theories in Sec. 2.2 and a concise summary of Kohn-Sham density functional theory and its reciprocal-space implementation in Sec. 2.3-2.4, we detail in some depth density-functional perturbation theory and its application to studying lattice dynamics and electron-phonon coupling in Sec. 2.5- 2.7. In Sec. 2.8-2.12 we turn our attention to many-body perturbation theory and common approximations used to compute renormalized eigenenergies. In the last two of these sections special attention is given to W^{ph}, the phonon contribution to the screened electron-electron interaction. This quantity will play an important role in Chap. 5. In Sec. 2.13, we discuss the Bethe-Salpeter equation formalism for computing excitonic properties and finally in Sec. 2.14 we define the exciton-phonon matrix and related it the contraction of the exciton expansion coefficients and electron-phonon matrix elements. This quantity is central to the discussion in Chap. 4 and 6.

2.2 The Many-Body Hamiltonian and Ground vs. Excited State Theories

The Hamiltonian, we concern ourselves with in condensed matter physics takes the form

$$\hat{H} = -\sum_{i} \frac{\nabla_i^2}{2} + \frac{1}{2}\sum_{i \neq j} \frac{1}{|\mathbf{r}_i - \mathbf{r}_j|} - \sum_{I} \frac{\nabla_I^2}{2M_I} + \frac{1}{2}\sum_{I \neq J} \frac{Z_I Z_J}{|\mathbf{R}_I - \mathbf{R}_J|} + \sum_{i,I} \frac{Z_I}{|\mathbf{r}_i - \mathbf{R}_I|}, \tag{2.1}$$

where $\mathbf{r}_i$ and $\mathbf{R}_I$ denote the positions of the i^{th} electron and I^{th} ion respectively while Z_I and M_I denote the effective charge and mass associated with ion I. Unless stated otherwise, we work in atomic units, $\hbar = m_e = e = 1$. As a first approximation, the nuclear coordinates are often taken to be clamped at their equilibrium positions so that the kinetic term associated with these degrees of freedom can be neglected and the nuclear positions, $\mathbf{R}_I$, can be demoted from operator to classical variable [25]. Even after these simplifying approximations, the many-body wavefunction $\Psi(\mathbf{r}_1, \mathbf{r}_2 \ldots \mathbf{r}_{N_e}; \mathbf{R}_1 \ldots \mathbf{R}_{N_i})$ is still prohibitively expensive to compute and for systems with more than ~ 10 electrons a direct solution is often infeasible.

In many, if not all practical cases, it turns out that experimentally measurable properties do not depend on the detailed motion of all particles and the entire many-body wavefunction is not required to make physical predictions. Instead it can be sufficient to focus on reduced quantities – i.e. quantities with many degrees of freedom integrated out. An important example is the ground state density, $n(\mathbf{r})$, related to the many-body wavefunction through

$$n(\mathbf{r}) = N_e \int d^3\mathbf{r}_2 \ldots d\mathbf{r}_{N_e} \Psi^\star(\mathbf{r}, \mathbf{r}_2 \ldots \mathbf{r}_{N_e}) \Psi(\mathbf{r}, \mathbf{r}_2 \ldots \mathbf{r}_{N_e}), \tag{2.2}$$

where N_e denotes the number of electrons in the system. Physically, $n(\mathbf{r})$, is the probability density to find an electron at position $\mathbf{r}$. Importantly, it was proved by Hohenberg and Kohn [26] that for a given ionic configuration, the ground state energy E is a unique functional of $n(\mathbf{r})$ – i.e. $E = E[n(\mathbf{r})]$ – so that in principle knowledge of $n(\mathbf{r})$ allows for the prediction of all ground state properties. Notably, many properties of interest are related to total energy differences, cohesive energies, lattice constants, adsorption energies, ionization energies as well as the the preferred structural and magnetic ordering of materials are all examples of properties which can be determined from differences in E. While a host of other linear response functions are related to infinitesimal changes in E in response to perturbations. Examples include the elastic constants, dynamical matrix, polarizability, Born effective charge, magnetic susceptibility and Raman tensor [27, 28].

Unsurprisingly, not all experimental observables can be easily related to total energy differences. A classic example is the quasiparticle dispersion which is a measure of particle-like excitation energies. Here one needs a different framework, one based on the single particle many-body Green's function, $G(\mathbf{r}t, \mathbf{r}'t')$. In Sec. 2.7, we will show how the poles of this object are related to excitations of the many-body system. While $G(\mathbf{r}t, \mathbf{r}'t')$ is more complex than $n(\mathbf{r})$ it is still much simpler than the many-body wavefunction for large numbers of electrons.

In light of the above discussion, it is natural to ask: is it possible to determine reduced quantities like $n(\mathbf{r})$ or $G(\mathbf{r}t; \mathbf{r}'t')$ without recourse to first solving the many-body Hamiltonian? The answer turns out to be a resounding yes (at least in theory), and this framework is used for much of the work in this thesis, and we review it in the subsequent sections.

2.3 Kohn-Sham Density Functional Theory

One year after Kohn and Hohenberg established that the ground state energy, E, of an interacting system can be expressed as a unique functional of the single particle density $n(\mathbf{r})$ [26], Kohn and Sham put forward an scheme for practical calculations [29]. Their strategy, which is still widely used today, is to map to a fictitious, non-interacting system which generates the same ground state density as the interacting system. Because the reference system is non-interacting, the wavefunction for this system can be expressed as a Slater determinant of single-particle orbitals. There are many excellent sources for deriving the Kohn-Sham (KS) equations, here we state some results [30, 31].

The Kohn-Sham equation is usually cast as an eigenvalue equation of the form

$$\left(-\frac{\nabla^2}{2} + V_{\mathrm{KS}}(\mathbf{r}) \right) \psi_i(\mathbf{r}) = \varepsilon_i \psi(\mathbf{r}), \tag{2.3}$$

where ε_i and $\psi_i(\mathbf{r})$ are the Kohn-Sham eigenenergies and orbitals respectively and $V_{\mathrm{KS}}[n](\mathbf{r})$ is the Kohn-Sham potential. The Kohn-Sham potential is in turn composed of three terms

$$V_{\mathrm{KS}}[n](\mathbf{r}) = V_{\mathrm{ion}}(\mathbf{r}) + V_{\mathrm{H}}[n](\mathbf{r}) + V_{\mathrm{xc}}[n](\mathbf{r}), \tag{2.4}$$

where the notation $[n]$ has been introduced to denote terms which depend functionally on the ground state density. The ionic contribution is determined by the position of the underlying atoms which compose the system. While the Hartree and exchange-correlation terms are defined, respectively, as

$$V_{\mathrm{H}}[n](\mathbf{r}) = \int d^3\mathbf{r}' \frac{n(\mathbf{r}')}{|\mathbf{r} - \mathbf{r}'|} \tag{2.5}$$

$$V_{\mathrm{xc}}[n](\mathbf{r}) = \frac{\delta E_{xc}[n(\mathbf{r})]}{\delta n(\mathbf{r})}, \tag{2.6}$$

where E_{xc} is the universal exchange-correlation functional. The Hartree term is familiar from electricity and magnetism and is the classical potential an electron in state i experiences due to all other electrons (and itself). By contrast the exchange correlation energy is purely quantum mechanical and is for general systems unknown. The first proposed and most well know construction of $V_{\mathrm{xc}}[n](\mathbf{r})$ relies on the local density approximation (LDA). This approximation begins with $\varepsilon^{\mathrm{HEG}}(n)$, the exchange-correlation energy per unit volume for a homogeneous electron gas (HEG) with uniform density, n, which has been accurately parameterized against Monte-Carlo simulations [32]. In the local density approximation n is promoted from a scalar to a function, $n(\mathbf{r})$, so that

$$E^{\mathrm{LDA}}_{\mathrm{xc}}[n(\mathbf{r})] = \int d^3\mathbf{r} n(\mathbf{r}) \varepsilon^{\mathrm{HEG}}(n) \bigg|_{n=n(\mathbf{r})}, \tag{2.7}$$

from which it immediately follows

$$V^{\mathrm{LDA}}_{\mathrm{xc}}[n(\mathbf{r})] = \left(\varepsilon^{\mathrm{HEG}}(n) + n \frac{d\varepsilon^{\mathrm{HEG}}}{dn} \right)_{n=n(\mathbf{r})}. \tag{2.8}$$

For some initial guess for the ground state density, $n(\mathbf{r})$, $V_{\mathrm{KS}}[n](\mathbf{r})$ can be constructed as prescribed by Eqs. 2.4- 2.5 and 2.8. Equation 2.3 can then be solved to obtain KS eigenstates, $\psi_i(\mathbf{r})$. With these eigenstates, a new ground state density, $n(\mathbf{r})$, can be calculated using

$$n(\mathbf{r}) = \sum_i f_i |\psi_i(\mathbf{r})|^2, \tag{2.9}$$

where f_i denotes the occupation of the i^{th} orbital. If $n(\mathbf{r})$ differs from the previous density, the entire procedure is repeated and a new density is computed. This cycle is repeated until the density is unchanged between cycles. In this way the density is computed self-consistently. At the end of the KS cycle, the ground state density is, in principle, guaranteed to be equivalent to the ground state density of the many-body system. In practice the density will differ as a result of the approximate exchange-correlation functional used, e.g. LDA.

Finally, with the ground state density, the total energy $E[n(\mathbf{r})]$ is given by

$$E[n(\mathbf{r})] = 2\sum_{i}^{N_e/2} \varepsilon_i - \frac{1}{2}\int \frac{n(\mathbf{r})n(\mathbf{r}')}{|\mathbf{r}-\mathbf{r}'|} d^3\mathbf{r}d^3\mathbf{r}' + E_{\text{xc}}[n] - \int n(\mathbf{r})v_{\text{xc}}(\mathbf{r})d^3\mathbf{r} + E^{\text{ion-ion}}, \qquad (2.10)$$

where $E^{\text{ion-ion}}$ denotes the contribution to the total energy due to ion-ion interactions.

2.4 Plane-wave DFT and the Pseudopotential Method

In this thesis, we work exclusively with extended solid-state systems, systems that possess some discrete translational symmetry. From Bloch's theorem, we know single-particle eigenstates of these systems can be written as

$$\psi_{n\mathbf{k}}(\mathbf{r}) = e^{i\mathbf{k}\cdot\mathbf{r}}u_{n\mathbf{k}}(\mathbf{r}), \qquad (2.11)$$

where n is the band index, $\mathbf{k}$, the wavevector, and $u_{n\mathbf{k}}(\mathbf{r})$ is a cell periodic function so that $u_{n\mathbf{k}}(\mathbf{r}) = u_{n\mathbf{k}}(\mathbf{r}+\mathbf{R})$ where $\mathbf{R}$ is a lattice vector. The periodicity of $u_{n\mathbf{k}}(\mathbf{r})$ ensures that it can be expressed as a Fourier expansion, namely

$$u_{n\mathbf{k}}(\mathbf{r}) = \sum_{\mathbf{G}} c_{n\mathbf{k}}(\mathbf{G})e^{i\mathbf{G}\cdot\mathbf{r}}, \qquad (2.12)$$

where $\mathbf{G}$ are reciprocal lattice vectors, related to lattice vectors $\mathbf{R}$ through the relation $\mathbf{R}\cdot\mathbf{G} = 2\pi m$, where m is an integer and $c_{n\mathbf{k}}(\mathbf{G}) = \langle \mathbf{k}+\mathbf{G}|\psi_{n\mathbf{k}}\rangle$. These relations motivate the choice to expand the Kohn-Sham eigensystem in a basis of plane waves. In this basis, the Kohn-Sham eigensystem takes the form [33]

$$\sum_{\mathbf{G}'}\left[\frac{|\mathbf{k}+\mathbf{G}|^2}{2}\delta_{\mathbf{G}\mathbf{G}'} + \langle \mathbf{k}+\mathbf{G}|V_{\text{KS}}|\mathbf{k}+\mathbf{G}'\rangle\right]c_{n\mathbf{k}}(\mathbf{G}') = \varepsilon_{n\mathbf{k}}c_{n\mathbf{k}}(\mathbf{G}), \qquad (2.13)$$

where $\varepsilon_{n\mathbf{k}}$ are the eigenenergies which when plotted as a function of $\mathbf{k}$ give the Kohn-Sham bandstructure. Generally, one solves Eq. 2.13 in a subset of $\mathbf{G}$ vectors setting an upper cutoff — i.e. $|\mathbf{k}+\mathbf{G}|^2/2 < E_{\text{cut}}$.

One challenge associated with the procedure is that ionic potential is long-range and falls off very slowly in reciprocal space, i.e. $\langle \mathbf{k}+\mathbf{G}|V_{\text{ion}}|\mathbf{k}+\mathbf{G}\rangle \propto 4\pi/|\mathbf{k}+\mathbf{G}|^2$. A solution is to use a shorter range potential which produces the essential feature of the true ionic potential in the chemically relevant region. The idea dates back to the early work of Philips and Kleinman [34]. In this thesis we work exclusively with norm-conserving pseudopotentials [35].

2.5 Density Functional Perturbation Theory

Importantly DFT can formally be extended to compute first order changes in the ground density energy due to static perturbations. This extension is called density functional perturbation theory (DFPT) [27]. Consider a perturbation, $\delta V_{\mathrm{ext}}(\mathbf{r})$, to the external potential. This change will in turn induce a change in the wavefunction, $\delta\psi(\mathbf{r})$, and ground state density, $\delta n(\mathbf{r})$. The change in the ground state density will induce a change in the Hartree, $\delta V_{\mathrm{H}}(\mathbf{r})$, and exchange-correlation, $\delta V_{\mathrm{xc}}(\mathbf{r})$, potentials. Below, we collect a set of equations which relates all these quantities

$$\delta V_{\mathrm{KS}}[\delta n](\mathbf{r}) = \delta V_{\mathrm{ext}}(\mathbf{r}) + V_{\mathrm{H}}[\delta n](\mathbf{r}) + \frac{dV_{\mathrm{xc}}(n)}{dn}\delta n(\mathbf{r}) \tag{2.14}$$

$$(H_{\mathrm{KS}} - \varepsilon_i)\,|\delta\psi_i\rangle = -(\delta V_{\mathrm{KS}} - \delta\varepsilon_i)\,|\psi_i\rangle \tag{2.15}$$

$$\delta n(\mathbf{r}) = 2\mathrm{Re}\sum_i \psi_i^\star(\mathbf{r})\delta\psi_i(\mathbf{r}). \tag{2.16}$$

Equation 2.15 is often refereed to as the Sternheimer equation [36] and is an intermediate step in deriving the first order Rayleigh-Schrödinger correction to the wavefunction, $|\delta\psi\rangle$, in the presence of a perturbation δV_{ext}. In the same equation, $\delta\varepsilon_i$ is the first-order change in the eigenenergy ε_i, and is given by $\delta\varepsilon_i = \langle\psi_i|\delta V_{\mathrm{ext}}|\psi_i\rangle$. In practice Eqs. 2.14- 2.16 are solved iteratively provided H_{KS} for the unperturbed system has already been solved and $|\psi_i\rangle$ are known.

Two critical advantages of using the DFPT approach are: (i) it only requires occupied states and (ii) for periodic systems, these equations can be solved in the unit cell regardless of the wavevector associated with the perturbing potential. To see this last point, consider a monochromatic perturbation with wavevector $\mathbf{q}$ – i.e. $\delta V_{\mathrm{KS}}(\mathbf{r}) = \partial_{\mathbf{q}} V_{\mathrm{KS}}(\mathbf{r})e^{i\mathbf{q}\cdot\mathbf{r}}$ where $\partial_{\mathbf{q}} V_{\mathrm{KS}}(\mathbf{r})$ is a lattice periodic function. When specialized to this case, Eqs. 2.14- 2.16 take the form

$$\partial_{\mathbf{q}} V_{\mathrm{KS}}(\mathbf{r}) = \partial_{\mathbf{q}} V_{\mathrm{ext}}(\mathbf{r}) + \int d^3\mathbf{r}\frac{\partial_{\mathbf{q}} n(\mathbf{r}')}{|\mathbf{r}-\mathbf{r}'|}e^{-i\mathbf{q}\cdot(\mathbf{r}-\mathbf{r}')} + \left.\frac{dv_{\mathrm{xc}}(n)}{dn}\right|_{n=n(\mathbf{r})}\partial_{\mathbf{q}} n(\mathbf{r}) \tag{2.17}$$

$$(H_{\mathrm{KS}}^{\mathbf{k}+\mathbf{q}} - \varepsilon_{v\mathbf{k}})\,|\Delta u_{v\mathbf{k}}\rangle = -\partial_{\mathbf{q}} V_{\mathrm{KS}}\,|u_{n\mathbf{k}}\rangle \tag{2.18}$$

$$\partial_{\mathbf{q}} n(\mathbf{r}) = 2\sum_{v\mathbf{k}} u_{v\mathbf{k}}^\star(\mathbf{r})\Delta u_{v\mathbf{k}+\mathbf{q}}(\mathbf{r}), \tag{2.19}$$

where $H_{\mathrm{KS}}^{\mathbf{k}} = e^{-i\mathbf{k}\cdot\mathbf{r}}H_{\mathrm{KS}}e^{i\mathbf{k}\cdot\mathbf{r}}$. In this form, the DFPT equations have been reduced to a form which involves only lattice periodic functions, namely, $H_{\mathrm{KS}}^{\mathbf{k}+\mathbf{q}}(\mathbf{r})$, $\partial_{\mathbf{q}} V_{\mathrm{ext}}(\mathbf{r})$, $\partial_{\mathbf{q}} n(\mathbf{r})$, $\partial_{\mathbf{q}} V_{\mathrm{KS}}(\mathbf{r})$.

2.6 The Dynamical Matrix from DFPT

The DFPT formalism can be used to study lattice dynamics. Let $\boldsymbol{\tau}_{kp}$ denote the initial positions of each atom in the solid, with k denoting the position of the k^{th} atom in the unit cell and p labeling the cell relative to the origin. Consider now perturbing this these ions with some monochromatic perturbation, with wavevector $\mathbf{q}$, so that the new positions of the atoms are given by $\boldsymbol{\tau}_{kp} + \mathbf{u}_k(\mathbf{q})e^{i\mathbf{q}\cdot\mathbf{R}_p}$ where $\mathbf{u}_k(\mathbf{q})$ defines the distortion pattern. If the distortion is small, it is meaningful to speak of the rate of change in the ionic potential that it induces. The change takes the from

$$\frac{\partial V_{\text{ion}}(\mathbf{r})}{\partial u_{k\alpha}(\mathbf{q})} = e^{i\mathbf{q}\cdot\mathbf{r}}\partial_{k\alpha,\mathbf{q}}V_{\text{ion}}(\mathbf{r}), \tag{2.20}$$

where α labels the Cartesian direction of the displacement and $\partial_{k\alpha,\mathbf{q}}V_{\text{ion}}(\mathbf{r})$ is the planewave periodic part of the change in the potential which can be explicitly expressed as

$$\partial_{k\alpha,\mathbf{q}}V_{\text{ion}}(\mathbf{r}) = \sum_p e^{-\mathbf{q}\cdot(\mathbf{r}-\mathbf{R}_p)} \left.\frac{\partial V_{\text{ion}}}{\partial \tau_{k\alpha}}\right|_{\mathbf{r}-\mathbf{R}_p}. \tag{2.21}$$

In this form, it is readily verified that $\partial_{k\alpha,\mathbf{q}}V_{\text{ion}}(\mathbf{r})$ is cell-periodic in $\mathbf{r}$. The derivative on $V_{\text{ion}}(\mathbf{r})$ can be performed analytically and, in Fourier space, the result reads

$$\partial_{k\alpha,\mathbf{q}}V_{\text{ion}}(\mathbf{G}) = -i(\mathbf{q}+\mathbf{G})_\alpha V_k(\mathbf{q}+\mathbf{G})e^{-i(\mathbf{q}+\mathbf{G})\cdot\boldsymbol{\tau}_k}, \tag{2.22}$$

where we have used the convention $f(\mathbf{G}) = V_{\text{uc}}^{-1}\int d\mathbf{r}e^{-i\mathbf{G}\cdot\mathbf{r}}f(\mathbf{r})$ where V_{uc} is the unit cell volume and V_k, the psuedopotential for ion k.

Taking $\partial_{k\alpha,\mathbf{q}}V_{\text{ion}}(\mathbf{r})$ as the perturbing external potential, the DFPT equations, 2.17- 2.19, can now be solved to obtain the induced change in the density, $\partial_{k\alpha,\mathbf{q}}n(\mathbf{r})$ and change in the Kohn-Sham potential $\partial_{k\alpha,\mathbf{q}}V_{\text{KS}}(\mathbf{r})$. With these ingredients the change in the total electronic energy is given by

$$\frac{\partial^2 E^{\text{el}}}{\partial u^\star_{k\alpha}(\mathbf{q})\partial u_{k'\alpha'}(\mathbf{q})} = \int \left(\frac{\partial n(\mathbf{r})}{\partial u_{k\alpha}(\mathbf{q})}\right)^\star \frac{\partial V_{\text{ion}}(\mathbf{r})}{\partial u_{k'\alpha'}(\mathbf{q})} d^3\mathbf{r} + \int n(\mathbf{r}) \frac{\partial^2 V_{\text{ion}}(\mathbf{r})}{\partial u^\star_{k\alpha}(\mathbf{q})\partial u_{k'\alpha'}(\mathbf{q})} d^3\mathbf{r}. \tag{2.23}$$

That the second derivative of the total energy with respect to ionic displacements can be determined as a function of the first derivative of the electronic density is a specific case of the $(2n+1)-$theorem. This theorem, is an extension of the Hellman-Feynman theorem and states that the $(2n+1)^{\text{th}}$ derivative of the total energy can be computed from the n^{th} derivative of the wavefunction [37].

The mass reduced dynamical matrix [3, 25] is defined as

$$D^{\alpha\alpha'}_{kk'}(\mathbf{q}) = \frac{1}{\sqrt{M_k M_{k'}}}\left[\frac{\partial^2 E^{\text{el}}}{\partial u^\star_{k\alpha}(\mathbf{q})\partial u_{k'\alpha'}(\mathbf{q})} + \frac{\partial^2 E^{\text{ion}}}{\partial u^\star_{k\alpha}(\mathbf{q})\partial u_{k'\alpha'}(\mathbf{q})}\right], \tag{2.24}$$

where the second term on the right-hand side is the second order change in the ionic contribution to the total energy. Eigenvectors of the mass reduced dynamical matrix give the eigenfrequencies, $\omega_{\mathbf{q}\nu}$, and eigenmodes, $\xi^\nu_{k\alpha}(\mathbf{q})$, of the system, specifically

$$\sum_{k'\alpha'} D^{\alpha\alpha'}_{kk'}(\mathbf{q})\xi^\nu_{k'\beta}(\mathbf{q}) = \omega^2_{\mathbf{q}\nu}\xi^\nu_{k\alpha}(\mathbf{q}), \tag{2.25}$$

where ν labels the branch index of the mode. The eigenvectors are a complete basis and we can represent any displacement in this basis, explicitly

$$u_{k\alpha p} = \frac{1}{\sqrt{N_{\mathbf{q}}}} \sum_{\mathbf{q}\nu} \sqrt{\frac{1}{2M_k \omega_{\mathbf{q}\nu}}} \xi^{\nu}_{k\alpha}(\mathbf{q}) e^{i\mathbf{q}\cdot\mathbf{R}_p} [b^{\dagger}_{-\mathbf{q}\nu} + b_{\mathbf{q}\nu}], \tag{2.26}$$

where $u_{k\alpha p}$ denote the change in the position of the k^{th} ion in the α-direction located p unit cells from the origin. M_k denotes the mass of the k^{th} atom and in writing down Eq. 2.26 we have also quantized the theory introducing phonon creation $b^{\dagger}_{-\mathbf{q}\nu}$ and annihilation $b_{\mathbf{q}\nu}$ operators.

2.7 The Electron Phonon Matrix Element from DFPT

In addition to the change in the total energy with ionic displacement, to compute the electron-phonon coupling matrix element, we also need to know how the DFT Hamiltonian itself changes with respect to ionic displacement. Consider again the displacement $u_{k\alpha p}$. If the displacement is small we can expand the Kohn-Sham Hamiltonian about equilibrium coordinates as

$$H_{\text{KS}}(\mathbf{r}; \boldsymbol{\tau}_0 + \mathbf{u}) = -\frac{\nabla^2}{2} + V_{\text{KS}}(\mathbf{r}, \boldsymbol{\tau}_0) + \sum_{kp\alpha} \frac{\partial V_{\text{KS}}(\mathbf{r})}{\partial \tau_{k\alpha p}} u_{k\alpha p} + \cdots , \tag{2.27}$$

where the notation $H_{\text{KS}}(\mathbf{r}; \boldsymbol{\tau}_0 + \mathbf{u})$ symbolically denotes the KS Hamiltonian with ionic coordinates displaced from their equilibrium position, $\boldsymbol{\tau}_0$, by $\mathbf{u}$. The final term in this expansion ultimately gives rise to the electron-phonon interaction and can be treated as a perturbation, presently we label it $H_{\text{elph}}(\mathbf{r})$. We can use the normal mode expansion in Eq. 2.26 to rewrite this perturbation in normal mode coordinates, namely

$$H_{\text{elph}}(\mathbf{r}) = \frac{1}{\sqrt{N_{\mathbf{q}}}} \sum_{\mathbf{q}\nu} \left[e^{i\mathbf{q}\cdot\mathbf{r}} \frac{1}{\sqrt{2\omega_{\mathbf{q}\nu}}} \sum_{k\alpha} \frac{\xi^{\nu}_{k\alpha}(\mathbf{q})}{\sqrt{2M_k}}\ \partial_{k\alpha,\mathbf{q}} V_{\text{KS}}(\mathbf{r}) \right] (b^{\dagger}_{-\mathbf{q}\nu} + b_{\mathbf{q}\nu}) \tag{2.28}$$

where $\partial_{k\alpha,\mathbf{q}} V_{\text{KS}}(\mathbf{r})$ is cell-periodic and defined in a manner analogous to $\partial_{k\alpha,\mathbf{q}} V_{\text{ion}}(\mathbf{r})$ (see Eq. 2.20). Notably, at the end of the DFPT cycle, we have access to $\partial_{k\alpha,\mathbf{q}} V_{\text{KS}}(\mathbf{r})$ so that the electron-phonon Hamiltonian can be parameterized.

To clean up the notation, it is common practice [38] to rewrite Eq. 2.28 in terms of the electron-phonon matrix element which we define in real-space as

$$g_{\mathbf{q}\nu}(\mathbf{r}) = \frac{1}{\sqrt{2\omega_{\mathbf{q}\nu}}} \sum_{k\alpha} \frac{\xi^{\nu}_{k\alpha}(\mathbf{q})}{\sqrt{2M_k}}\ \partial_{k\alpha,\mathbf{q}} V_{\text{KS}}(\mathbf{r}). \tag{2.29}$$

Finally we can quantize the theory in the electronic coordinate, taking the unperturbed Bloch states as our basis, so that $\hat{H}_{\text{elph}}$ reads

$$\hat{H}_{\text{elph}} = \frac{1}{\sqrt{N_{\mathbf{q}}}} \sum_{\mathbf{q}\nu} g_{mn\nu}(\mathbf{k},\mathbf{q}) c^{\dagger}_{m\mathbf{k}+\mathbf{q}} c_{n\mathbf{k}} (b^{\dagger}_{-\mathbf{q}\nu} + b_{\mathbf{q}\nu}), \tag{2.30}$$

where we have introduced the notation

$$\begin{aligned} g_{mn\nu}(\mathbf{k},\mathbf{q}) &= \langle m\mathbf{k}+\mathbf{q}| e^{i\mathbf{q}\cdot\mathbf{r}} g_{\mathbf{q}\nu}(\mathbf{r}) |n\mathbf{k}\rangle \\ &= \langle u_{m\mathbf{k}+\mathbf{q}}| g_{\mathbf{q}\nu}(\mathbf{r}) |u_{n\mathbf{k}}\rangle_{\text{uc}}\,, \end{aligned} \tag{2.31}$$

where the subscript uc denotes that the integration should be performed over the unit cell.

2.8 The Single-Particle Many-Body Green's Function

To this point, we have been primarily concerned with DFT, which as emphasized in the introduction, is a formally exact theory for studying ground state properties. For studying phenomena related to single-particle excitations, DFT within common approximations often performs poorly. In fact, the DFT eigenvalues cannot formally be interpreted as quasiparticle excitations and care should be used when trying to interpret them in this way [39]. To study excitation energies, we need a more general object than the ground state density $n(\mathbf{r})$. That object is the single-particle many-body Green's function (abbreviated here as just the Green's function [40–42]). Below, we define this object and give its microscopic interpretation and connection to excitation energies.

In many-body theory, the Green's function is defined as

$$G(\mathbf{r}t;\mathbf{r}'t') = -i\,\langle \Psi_0^N | T\psi(\mathbf{r}t)\psi^{\dagger}(\mathbf{r}'t') | \Psi_0^N \rangle\,, \tag{2.32}$$

where $\psi^{\dagger}(\mathbf{r}t)$ and $\psi(\mathbf{r}'t')$ are Fermoinic creation and annihilation operators, respectively, T is the time-ordering operator, and Ψ_0^N denotes the N-particle ground state. Physically, $G(\mathbf{r}t;\mathbf{r}'t)$ encodes the probability for a particle (or hole) injected into an N-particle system at position $\mathbf{r}'$ and time t', to be found at position $\mathbf{r}$ at time t. Microscopically we can interpret this as a propagator.

For systems in equilibrium, $G(\mathbf{r}t;\mathbf{r}'t')$ can be expressed as a function of the time difference $t-t'$ and it will often be useful to work in the Fourier representation, defined as

$$G(\mathbf{r},\mathbf{r}',\omega) = \int dt e^{i\omega(t-t')} G(\mathbf{r},\mathbf{r}',t-t'). \tag{2.33}$$

Working in the frequency domain and inserting a resolution of the identity, we arrive at the Lehman representation [40, 41]

$$G(\mathbf{r},\mathbf{r}',\omega) = \sum_{s} \frac{\langle \Psi_0^N | \psi(\mathbf{r}) | \Psi_s^{N+1}\rangle \langle \Psi_s^{N+1} | \psi^{\dagger}(\mathbf{r}) | \Psi_N^0\rangle}{\omega - (E_s^{N+1} - E_0^N) + i\eta} \tag{2.34}$$

where $\Psi_s^{N\pm1}$ and $E_s^{N\pm1}$ denote the s^{th} excited state Dyson-orbital and energy, respectively, of $N\pm1$ many-body system. In this form, we see that poles of the Green's function give electron addition, $(E_s^{N+1}-E_0^N)$, and removal, $(E_0^N-E_s^{N-1})$, excitation energies. The imaginary part of G gives the spectral function, $A(\omega)$.

2.9 The Hedin Equations

To this point we have discussed the Kohn-Sham formalism for constructing an auxiliary system whose solution, in principle, gives the exact ground state density, $n(\mathbf{r})$. We would like find a similar set of equations whose solution gives the single particle many-body Green's function. In condensed matter communities, these equations are referred to as the Hedin equations [22, 43], we state them below

$$G(12) = G_0(12) + \int d(34)G_0(13)\Sigma(34)G(42) \tag{2.35}$$

$$\Sigma(12) = \int d(34)G(13)\Gamma(324)W^{\text{el}}(41^+) \tag{2.36}$$

$$W^{\text{el}}(1,2) = v_c(1,2) + \int d(34)v_c(13)P^{\text{el}}(34)W^{\text{el}}(42) \tag{2.37}$$

$$P^{\text{el}}(1,2) = \int d(34)G(12)G(41^+)\Gamma(342) \tag{2.38}$$

$$\Gamma(123) = \delta(12)\delta(13) + \int d(4567)\frac{\delta\Sigma(12)}{\delta G(45)}G(46)G(75)\Gamma(673), \tag{2.39}$$

where $\Sigma(12)$, $W^{\text{el}}(12)$, $P^{\text{el}}(12)$, $\Gamma(123)$ are the electron self-energy, screened Coulomb interaction, electronic polarizability, and vertex correction, respectively. While v_c and G_0 are the bare Coulomb and non-interacting Green's function, respectively. In writing down Eqs. 2.35- 2.39 we have adopted the notation that numbers label space-time points so $1 = (\mathbf{r}_1, t_1)$ and $\Sigma(12) = \Sigma(\mathbf{r}_1 t_1, \mathbf{r}_2 t_2)$. Finally the $^+$ symbol denotes that the time variable for that index should be taken infinitesimally later than the time index which proceeds it, for example $G(14^+)$ should be read as $G(\mathbf{r}t, \mathbf{r'}t+\eta)$ where η is an infinitesimally positive quantity.

As presently written the equations may seem unfamiliar and unmotivated. The form of these equations appears much more natural when viewed as deriving from the QED Lagrangian instead of the non-relativistic many-body Hamiltonian [44, 45]. In this context, G and W are interpreted as dressed propagators for the electron and photon respectively while G_0 and v_c are their bare counterparts and Σ and P^{el} are the electron and photon self-energies. Finally $\Gamma(123)$ is the dressed electron-photon vertex while $\delta(12)\delta(13)$ the bare counterpart. That the vertex is a 3-point interaction is not surprising given the electron-photon interaction in the QED Lagrangian is also 3-point. Starting from the non-relativistic Hamiltonian, it is possible to restore this 3-point coupling at the cost of introducing an auxiliary Bosonic field by making a Hubbard-Stravonovich transformation on the 4-point

Coulomb interaction [46]. The auxiliary field introduced in the process is precisely the photon field. Finally we remark that the infinitesimal time orderings which appear in 2.36 and 2.38 are a consequence of integrating out the photon field and taking the non-relativistic limit. When the full photon propagator is retained, this time ordering issue does not appear.

2.10 The *GW* Approximation

A direct solution of Eq. 2.35- 2.39 is generally not computationally feasible and as a result a number of approximations are typically made [11, 47–49]. First, vertex corrections are ignored so that $\Gamma(123) = \delta(12)\delta(13)$. With this approximations the Hedin equations collapse to

$$\Sigma^{\mathrm{GW}}(\mathbf{r},\mathbf{r}',\omega) = \frac{i}{2\pi}\int d\omega' G(\mathbf{r},\mathbf{r}',\omega+\omega')W^{\mathrm{el}}(\mathbf{r},\mathbf{r}',\omega')e^{i\eta\omega'} \tag{2.40}$$

$$W^{\mathrm{el}}(\mathbf{r},\mathbf{r}',\omega) = \int d^3\mathbf{r}''\varepsilon^{-1}(\mathbf{r},\mathbf{r}'',\omega)v_c(\mathbf{r}''-\mathbf{r}') \tag{2.41}$$

$$\varepsilon(\mathbf{r},\mathbf{r}',\omega) = \delta(\mathbf{r},\mathbf{r}') - \int d^3\mathbf{r}'' P^{\mathrm{el}}(\mathbf{r},\mathbf{r}'',\omega)v_c(\mathbf{r}''-\mathbf{r}') \tag{2.42}$$

$$P^{\mathrm{el}}(\mathbf{r},\mathbf{r}',\omega) = i\int d\omega' G(\mathbf{r},\mathbf{r}',\omega+\omega')G(\mathbf{r}',\mathbf{r},\omega'), \tag{2.43}$$

where we have expressed all quantities in the frequency domain. Next the full interacting Green's function is replaced with the non-interacting Green's function, i.e. $G(12) = G_0(12)$. Then, Ψ_0^N takes the form of a single Slater determinant and G_0 can be expressed as [40, 41]

$$G_0(\mathbf{r},\mathbf{r}',\omega) = \sum_j \frac{\psi_j(\mathbf{r})\psi_j^\star(\mathbf{r}')}{\omega-\varepsilon_j \pm i\eta}, \tag{2.44}$$

where $\psi_j(\mathbf{r})$ and ε_j are single-particle orbitals and energies associated with state j while η is an infinitesimal positive or negative quantity depending on whether ε_j lies above or below the Fermi energy. With this approximation, the integral in Eq. 2.43 can be performed exactly and polarizability is given by,

$$P^{\mathrm{el}}(\mathbf{r},\mathbf{r}',\omega) = \sum_{ij}(f_i - f_j)\frac{\psi_i^\star(\mathbf{r})\psi_j(\mathbf{r})\psi_j^\star(\mathbf{r}')\psi_i(\mathbf{r}')}{\varepsilon_i-\varepsilon_j+\omega+i\eta} \tag{2.45}$$

where f_i denotes the Fermi-Dirac occupation factor for state i [50, 51].

In general the frequency integral for the self-energy, appearing in Eq. 2.40, cannot be evaluated analytically as we did for the polarizability. Short of computing the integral explicitly it is still possible to build some insight by noting that the integral can be analytically continued in the complex plane so that it decouples to two terms, namely

$$\Sigma^{\mathrm{GW}}(\mathbf{r},\mathbf{r}',\omega) \equiv \Sigma^{\mathrm{SX}}(\mathbf{r},\mathbf{r}',\omega) + \Sigma^{\mathrm{CH}}(\mathbf{r},\mathbf{r}',\omega), \tag{2.46}$$

where

$$\begin{aligned}\Sigma^{\mathrm{SX}}(\mathbf{r},\mathbf{r}',\omega) &= \frac{i}{2\pi}\int_C d\omega' G(\mathbf{r},\mathbf{r}',\omega+\omega')\mathcal{P}[W^{\mathrm{el}}(\mathbf{r},\mathbf{r}',\omega')]e^{i\eta\omega'} \\ &= -\sum_j^{\mathrm{occ}} \psi_j(\mathbf{r})\psi_j^\star(\mathbf{r}')W^{\mathrm{el}}(\mathbf{r},\mathbf{r}',\omega-\varepsilon_j),\end{aligned} \tag{2.47}$$

where the $\mathcal{P}$ in the first line is the Cauchy principal value. We are able to perform this part of the integral because the poles of G are explicitly known. Additional details on the evaluation including the contour, C, used can be found in Ref. [52]. We label this contribution SX, because it has the form of a dynamically screened exchange interaction. The second term takes the form

$$\Sigma^{\mathrm{CH}}(\mathbf{r},\mathbf{r}',\omega) = \frac{i}{2\pi}\int_C d\omega' \mathcal{P}[G(\mathbf{r},\mathbf{r}',\omega+\omega')]W^{\mathrm{el}}(\mathbf{r},\mathbf{r}',\omega')e^{i\eta\omega'}. \tag{2.48}$$

Here we cannot proceed further without additional approximation because unlike G_0, P^{el}, and ε, the poles of ε^{-1} and in turn W are unknown. Short of performing the numerical integration, one way to proceed is to fit ε^{-1} to a plasmon-pole model, e.g. the Hybertsen-Louie [11] or Godby-Needs [52] plasmon-pole model. Then the pole structure would be known and the integral could be performed. Here, because we are just interested in the physical content of Σ^{CH} we make an even more drastic approximation and take the static limit. It can be shown that

$$\Sigma^{\mathrm{CH}}(\mathbf{r},\mathbf{r}',\omega=0) = \frac{1}{2}\delta(\mathbf{r}-\mathbf{r}')[W^{\mathrm{el}}(\mathbf{r},\mathbf{r}',\omega) - v_c(\mathbf{r}-\mathbf{r}')]. \tag{2.49}$$

This term can be interpreted as the electrostatic energy associated with the quasiparticle and charge it displaces when it is created. It is know as the Coulomb hole term [43].

Having interpreted Σ^{GW}, we now discuss how to use it. With the explicit form of G_0 given in Eq. 2.44. Dyson's equation, Eq. 2.35, can be cast as an eigenvalue equation with the form

$$\left[-\frac{\nabla^2}{2} + V_{\mathrm{ion}}(\mathbf{r}) + V_{\mathrm{H}}[n](\mathbf{r})\right]\psi_i(\mathbf{r}) + \int d^3\mathbf{r}'\Sigma^{\mathrm{GW}}(\mathbf{r},\mathbf{r}',E_i)\psi_i(\mathbf{r}') = E_i\psi_i(\mathbf{r}). \tag{2.50}$$

Equation 2.50 has the same form as the Kohn-Sham equation but the with exchange correlation potential replaced by the GW self-energy. In this light, we can view $\Sigma^{\mathrm{GW}}(\mathbf{r},\mathbf{r}',\omega)$ as an effective, non-local, frequency-dependent potential which the electrons of the many-body system move in. In theory Eq. 2.50 could be solved self-consistently for both the GW eigenvalues, E_i, and wavefunctions, in practice, from many systems, the KS and GW wavefunctions are very nearly the same so that $\Sigma^{\mathrm{GW}}(\mathbf{r},\mathbf{r}',\omega)$ can be treated pertubatively. The the equation we must solve is

$$E_i = \varepsilon_i + \langle i|\Sigma(\mathbf{r},\mathbf{r}',E_i)|i\rangle\,, \tag{2.51}$$

where the distinction between the Kohn-Sham, ε_i, and GW, E_i, eigenvalues should be kept in mind. Eq. 2.51, can be solved graphically but often it is sufficient to expand $\langle i|\Sigma(\mathbf{r},\mathbf{r}',E_i)|i\rangle$ to linear order and solve the resulting linear equation [11].

Finally, we note that up to this point we have given all expressions in real space but for periodic systems calculations are typically performed in reciprocal space. We define the two-point Fourier transform using the following convention

$$f(\mathbf{r},\mathbf{r}') = \frac{1}{V_{\text{xtal}}} \sum_{\mathbf{q}\mathbf{G}\mathbf{G}'} e^{i(\mathbf{q}+\mathbf{G})\cdot\mathbf{r}} f_{\mathbf{G}\mathbf{G}'}(\mathbf{q}) e^{-i(\mathbf{q}+\mathbf{G})\cdot\mathbf{r}'}, \tag{2.52}$$

with this convention in reciprocal space, the polarizability reported in Eq. 2.43 reads [53]

$$P^{\text{el}}_{\mathbf{G}\mathbf{G}'}(\mathbf{q},\omega) = \frac{1}{V_{\text{xtal}}} \sum_{nn'\mathbf{k}} \frac{\langle n\mathbf{k}|e^{-i(\mathbf{q}+\mathbf{G})\cdot\mathbf{r}}|m\mathbf{k}+\mathbf{q}\rangle\,\langle m\mathbf{k}+\mathbf{q}|e^{i(\mathbf{q}+\mathbf{G})\cdot\mathbf{r}}|n\mathbf{k}\rangle}{\varepsilon_{n\mathbf{k}} - \varepsilon_{m\mathbf{k}+\mathbf{q}} + \omega + i\eta}. \tag{2.53}$$

While the convolutions over response functions in real-space take the form of products in reciprocal space. For instance Eq. 2.41 becomes

$$W_{\mathbf{G}\mathbf{G}'}(\mathbf{q},\omega) = \varepsilon^{-1}_{\mathbf{G}\mathbf{G}'}(\mathbf{q},\omega) v_c(\mathbf{q}+\mathbf{G}'). \tag{2.54}$$

2.11 The Hedin-Baym Equations

As presently written, the Hedin equations of the previous section assume ions are clamped at their equilibrium locations. It is possible to extend these equations to include harmonic fluctuations of ions about their equilibrium position. These auxiliary equations involve the displacement-displacement correlation function defined as

$$D_{k\alpha p,k'\alpha' p'}(t-t') = -i\,\langle T u_{k\alpha p}(t) u_{k'\alpha' p'}(t')\rangle\,, \tag{2.55}$$

which encodes how ionic motion is coupled in space and time. An extension of the Hedin equations to include the motion of $D_{k\alpha p,k'\alpha' p'}(t-t')$ and its influence on the electronic structure is summarized in Ref. [38]. Here we state a subset of these additional equations relevant to this thesis.

The motion of the $D_{k\alpha p,k'\alpha' p'}(\omega)$ is governed by the following Dyson-like equation

$$\sum_{k''\alpha'' p''} [M_k\omega^2\delta_{k\alpha p,k''\alpha'' p''} - \Pi_{k\alpha p,k''\alpha'' p''}(\omega)] D_{k''\alpha'' p'',k'\alpha' p'}(\omega) = \delta_{k\alpha p,k'\alpha' p'}, \tag{2.56}$$

where M_k is the mass of the k^{th} ion and the phonon self-energy can be expressed as

$$\Pi_{k\alpha p,k'\alpha' p'}(\omega) = \sum_{k''p''} Z_k Z_{k'} \frac{\partial^2}{\partial r_\alpha \partial r'_{\alpha'}} [\delta_{k'p',k''p''} W^{\text{el}}(\mathbf{r},\mathbf{r}',\omega) - \delta_{kp,k'p'} W^{\text{el}}(\mathbf{r},\mathbf{r}',0)]_{\mathbf{r}=\boldsymbol{\tau}^0_{kp}.\mathbf{r}'=\boldsymbol{\tau}^0_{k'p'}}, \tag{2.57}$$

with Z_k denoting the charge on the k^{th} ion. For a fixed $W_e(\mathbf{r},\mathbf{r}',\omega)$, Eq. 2.56 and 2.57 are sufficient to determine the phonon frequencies and eigenmodes. We observe that the influence of the electrons on ionic motion is entirely contained in $W^{\text{el}}(\mathbf{r},\mathbf{r}',\omega)$.

There is some back action on the electrons due to the phonons. In much the same way that the effect of electrons on the ionic motion can be packaged into W^{el}, much, though not all [38], of the effect of ionic motion on the electronic structure can be packaged into W^{ph}, defined through the following equations

$$W^{\text{ph}}(\mathbf{r},\mathbf{r}';\omega) = \frac{1}{N_{\mathbf{q}}}\sum_{k\alpha,k'\alpha'\mathbf{q}} g^{\star}_{k\alpha,\mathbf{q}}(\mathbf{r},\omega) D_{k\alpha,k'\alpha',\mathbf{q}}(\omega) g_{k\alpha,\mathbf{q}}(\mathbf{r}',\omega) e^{-i\mathbf{q}\cdot(\mathbf{r}-\mathbf{r}')}, \tag{2.58}$$

where

$$g_{k\alpha,\mathbf{q}}(\mathbf{r},\omega) = \int d\mathbf{r}'\varepsilon^{-1}(\mathbf{r},\mathbf{r}',\omega)\partial_{k\alpha,\mathbf{q}}V_{\text{ion}}(\mathbf{r}'). \tag{2.59}$$

Physically, we recognize $g_{k\alpha,\mathbf{q}}(\mathbf{r},\omega)$ as the electron-ion coupling matrix element which, when inverse Fourier transformed to $t-t'$ encodes how the displacement of ions along pattern $u_{k\alpha}(\mathbf{q})$ at time t' couples to an electron at $\mathbf{r}$ at time t. With this in mind, we interpret $W^{\text{ph}}(\mathbf{r},\mathbf{r}';\omega)$ as a dynamically screened electron-electron interaction mediated by a lattice distortion.

The phonon contribution to the screened interaction, W^{ph}, contributes to the electron self-energy in a manner exactly analogous to W^{el}, namely [22],

$$\Sigma^{\text{ph}}(12) = \int d(34)G(13)\Gamma(324)W^{\text{ph}}(41^{+}). \tag{2.60}$$

We note that this is just part of the influence harmonic ionic fluctuations have on the electronic structure. For this thesis, this amount of theory is sufficient. In the next section we will see how the many-body formalism of Hedin and Baym reduce to quantities computed from DFPT under the adiabatic approximation.

2.12 Connecting the Many-Body Formalism with DFPT

The purpose of this section is two fold: (i) to summarize the applicability and limitation of DFPT and (ii) to expand on the definitions introduced in the previous section, particularly W^{ph} which will play a central role in Chap. 5.

The connection between the many-body formalism and the expressions previously derived in the context of DFPT lie in the adiabatic (Born-Oppenheimer) approximation. In the many-body formalism this approximation reduce to taking the static limit ($\omega = 0$) of the phonon self-energy. To see this explicitly, we note the static limit of the phonon self-energy can be expressed as

$$\Pi_{\kappa\alpha p,k'\alpha'p'}(\omega=0)=\int\left(\frac{\partial n(\mathbf{r})}{\partial u_{\kappa\alpha p}}\right)^{\star}\frac{\partial V_{\text{ion}}(\mathbf{r})}{\partial u_{k'\alpha'p'}}d^3\mathbf{r}+\int n(\mathbf{r})\frac{\partial^2 V_{\text{ion}}(\mathbf{r})}{\partial u^{\star}_{\kappa\alpha p}\partial u_{k'\alpha'p'}}d^3\mathbf{r} + \frac{\partial^2 E^{\text{ion-ion}}}{\partial u_{\kappa\alpha p}\partial u_{k'\alpha'p'}}, \tag{2.61}$$

which is entirely equivalent in form to the DFPT inter-atomic force constants (the inverse Fourier transform of Eq. 2.24). Details on the derivation can be found in [38]. In a similar manner, taking the static limit of $g_{\mathbf{q}\nu}(\mathbf{r},\omega=0)$ gives a from for the electron-phonon vertex analogous to the DFPT vertex. We expect both approximations to be legitimate in the limit where $\varepsilon^{-1}(\omega=0)\sim\varepsilon^{-1}(\omega=\omega_{\text{ph}})$ with ω_{ph} denoting a typical phonon frequency. Based on Eq. 2.43, we expect this semi-equality to hold in the limit where electronic excitation energies are much great than the ionic ones, i.e. $E_g\gg\omega_{\text{ph}}$. For all semiconductors studied in this thesis, we expect this equality to hold.

Before closing this section we return to the electron-phonon self-energy Σ^{ph}, defined in Eq. 2.60. When the static electron-phonon vertex is used, this correction is equivalent to the Fan-Migdal self-energy correction [38]. Explicitly

$$\begin{aligned}\Sigma^{\text{ph}}_{nn'}(\mathbf{k},\omega)&=\frac{i}{2\pi}\int G(\mathbf{r},\mathbf{r}';\omega+\omega')W^{\text{ph}}(\mathbf{r},\mathbf{r}';\omega')e^{i\eta\omega'}d\omega\\&=\frac{1}{N_{\mathbf{q}}}\sum_{m\mathbf{q}\nu}\langle n\mathbf{k}|g^{\star}_{\nu\mathbf{q}}(\mathbf{r})|m\mathbf{k}+\mathbf{q}\rangle\langle m\mathbf{k}+\mathbf{q}|g_{\nu\mathbf{q}}(\mathbf{r}')|n'\mathbf{k}\rangle\\&\quad\times\left[\frac{f_{m\mathbf{k}+\mathbf{q}}}{\omega-E_{m\mathbf{k}+\mathbf{q}}+\omega_{\nu\mathbf{q}}-i\eta}+\frac{1-f_{m\mathbf{k}+\mathbf{q}}}{\omega-E_{m\mathbf{k}+\mathbf{q}}-\omega_{\nu\mathbf{q}}+i\eta}\right],\end{aligned}\tag{2.62}$$

where the off-diagonal electron-phonon self-energy is given by $\Sigma^{\text{ph}}_{nn';\mathbf{k}}(\omega)=\langle n\mathbf{k}|\Sigma^{\text{ph}}(\mathbf{r},\mathbf{r}';\omega)|n'\mathbf{k}\rangle$. A similar expression can be derived from Rayleigh-Schrödinger perturbation theory [40].

2.13 Excitons and the Bethe-Salpeter Equation Approach

Up to this point, we have concerned ourselves primarily with electrons, phonons and their coupling. However the majority of the work in this thesis centers on excitons [2], correlated electron-hole pairs, and their interaction with phonons. In this section, we introduce the computational framework used to compute exciton eigenenergies and eigenstates. In the next section we discuss the exciton-phonon matrix element.

In much the same way that we defined a Dyson equation for the single-particle Green's function, we can construct a Dyson-Like equation for the two-particle correlation function, $L(1,2;1'2')$ [41, 54], explicitly

$$L(12;1'2')=L_0(12;1'2')+\int d(3456)L_0(14;1'3)K(35;46)L(62;52'),\tag{2.63}$$

where $L_0(12;1'2') = G(12')G(21')$ and $K(35;46)$ is the electron-hole kernel related to the underlying electronic self-energy, Σ, through the following functional derivative

$$\begin{aligned} K(35;46) &= -i\delta(3,4)\delta(5,6)v_c(3,6) + \frac{\delta\Sigma(3,4)}{\delta G(6,5)} \\ &\equiv K^{\mathrm{X}}(35;46) + K^{\mathrm{D}}(35;46). \end{aligned} \tag{2.64}$$

The first term in Eq. 2.64, which we label $K^{\mathrm{X}}(35;46)$, has the form of a two particle exchange interaction. Specializing to the case of $\Sigma = \Sigma^{\mathrm{GW}}$, the functional derivative appearing in Eq. 2.64 takes the form

$$K^{\mathrm{D}}(35;46) = \frac{\delta\Sigma^{\mathrm{GW}}(34)}{\delta G(56)} = i\delta(3,6)\delta(4,5)W(3^+,4), \tag{2.65}$$

the so-called screened direct interaction. It is possible to cast Eq. 2.64 as a eigenvalue equation in a basis of free electron-hole product states [10, 12], $\langle \mathbf{r}_e\mathbf{r}_h|cv\mathbf{kQ}\rangle = \psi_{c\mathbf{k}+\mathbf{Q}}(\mathbf{r}_e)\psi^\star_{v\mathbf{k}}(\mathbf{r}_h)$, where $\psi_{n\mathbf{k}}(\mathbf{r})$ are defined in Eq. 2.11. Here c and v label conduction and valence bands, respectively, while $\mathbf{r}_e$ and $\mathbf{r}_h$ denote the electron and hole position, respectively. In this basis the BSE takes the from

$$(E_{c\mathbf{k}+\mathbf{Q}} - E_{v\mathbf{k}})A^{S\mathbf{Q}}_{cv\mathbf{k}} + \sum_{c'v'\mathbf{k}} \langle cv\mathbf{k}|K^{\mathrm{eh}}|c'v'\mathbf{k}'\mathbf{Q}\rangle\, A^{S}_{c'v'\mathbf{k}'\mathbf{Q}} = \Omega_S(\mathbf{Q})A^{S\mathbf{Q}}_{cv\mathbf{k}}, \tag{2.66}$$

where S and $\mathbf{Q}$ label the principle quantum number and center-of-mass momentum of the exciton, respectively. The eigenenergy associated with state $(S\mathbf{Q})$ is $\Omega_S(\mathbf{Q})$ while the exciton state projected onto the electron-hole basis is given by $\langle cv\mathbf{kQ}|S\mathbf{Q}\rangle = A^{S\mathbf{Q}}_{cv\mathbf{k}}$. Finally, $E_{c\mathbf{k}+\mathbf{Q}}$ and $E_{v\mathbf{k}}$ are the GW eigenenergies for states $\psi_{c\mathbf{k}+\mathbf{Q}}(\mathbf{r}_e)$ and $\psi_{v\mathbf{k}}(\mathbf{r}_h)$, respectively. In writing down 2.66, we have made the Tamm-Dancoff approximation which amounts only retaining electron-hole coupling terms in expanding K^{eh}.

A further approximation, which we will often make, is to replace the dynamically screened Coulomb interaction, $W^{\mathrm{el}}(\omega)$, with its static counterpart. This approximation is justified in the limit where the plasmon energy is much larger than the exciton binding energy [12]. With these approximations, the exchange and direct kernel can be written as

$$\langle cv\mathbf{kQ}|K^{\mathrm{X}}|c'v'\mathbf{k}'\mathbf{Q}\rangle = \sum_{\mathbf{G}} M_{cv}(\mathbf{k},\mathbf{Q},\mathbf{G})v_c(\mathbf{Q}+\mathbf{G})M^\star_{c'v'}(\mathbf{k},\mathbf{Q},\mathbf{G}) \tag{2.67}$$

$$\langle cv\mathbf{kQ}|K^{\mathrm{D}}|c'v'\mathbf{k}'\mathbf{Q}\rangle = -\sum_{\mathbf{GG}'} M^\star_{cc'}(\mathbf{k}+\mathbf{Q},\mathbf{q},\mathbf{G})W_{\mathbf{GG}'}(\mathbf{q})M_{vv'}(\mathbf{k},\mathbf{q},\mathbf{G}), \tag{2.68}$$

where $\mathbf{q} = \mathbf{k} - \mathbf{k}'$ and $M_{nn'}(\mathbf{k},\mathbf{Q},\mathbf{G}) = \langle n\mathbf{k}+\mathbf{Q}|e^{i(\mathbf{Q}+\mathbf{G})\cdot\mathbf{r}}|n'\mathbf{k}\rangle$ [55].

Finally, with the exciton expansion coefficients, $A^{S\mathbf{Q}}_{cv\mathbf{k}}$, in hand, we can write a real-space representation of the exciton state as

$$\Psi_{S\mathbf{Q}}(\mathbf{r}_e,\mathbf{r}_h) = \sum_{cv\mathbf{k}} A^{S\mathbf{Q}}_{cv\mathbf{k}}\psi_{c\mathbf{k}+\mathbf{Q}}(\mathbf{r}_e)\psi^\star_{v\mathbf{k}}(\mathbf{r}_h). \tag{2.69}$$

2.14 The Exciton-Phonon Matrix Element

We define the exciton-phonon matrix element as

$$\mathcal{G}_{S'S\nu}(\mathbf{Q},\mathbf{q}) = \frac{1}{\sqrt{2\omega_{\mathbf{q}\nu}}}\sum_{k\alpha}\frac{\xi^{\nu}_{k\alpha}(\mathbf{q})}{\sqrt{2M_k}}\left\langle S\mathbf{Q}+\mathbf{q}\right| e^{i\mathbf{q}\cdot(\mathbf{r}_e+\mathbf{r}_h)}\partial_{k\alpha,\mathbf{q}}H^{\mathrm{BSE}}\left|S\mathbf{Q}\right\rangle . \tag{2.70}$$

The definition is analogous to Eq. 2.31, except here, the sandwiching states are excitonic wavefunctions instead of single-particle Bloch eigenstates and the derivative is with respect to the BSE Hamilton instead of the KS potential. Physically $\mathcal{G}_{S'S\nu}(\mathbf{Q},\mathbf{q})$ encodes the probability amplitude for an exciton in state $(S\mathbf{Q})$ to scatter off a phonon with crystal momentum $\mathbf{q}$ and branch index ν and into state $(S\mathbf{Q}+\mathbf{q})$. Eq. 2.70 can be rewritten in the quasiparticle basis as

$$\mathcal{G}_{S'S\nu}(\mathbf{Q},\mathbf{q}) = \sum_{c'cv\mathbf{k}} A^{S'\mathbf{Q}+\mathbf{q}\star}_{c'v\mathbf{k}}\, g_{c'c\nu}(\mathbf{k}+\mathbf{Q},\mathbf{q})A^{S\mathbf{Q}}_{cv\mathbf{k}} - \sum_{cvv'\mathbf{k}} A^{S'\mathbf{Q}+\mathbf{q}\star}_{cv'\mathbf{k}}\, g_{vv'\nu}(\mathbf{k},\mathbf{q})A^{S\mathbf{Q}}_{cv\mathbf{k}+\mathbf{q}}. \tag{2.71}$$

To build intuition for this matrix element and how it differs from the usual electron-phonon matrix element, we specialize to the single-band limit with electron-phonon matrix element given by a simple Fröhlich model, $g^{e/h}_{\mathbf{q}} = C^{e/h}_F/q$, and take the exciton expansion coefficients to be of the 1s hydrogen orbital form appropriate in the Mott-Wannier model of an exciton. With these simplifications, we arrive at a form first introduced by Toyozawa [24]

$$\mathcal{G} = \frac{C^F_e}{q}\cdot\frac{1}{[1+(p_e a_B q/2)^2]} - \frac{C^F_h}{q}\cdot\frac{1}{[1+(p_h a_B q/2)^2]}, \tag{2.72}$$

where $p_{e/h} = m_{e/h}/(m_e + m_h)$ and a_B denotes the exciton radius. From Eq. 2.72 we see that the exciton-phonon vertex has an electron and hole channel, each screened by a form factor $1/[1+(p_{e/h}a_B q/2)^2]$. As a result of this form factor, the exciton-phonon vertex falls off rapidly for $a_B q \gg 1$ or equivalently $a_B \gg \lambda$. Physically phonons with wavelengths much shorter than the exciton radius, cannot efficiently couple to the exciton. In this way Eq. 2.72 highlights the close connection between the exciton radius and exciton-phonon coupling strength. From this simple analysis, it might seem that the exction phonon vertex should always couple less strongly than the underlying electron- or hole-phonon vertex. This is in fact an artifact of only considering intraband transitions. In Chap. 4, we will see that the exciton-phonon coupling can be quite large when interband transitions constructively interfere. Finally we note that when the the coupling and effective masses for the electron and hole channel are the same, i.e. $p_e = p_h$ and $C^F_e = C^F_h$, $\mathcal{G}$ vanishes. This dramatic example of polaron interference will be discussed in Chap. 5.

Chapter 3

Maximally-Localized Wannier Functions for Excitons

3.1 Introduction

Since their introduction 25 years ago [56], maximally-localized Wannier functions (MLWFs) have had a transformative impact on our ability to compute and understand one-electron observables using density functional theory (DFT). Today MLWFs, serve as a compact basis for linear scaling algorithms [57], allow for the computation of Berry phase (geometric) quantities [58–60] (e.g. polarization in electronic structure theory [61]), and find application in efficient and accurate interpolation of linear response quantities (e.g. electron-phonon matrix element) [16, 62, 63], and more [20]

In the MLWF scheme, one-electron cell-periodic Bloch states are related to localized Wannier functions through a unitary transformation which simultaneously preserves the canonical commutation relations while also localizing the sum of the spreads of the electronic states to the greatest extent possible [20, 56, 64]. Up to this point, the MLWF procedure has exclusively been applied in the context of single-particle electronic excitations and their perturbations [65]. Yet, the framework is of quite general nature and in principle can be applied to any lattice periodic function. One such excitation of broad theoretical and technological interest is the exciton, a two particle bound electron-hole state, and the extension of the MLWF scheme to excitons is the focus of this work.

Excitons are bound electron-hole pairs which often dominate the low-energy optical response of semiconducting and insulating materials. Understanding these composite particles plays an increasingly important role in the design and development of next-generation of optoelectronic devices, especially those based on complex materials with strong light-matter interactions (e.g. low-dimensional-, organic-, and perovskite- based materials). Over the past two decades, *ab initio* many-body perturbation theory within the GW approximation and Bethe-Salpeter equation (BSE) approach [11, 12, 22, 43, 54], where G is the one-electron Green's Function and W the screened Coulomb interaction, has rapidly emerged as a powerful and robust method for computing excitonic properties over a wide range of increasingly complex materials including low-dimensional transition metal dichalcogenides [66], lead-halide perovskites [67–69], and organic crystals [70–73], in all cases yielding results in excellent agreement with experiment. Given the technological relevance and increasing maturity of computational capabilities [13], revisiting the MLWF scheme in the context of excitons is quite timely.

In solid-state systems with translational symmetry, the exciton wavefunction can be written in Bloch periodic form with respect to the average electron-hole coordinate. A canonical example is the phenomenological Mott-Wannier model [4, 5] of a weakly bound exciton, described by a hydrogen-like wavefunction with the form

$$\Psi_{n\ell m,\mathbf{Q}}(\mathbf{R},\mathbf{r}) = e^{i\mathbf{Q}\cdot\mathbf{R}} F_{n\ell m}(\mathbf{r}), \tag{3.1}$$

where $\mathbf{R}$ and $\mathbf{r}$ denote the average and relative coordinate of the electron-hole pair, respectively, while $F_{n\ell m}(\mathbf{r})$ is a hydrogenic-like eigenfunction with quantum numbers $n\ell m$. Notably, while the wavefunction is localized in the relative coordinate, it is periodic in the average coordinate $\mathbf{R}$, a general feature true of all descriptions of an exciton in a perfect lattice, i.e. the Frenkel [6] and charge-transfer excitons are also cell periodic in $\mathbf{R}$.

In this work, we show how the MLWF scheme can be leveraged to construct a representation of exciton states which is maximally localized in the average electron-hole coordinate. These maximally-localized exciton Wannier functions (MLXWFs) will allow for post-processing of exciton related properties in analogy to the electronic case, for instance, the *ab initio* construction of exciton tight-binding models, the efficient interpolation of eigenenergies [55, 74] and exciton-phonon matrix elements [19, 24, 75] throughout the Brillouin zone, the computation of Berry-curvature related properties at the excitonic level [76–79], and more. Our framework also helps to unify the phenomenological Mott-Wannier [4, 5] and Frenkel [6] pictures of an exciton and expresses the splitting of the transverse and longitudinal exciton branches of the exciton band structure [80, 81] in terms of long-range dipole-dipole interactions between localized exciton Wannier orbitals.

The reminder of this chapter is organized as follows. In Sec. 3.2 we introduce exciton Wannier functions. In Sec. 3.3 we review the MLWF framework and adapt this formalism for handling the excitonic case. In Sec. 3.4, we summarize our GW-BSE approach and the computational details of our calculation. In Sec. 3.5 we apply our framework to LiF, visualizing the exciton Wannier functions in real-space and detailing convergence of the Wannier spreads. In Sec. 3.6, we discuss analytical properties of the exciton Wannier functions and their matrix elements. In this section we also discuss the connection between long-range dipole-dipole interactions in the Wannier basis and non-analyticity of the exciton eigenvalues near $\mathbf{Q} = 0$. In Sec. 3.7 demonstrate how the Wannier-Fourier interpolation can be used to interpolate exciton eigenvalues through the Brillouin zone. In Sec. 3.8, we discuss the similarities between the exciton Wannier functions and Frenkel's description of an exciton. We close, in Sec. 3.9, with a summary of our work and potential future directions.

3.2 Exciton Wannier Function

An exciton is a composite particle consisting of a bound electron-hole pair. The position of the electron, $\mathbf{r}_e$, and hole, $\mathbf{r}_h$, are correlated and encoded in the exciton wavefunction, $\Psi_{S\mathbf{Q}}(\mathbf{r}_e, \mathbf{r}_h)$, where S and $\mathbf{Q}$ denote the exciton's principle quantum number and crystal momentum respectively. Physically, $\Psi_{S\mathbf{Q}}(\mathbf{r}_e, \mathbf{r}_h)$ is the probability amplitude to simultaneously find an electron and hole at $\mathbf{r}_e$ and $\mathbf{r}_h$, respectively.

An increasingly standard approach for computing exciton states and properties in solids is the GW-BSE method. In this approach, $\Psi_{S\mathbf{Q}}(\mathbf{r}_e, \mathbf{r}_h)$ is expressed as a coherent sum over non-interacting electron-hole product states, namely,

$$\Psi_{S\mathbf{Q}}(\mathbf{r}_e, \mathbf{r}_h) = \sum_{cv\mathbf{k}} A^{S\mathbf{Q}}_{cv\mathbf{k}} \psi_{c\mathbf{k}+\mathbf{Q}/2}(\mathbf{r}_e) \psi^{\star}_{v\mathbf{k}-\mathbf{Q}/2}(\mathbf{r}_h), \tag{3.2}$$

where $\psi_{n\mathbf{k}}(\mathbf{r}) = e^{i\mathbf{k}\cdot\mathbf{r}_e} u_{n\mathbf{k}}(\mathbf{r}_e)$ denotes a single-particle Bloch state with band index n and crystal momentum $\mathbf{k}$ (e.g. computed from Kohn-Sham DFT or another cell-periodic formalism, like Hartree Fock or equation of motion coupled cluster [82]), while $A^{S\mathbf{Q}}_{cv\mathbf{k}}$ is the exciton expansion coefficient with indices c (v) denoting conduction (valence) states, respectively. The same exciton wavefunction can be written in Bloch periodic form when reexpressed in the average $\mathbf{R} = (\mathbf{r}_e + \mathbf{r}_h)/2$, and relative, $\mathbf{r} = \mathbf{r}_e - \mathbf{r}_h$, coordinates

$$\Psi_{S\mathbf{Q}}(\mathbf{R}, \mathbf{r}) = e^{i\mathbf{Q}\cdot\mathbf{R}} F_{S\mathbf{Q}}(\mathbf{R}, \mathbf{r}), \tag{3.3}$$

where $F_{S\mathbf{Q}}(\mathbf{R}, \mathbf{r})$ is cell periodic in $\mathbf{R}$ but not in $\mathbf{r}$ (note Eq. 3.1 is a specialized case of this general form). Importantly, the exciton is localized in the relative coordinate $\mathbf{r}$ but periodic in the average coordinate $\mathbf{R}$. An explicit expression for $F_{S\mathbf{Q}}$ is given in Appendix A.1.

We can define the exciton Wannier function as

$$W_{S\bar{\mathbf{R}}}(\mathbf{R}, \mathbf{r}) = \sum_{\mathbf{Q}} e^{-i\mathbf{Q}\cdot\bar{\mathbf{R}}} \Psi_{S\mathbf{Q}}(\mathbf{R}, \mathbf{r}), \tag{3.4}$$

where $\bar{\mathbf{R}}$ is a lattice vector. As defined above, the exciton Wannier functions span the same functional space as the original excitonic states and are orthonormal in indices $(S, \bar{\mathbf{R}})$ so that $\langle W_{S\bar{\mathbf{R}}} | W_{S'\bar{\mathbf{R}}'} \rangle = \delta_{SS'} \delta_{\bar{\mathbf{R}},\bar{\mathbf{R}}'}$. Further, the exciton Wannier functions are localized in $\mathbf{R}$ about $\bar{\mathbf{R}}$. This is readily seen in the limit where the cell periodic function is only weakly dependent on $\mathbf{Q}$ so that $F_{S\mathbf{Q}}(\mathbf{R}, \mathbf{r}) \approx F_S(\mathbf{R}, \mathbf{r})$. Then, $W_{S\bar{\mathbf{R}}}(\mathbf{R}, \mathbf{r}) \approx F_S(\mathbf{R}, \mathbf{r}) \sum_{\mathbf{Q}} e^{i\mathbf{Q}\cdot(\mathbf{R}-\bar{\mathbf{R}})}$. Since the only length scales appearing in the sum are the lattice parameters, $W_{\bar{\mathbf{R}}}(\mathbf{R}, \mathbf{r})$ should decay rapidly in $\mathbf{R} - \bar{\mathbf{R}}$ beyond a few unit cells. By contrast, the spread in the relative coordinate, $\mathbf{r}$, is related to the exciton radius, which, for weakly bound excitons, can be on the order of many unit cells. Thus the spread in the average coordinate should be smaller than the spread in the relative coordinate in many cases.

3.3 Maximally Localized Wannier Functions

In the MLWF scheme, extended one-electron Bloch states, $\psi_{n\mathbf{k}}(\mathbf{r}_e) = \langle \mathbf{r}_e | n\mathbf{k} \rangle$, are related to localized Wannier functions, with principle quantum number m, $w_{m\bar{\mathbf{R}}}(\mathbf{r}_e) = \langle \mathbf{r}_e | m\bar{\mathbf{R}} \rangle$, through a unitary transformation

$$w_{m\bar{\mathbf{R}}}(\mathbf{r}_e) = \sum_{n\mathbf{k}}^{J} e^{-i\mathbf{k}\cdot\bar{\mathbf{R}}} U_{nm}(\mathbf{k}) \psi_{n\mathbf{k}}(\mathbf{r}_e), \tag{3.5}$$

where $U_{nm}(\mathbf{k})$ is a unitary matrix which mixes some subset of states, J, at a given $\mathbf{k}$ point. The key idea of Marzari and Vanderbilt [56] is to take advantage of this extra gauge freedom and choose $U_{nm}(\mathbf{k})$ to localize the sum of the spread of the Wannier functions to the greatest possible extent. Here the sum of the spreads, labeled Ω, is defined as

$$\Omega[U] = \sum_{m}^{J} [\langle m\mathbf{0} | r_e^2 | m\mathbf{0} \rangle - \langle m\mathbf{0} | \mathbf{r}_e | m\mathbf{0} \rangle^2], \tag{3.6}$$

where $\mathbf{r}_e$ is understood as the position operator and the notation, $\Omega[U]$, indicates that the spread is a functional of the gauge, U.

Nowadays the minimization procedure is often performed using `Wannier90`, an open source, post-processing software for constructing MLWFs, compatible with many DFT codes [83, 84]. Eq. 3.6 is minimized in reciprocal space and `Wannier90` requires two key inputs – the overlaps of Bloch periodic states at neighboring $\mathbf{k}$-points, $M_{nm}(\mathbf{k}, \mathbf{b}) = \langle u_{n\mathbf{k}} | u_{m\mathbf{k}+\mathbf{b}} \rangle$, and a set of initial guesses for the localized Wannier orbitals, $h_j(\mathbf{r}_e)$, projected onto the unperturbed Bloch states, $A_{nj}(\mathbf{k}) = \langle \psi_{n\mathbf{k}} | h_j \rangle$. As emphasized by the developers of `Wannier90`, these inputs are entirely agnostic to the underlying electronic structure theory calculation [83, 84].

A more subtle point is that MLWF procedure itself is agnostic to the type of quasiparticle excitation which one wishes to localize so long as the excitation can be written in Bloch form. Said another way, the procedure can be used to find localized representations of any lattice periodic excitation. Accordingly, in analogy with Eq. 3.4, exciton states $\Psi_{S\mathbf{Q}}(\mathbf{R}, \mathbf{r}) = \langle \mathbf{R}\mathbf{r} | S\mathbf{Q} \rangle$ are also related to localized exciton Wannier functions, $W_{M\bar{\mathbf{R}}}(\mathbf{R}, \mathbf{r}) = \langle \mathbf{R}\mathbf{r} | M\bar{\mathbf{R}} \rangle$, through a unitary transformation, namely

$$W_{M\bar{\mathbf{R}}}(\mathbf{R}, \mathbf{r}) = \sum_{S\mathbf{Q}} e^{-i\mathbf{Q}\cdot\bar{\mathbf{R}}} U_{SM}(\mathbf{Q}) \Psi_{S\mathbf{Q}}(\mathbf{R}, \mathbf{r}), \tag{3.7}$$

where M denotes the principle quantum number of the exciton Wannier function. In further analogy with the one-electron case, we can leverage the gauge freedom to choose $U_{MS}(\mathbf{Q})$ to minimize the sum of spread of the exciton Wannier functions defined as

$$\Omega[U] = \sum_{M}^{J} [\langle M\mathbf{0} | R^2 | M\mathbf{0} \rangle - \langle M\mathbf{0} | \mathbf{R} | M\mathbf{0} \rangle^2], \tag{3.8}$$

where

$$\langle M\mathbf{0}|R^2|M\mathbf{0}\rangle = \int_{\text{xtal}} |W_{M\mathbf{0}}(\mathbf{R},\mathbf{r})|^2 R^2 d^3\mathbf{r} d^3\mathbf{R}, \tag{3.9}$$

where the subscript “xtal” denotes that the integral is to be performed over all space. As emphasized previously, the spread here is with respect to the average, not the relative coordinate.

We use the `Wannier90` package to minimize Eq. 3.8. In practice this is done by passing overlap matrices, $M_{SS'}(\mathbf{Q},\mathbf{B}) = \langle F_{S\mathbf{Q}}|F_{S'\mathbf{Q}+\mathbf{B}}\rangle$, and initial projection matrices, $A_{SJ}(\mathbf{Q}) = \langle \Psi_{S\mathbf{Q}}|H_J\rangle$, to `Wannier90`. Explicit expressions for these overlaps are given in Appendix A.1. In Tab. 3.1, we distinguish the notation used for, and draw an analogy between, electron and exciton Wannier functions.

	electron	exciton
Bloch orbital	$\psi_{n\mathbf{k}}(\mathbf{r}_e)$	$\Psi_{S\mathbf{Q}}(\mathbf{R},\mathbf{r})$
Wannier coordinate	$\mathbf{r}_e$	$\mathbf{R}$
Conjugate momentum	$\mathbf{k}$	$\mathbf{Q}$
Conjugate position	$\bar{\mathbf{R}}$	$\bar{\mathbf{R}}$
Wannier orbital	$w_{m\bar{\mathbf{R}}}(\mathbf{r}_e)$	$W_{M\bar{\mathbf{R}}}(\mathbf{R},\mathbf{r})$
Rotation matrix	$U_{nm}(\mathbf{k})$	$U_{SM}(\mathbf{Q})$

Table 3.1: Notation for and analogy between electron and exciton Wannier functions and related parameters.

3.4 Methods and Computational Details

As previously emphasized the Wannierization procedure is independent of computational method used to compute excitonic properties. Popular methods include time-dependent density functional theory [10], equation of motion coupled cluster [82], and the *GW* plus Bethe-Salpeter equation (BSE) approach [12] to name a few. Here we adopt the latter method and summarize the approach below.

The BSE is a Dyson-like equation for the two-particle electron-hole propagator [12, 54, 55]. For computational tractability, the BSE is cast as an eigenvalue equation in a basis of electron-hole product states $\langle \mathbf{r}_e\mathbf{r}_h|cv\mathbf{k}\mathbf{Q}\rangle \equiv \psi_{c\mathbf{k}+\mathbf{Q}/2}(\mathbf{r}_e)\psi^{\star}_{v\mathbf{k}-\mathbf{Q}/2}(\mathbf{r}_h)$ and reads

$$(E_{c\mathbf{k}+\mathbf{Q}/2} - E_{v\mathbf{k}-\mathbf{Q}/2})A^{S\mathbf{Q}}_{cv\mathbf{k}} + \sum_{c'v'\mathbf{k}'} \langle cv\mathbf{k}\mathbf{Q}|K^{\text{ eh}}|c'v'\mathbf{k}'\mathbf{Q}\rangle\, A^{S\mathbf{Q}}_{c'v'\mathbf{k}'} = \Omega_{S\mathbf{Q}}A^{S\mathbf{Q}}_{cv\mathbf{k}}, \tag{3.10}$$

where $E_{n\mathbf{k}}$ are *GW* quasiparticle energies and K^{eh} is the electron-hole interaction kernel. Upon solving the BSE, one obtains exciton eigenenergies, $\Omega_{S\mathbf{Q}}$, and exciton wavefunctions in terms of the expansion coefficients, $A^{S\mathbf{Q}}_{cv\mathbf{k}}$, see Sec. 3.2.

When built atop GW, the electron-hole kernel appearing in Eq. 3.10 is expressed as the sum of two terms, $K^{\mathrm{eh}} = K^{\mathrm{D}} + 2\delta_S K^{\mathrm{X}}$, where K^D and K^{X} denote an attractive screened direct term and a repulsive bare exchange term, respectively, and δ_S is 1 for spin-singlet and 0 for spin-triplet excitons. Explicit expressions for K^{D} and K^{X} in the electron-hole product states basis are given in Ref. [55].

As a first application, we apply the above formalism to Wannierize the low-lying excitons in LiF, a prototypical wide band-gap insulator with weak dielectric screening and correspondingly strong electron-hole interactions. The lowest singlet exciton is strongly bound with binding energies on the order of 1.5 eV and a Bohr radius on the order of ~ 3.8 Å, about twice the size of the nearest neighbor separation 2.01 Å [85]. We note that LiF was one of the first systems studied within the *ab initio* GW plus BSE approach [12] while the closely related compound, LiCl, appeared in the original work on MLWFs [56].

The starting point for all calculations is a ground state density functional theory (DFT) calculation to obtain Kohn-Sham energies and eigenstates [26, 29]. In this work, we use `Quantum Espresso` [86]. We use a planewave basis set, the generalized gradient approximation of Perdew, Becke, and Ernzerhof (PBE) [87], and norm-conserving pseudopotentials taken from pseudo-dojo [88, 89]. To converge the ground state density we use an 80 Ry planewave cutoff and $8 \times 8 \times 8$ $\mathbf{k}$-grid. We then use `BerkeleyGW` [13] to perform a single-shot G_0W_0 calculation, computing the static dielectric function within the random phase approximation using a sum-over-bands approach [50, 51] in conjunction with a Hybertsen-Louie generalized plasmon-pole model to capture the frequency dependence [11]. In computing the susceptibility, χ_0, we include 90 unoccupied bands and use 10 Ry planewave cutoff. The same number of unoccupied bands is used to converge the Coulomb-hole contribution to the self-energy. The $\mathbf{k}$-grid used for our GW-BSE calculation is inherently linked to the $\mathbf{Q}$-grid used for Wannierization as explained in the following paragraph and generally differs from the $8 \times 8 \times 8$ grid used at DFT level.

In our BSE calculations of LiF, the electron-hole kernel, K^{eh}, is expanded in 1 conduction band and 3 valence bands. Our workflow requires exciton eigenenergies, $\Omega_{S\mathbf{Q}}$, and eigenstates, $\Psi_{S\mathbf{Q}}$, on a regular $\mathbf{Q}$-grid. As presently implemented, our formalism requires that the underlying $\mathbf{k}$-grid on which the BSE is solved be commensurate and twice as dense as the $\mathbf{Q}$-grid, a point further explained in Appendix A.1. To give an explicit example Wannierizing the exciton on a $5 \times 5 \times 5$ $\mathbf{Q}$-grid requires solving the BSE at 125 $\mathbf{Q}$-pts with the electron-hole kernel constructed on a $10 \times 10 \times 10$ $\mathbf{k}$-grid. In this work, no symmetry or interpolation scheme is used when building the electron-hole kernel.

In Fig. 3.3, we show the BSE-computed exciton dispersion for the eight lowest energy spin singlet (left panel) and triplet (right panel) bands. In the triplet case, we find that the excitons at $\mathbf{Q} = \mathbf{0}$ are three-fold degenerate. These three lowest exciton bands remain entangled throughout the Brillouin zone and are well separated from higher lying bands. By contrast, for spin-singlet excitons, the three-fold degeneracy at $\mathbf{Q} = \mathbf{0}$ is lifted by the exchange interaction, with the longitudinal branch higher in energy than the corresponding transverse branches [90]. The three lowest singlet bands are not entirely isolated from higher lying singlet states, however the disentanglement is fairly minimal occurring only near the

L points at the BZ edge.

Based on the exciton dispersion, we restrict our analysis to the subspace which contains the lowest three exciton bands. To initialize the Wannierization procedure, we use a product of hydrogen, 1s-like orbitals – explicitly $H_J(\mathbf{R},\mathbf{r}) = \psi_{1s}(\mathbf{R};a)\psi_{1s}(\mathbf{r};2a)$, where a denotes the lattice constant and $\psi_{1s}(\mathbf{r};a) = e^{-r/a}/\sqrt{\pi a^3}$. These trial orbitals are centered at the position of the fluoride atom. In this separable form, the projection matrix, $A^{\mathbf{Q}}_{SJ} = \langle \Psi_{S\mathbf{Q}}|H_J\rangle$, is more easily computed. We provide a detailed expression for this overlap in Appendix A.1.

3.5 Results

Q-grid	Ω	Ω_I	Ω_{OD}	Ω_D	WF spread
			Singlets		
$3\times3\times3$	4.755	4.718	0.037	0.0	1.594*
$4\times4\times4$	5.716	5.673	0.042	0.0	1.905
$5\times5\times5$	6.258	6.218	0.040	0.0	2.086
			Triplets		
$3\times3\times3$	3.882	3.866	0.017	0.0	1.294
$4\times4\times4$	4.332	4.320	0.012	0.0	1.444
$5\times5\times5$	4.591	4.581	0.011	0.0	1.531

Table 3.2: Minimized spread Ω for the triplet excitons in LiF and its decomposition into invariant, Ω_I, diagonal, Ω_D, and off-diagonal Ω_{OD} parts. The spread of the individual Wannier functions are reported in the final column. All values are reported in Å^2.

In Tab. 3.2 we report on the convergence of the Wannierization procedure with increasing **Q**-grid, decomposing the total spread, Ω, into its invariant, Ω_I, off-diagonal, Ω_{OD}, and diagonal, Ω_D, contributions. As discussed previously, the underlying **k**-grid is chosen twice as dense as the **Q**-grid. Despite this additional variability, we still observe clear convergence trends. The convergence of the total spread, Ω, is relatively slow, stemming primarily from the gauge invariant part of the spread, Ω_I, which is fixed after the disentanglement procedure is complete. By contrast the gauge dependent part of the spread, $\Omega_D + \Omega_{OD}$, the part which is actually minimized during the Wannierization procedure, converges rapidly with increasing **Q**-grid, changing by less than 0.002 Å^2 between the final two steps. This behavior is analogous, and the level of convergence in Ω similar, to what was reported at one-electron level by Marzari and Vanderbilt [56] in simple semiconducting systems.

In Fig. 3.1, we visualize the exciton Wannier orbitals, plotting $W_{M\mathbf{0}}(\mathbf{R},\mathbf{r}=\mathbf{0})$ vs. $\mathbf{R}$. Here, $W_{M\mathbf{0}}$ is the probability amplitude for finding the average electron-hole position at $\mathbf{R}$ given the relative electron-hole coordinate is $\mathbf{0}$, that is for $\mathbf{r}_e = \mathbf{r}_h$. We observe that the exciton Wannier function is well localized in $\mathbf{R}$ about the origin as expected. In analogy to

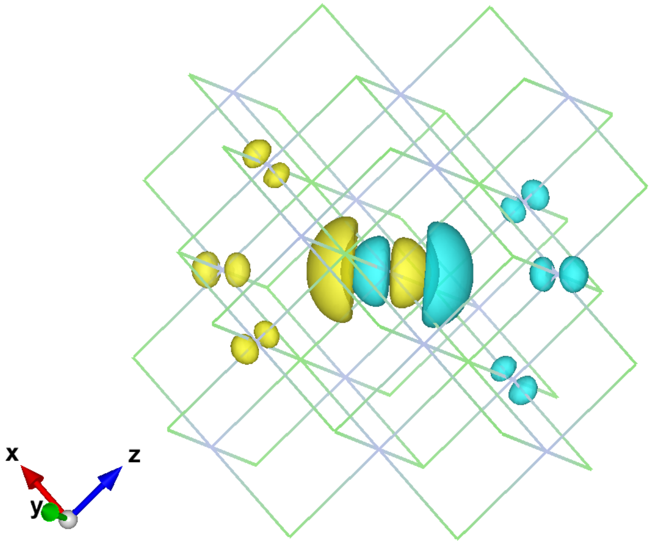

Figure 3.1: Triplet exciton Wannier function for LiF, plotted as a function of the average coordinate $\mathbf{R}$ with the relative coordinate $\mathbf{r} = \mathbf{0}$ – i.e. $W_{\mathbf{10}}(\mathbf{R}, \mathbf{0})$ vs. $\mathbf{R}$. Green and grey spheres denote Li and F atoms respectively. The Wannier function is entirely real so that yellow and blue lobes denote regions of positive and negative probability amplitude respectively.

the one-electron case, our numerical results indicate that the Wannierized excitons can be made entirely real through multiplication by a complex phase. Here we find $\mathrm{Im}W/\mathrm{Re}W = 0.001$. Further, we see the Wannier function transforms as an odd function under inversion symmetry and has a non zero dipole moment. This dipole moment gives rise to long-range dipole-dipole interactions between Wannier excitons (see Eq. 3.13 below) and drives the splitting of the longitudinal and transverse exciton branches to be discussed in Sec. 3.6.3.

3.6 Analytic Properties of the Exciton Wannier Functions and their Matrix Elements

3.6.1 Exponential localization of the exciton Wannier functions

An important analytic property of one-electron Wannier functions is their exponential localization in $\mathbf{r}_e$. In this section, we speculate on the existence of exponentially localized MLXWFs. We begin by reviewing the conditions for localization in the one-electron case and then comment on the possible extension to MLXWFs.

Early work on the subject, at the one-electron level, connected the exponential localization of one-electron Wannier functions to the analyticity of the Bloch periodic state, $u_{n\mathbf{k}}(\mathbf{r})$, in $\mathbf{k}$-space, throughout the Brillouin zone [91, 92]. Generally, for a composite set of entangled bands, $u_{n\mathbf{k}}(\mathbf{r})$ will not be analytic. However, in many cases, it is possible to rotate into a basis of quasi-Bloch states, defined as $v_{n\mathbf{k}} = \sum_m U_{mn}(\mathbf{k})u_{n\mathbf{k}}$, such that $v_{n\mathbf{k}}$ is analytic in $\mathbf{k}$. From simple Fourier analysis it is guaranteed that the Fourier transform of an analytic set of functions, in this case $v_{n\mathbf{k}}(\mathbf{r})$, will be exponential localized in $\mathbf{r}$ [92]. Recently, Panati et al. [93] proved that for one-electron Hamiltonians, $H(\mathbf{k}) = e^{-i\mathbf{k}\cdot\mathbf{r}}He^{i\mathbf{k}\cdot\mathbf{r}}$, which are both analytic in $\mathbf{k}$ and time-reversal symmetric, an analytic set of quasi-Bloch functions exist in 2 and 3 dimensions if, and only if, all Chern numbers of the system are zero. With these ingredients Brouder et al. [94] demonstrated that for real, square-integrable, one-electron potential, $V(\mathbf{r})$, it is possible to construct exponentially localized Wannier functions. They further demonstrated that the MLWFs procedure represents a unique path to the construction of these Wannier functions and when constructed in this way, the Wannier functions are real up to a global phase.

To adapt the above arguments to the exciton Wannier function case, we consider the BSE Hamiltonian, $H^{\mathrm{BSE}}(\mathbf{Q}) = e^{-i\mathbf{Q}\cdot\mathbf{R}}H^{\mathrm{BSE}}e^{i\mathbf{Q}\cdot\mathbf{R}}$. For spin triplet excitons, we expect $H^{\mathrm{BSE}}(\mathbf{Q})$ to be analytic in $\mathbf{Q}$, so that arguments above can be directly adapted to prove the exponential localization of triplet exciton Wannier functions, provided the system is time-reversal symmetric. By contrast, the spin-singlet Hamiltonian, has a well known non-analyticity stemming from the $\mathbf{Q} \to 0$ limit of the exchange term (see Sec. 3.6.3). This intrinsic non-analyticity violates one of the original assumptions of Prinati's work and the relation between the Chern numbers and analyticity of the quasi-Bloch states should be carefully revisited in this context before definitive statements about the analyticity of the Bloch states can be made.

A generalization of Panati's [93] work for spin-singlet exciton Wannier functions is beyond the scope of this work. However, even if this intrinsic non-analyticity turns out to prevent the exponential localization of the singlet MLXWF, it will not be detrimental to the approach here. For one, a term which contains the non-analytic contribution to the Hamiltonian can, in principle, always be isolated and subtracted to arrive at a sufficiently smooth $H^{\mathrm{BSE}}(\mathbf{Q})$ allowing for the exponential localization of MLXWFs. The non-analytic contribution can then be added back in post-processing. Finally, we note that in some systems, these questions are largely bypassed. For instance, in Sec. 3.6.3 we show that there is no non-analyticity associated high symmetry cubic systems including LiF studied here.

3.6.2 Decay of Matrix Elements in the Wannier Basis

Rapid decay of matrix elements of a general operator, $\mathcal{O}$, in the Wannier basis, $|\langle M\mathbf{0}|\mathcal{O}|N\bar{\mathbf{R}}\rangle|$, with increasing separation between Wannier orbitals, $\bar{R} = |\bar{\mathbf{R}}|$, hinges both on the exponential localization of the MLXWFs, discussed in Sec. 3.6.1., and the locality of the operator $\mathcal{O}$. In this section, we analyze the decay properties of the the screened direct, K^{D}, and bare exchange, K^{X}, operators in the MLXWF basis. The decay properties of these matrix elements have immediate consequences for the Wannier-Fourier interpolation of spin- singlet and triplet exciton dispersions as discussed in the subsequent section.

In the Wannier basis, the direct term takes the following form

$$\langle M\mathbf{0}|K^{\mathrm{D}}|N\bar{\mathbf{R}}\rangle = \frac{4\pi e^2}{V_{\mathrm{xtal}}}\int_{\mathrm{xtal}} W^{\star}_{M\mathbf{0}}(\mathbf{R},\mathbf{r})\varepsilon^{-1}(\mathbf{R},\mathbf{r})\frac{1}{r}W_{N\bar{\mathbf{R}}}(\mathbf{R},\mathbf{r})d^3\mathbf{R}d^3\mathbf{r}, \tag{3.11}$$

where $\varepsilon^{-1}(\mathbf{R},\mathbf{r})$ is the static inverse dielectric function, expressed in the average, $\mathbf{R}$, and relative, $\mathbf{r}$, coordinates. Assuming $W_{M\mathbf{0}}(\mathbf{R},\mathbf{r})$ and $W_{N\bar{\mathbf{R}}}(\mathbf{R},\mathbf{r})$ are exponentially localized in $\mathbf{R}$, about $\mathbf{0}$ and $\bar{\mathbf{R}}$ respectively, it follows that $|\langle M\mathbf{0}|K^{\mathrm{D}}|N\bar{\mathbf{R}}\rangle|$ also decays exponentially with increasing $\bar{R}$. This is especially obvious when local field effects are negligible and ε^{-1} depends only on $\mathbf{r}$. Then the the decay of the matrix element is proportional to the overlap of the two MLXWFs centered at $\mathbf{0}$ and $\bar{\mathbf{R}}$. However, even when local field effects are strong, the functional dependence of the integrand on $\mathbf{R}$ still implies exponential decay in $\bar{\mathbf{R}}$.

By contrast the exchange term takes the following form

$$\langle M\mathbf{0}|K^{\mathrm{X}}|N\bar{\mathbf{R}}\rangle = \frac{4\pi e^2}{V_{\mathrm{xtal}}}\int_{\mathrm{xtal}} W^{\star}_{M\mathbf{0}}(\mathbf{R},\mathbf{0})\frac{1}{|\mathbf{R}-\mathbf{R}'|}W_{N\bar{\mathbf{R}}}(\mathbf{R}',\mathbf{0})d^3\mathbf{R}d^3\mathbf{R}'. \tag{3.12}$$

In this case, the Coulomb interaction acts to couple exciton Wannier orbitals at different sites and $|\langle M\mathbf{0}|K^{\mathrm{X}}|N\bar{\mathbf{R}}\rangle|$ decays slowly. We can extract the analytic dependence of $|\langle M\mathbf{0}|K^{\mathrm{X}}|N\bar{\mathbf{R}}\rangle|$ on $\bar{R}$ in the large $\bar{\mathbf{R}}$ limit via a multipole expansion in the Coulomb interaction. This expansion is justified in the limit where $\bar{R}$ is much larger than the spatial extent of the MLXWFs in the $\mathbf{R}$ coordinate. Retaining only the lowest order dipole-dipole term, we arrive at

$$\langle M\mathbf{0}|K^{\;\mathrm{DD}}|N\bar{\mathbf{R}}\rangle = \frac{4\pi e^2}{V_{\mathrm{xtal}}}\left(\frac{\mathbf{p}^{\star}_M\cdot\mathbf{p}_N}{d^3} - 3\frac{(\mathbf{d}\cdot\mathbf{p}^{\star}_M)(\mathbf{d}\cdot\mathbf{p}_N)}{d^5}\right), \tag{3.13}$$

where $\mathbf{d}$ denotes the distance between Wannier centers, $\mathbf{d} = \bar{\mathbf{R}} + \boldsymbol{\tau}_M - \boldsymbol{\tau}_N$ and $\mathbf{p}_M$ denotes the dipole moment associated with the exciton Wannier function M, namely,

$$\mathbf{p}_M = \int_{\mathrm{xtal}} \mathbf{R}W_{M\mathbf{0}}(\mathbf{R},\mathbf{0})d^3\mathbf{R}. \tag{3.14}$$

From this analysis it is clear that when the exciton Wannier dipole moment is non-vanishing, $|\langle M\mathbf{0}|K^{\mathrm{X}}|N\bar{\mathbf{R}}\rangle|$ should decay as $1/|\bar{\mathbf{R}}|^3$. From Fig. 3.1, we clearly observe that the MLXWFs dipole moment is non-zero for LiF.

In Fig. 3.2 we plot the magnitude of the BSE Hamiltonian in the Wannier basis, $|\langle M\mathbf{0}|H^{\mathrm{BSE}}|N\bar{\mathbf{R}}\rangle|$, as a function of $\bar{R}$ in a manner similar to what is done in Ref. [62] for H^{DFT}. As expected, we observe that the triplet matrix elements decay exponentially in $\bar{R}$ while the singlet matrix elements appear to decay more slowly, though it is difficult to extract the exact functional dependence without going to larger $\bar{R}$. Unfortunately going to larger $\bar{R}$ requires denser $\mathbf{Q}$-grids and is prohibitively expensive.

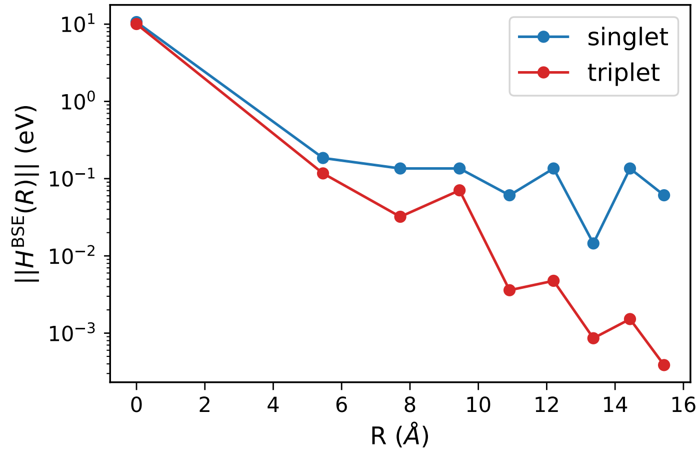

Figure 3.2: Spatial decay of the singlet and triplet BSE Hamiltonian in the Wannier representation $\langle M\mathbf{0}|H^{\rm BSE}|N\mathbf{R}\rangle$ as a function of R for LiF. The data points correspond to the largest value of the matrix element at a give R – i.e. $||H(R)|| = \max_{MN,|\mathbf{R}|=R} | \langle M\mathbf{0}|H^{\rm BSE}|N\mathbf{R}\rangle |$.

3.6.3 On the Relation Between the Dipole-Dipole Interactions and Non-analyticity

It is well known that long range dipole-dipole interactions, discussed in the previous subsection, give rise to the non-analyticity and ultimately the splitting of the longitudinal and transverse branches (LT-splitting) of the exciton bandstructure at $\mathbf{Q} = 0$ [80, 81]. To see how this comes about in our present formalism, we rotate Eq. 3.13 into the exciton basis to obtain

$$\begin{aligned} \langle S\mathbf{Q}|K^{\rm DD}|S'\mathbf{Q}\rangle &= \frac{4\pi e^2}{V_{\rm xtal}} \sum_{MN} U^{\dagger}_{SM}(\mathbf{Q})\; U_{NS'}(\mathbf{Q}) \\ &\times \sum_{\mathbf{G}} \frac{[\mathbf{p}_M\cdot(\mathbf{Q}+\mathbf{G})][\mathbf{p}_N\cdot(\mathbf{Q}+\mathbf{G})]}{|\mathbf{Q}+\mathbf{G}|^2} e^{i(\mathbf{Q}+\mathbf{G})\cdot(\boldsymbol{\tau}_M-\boldsymbol{\tau}_N)}, \end{aligned} \tag{3.15}$$

where $\mathbf{G}$ denotes a reciprocal lattice vector. Taking the $\mathbf{Q}\to 0$ limit of the above expression we arrive at

$$\langle S\mathbf{Q}|K^{\rm NA}|S'\mathbf{Q}\rangle = \frac{4\pi e^2}{V_{\rm xtal}} \frac{(\mathbf{Q}\cdot\mathbf{p}^{\star}_S)(\mathbf{Q}\cdot\mathbf{p}_{S'})}{Q^2}, \tag{3.16}$$

where we have used $\mathbf{p}_S = \sum_M U_{MS}(\mathbf{0})\mathbf{p}_M$. As a direct result of dipole-dipole interactions, exciton eigenvalues can exhibit rapid angular variation about the origin $\mathbf{Q} = 0$ and may appear discontinuous when plotted along certain directions in reciprocal space. This non-analyticity is known [2, 54, 80, 81] and was recently revisited in the context of first principles BSE [55, 74] where the diagonal part of Eq. 3.16 was derived by directly taking the $\mathbf{Q}\to\mathbf{0}$

limit of $\langle S\mathbf{Q}|K^{\mathrm{X}}|S\mathbf{Q}\rangle$. Our present derivation highlights that this non-analytic behavior can be recast as stemming entirely from dipole-dipole interactions between MLXWFs, providing an alternative to associating it with dipole moments of product states of electron-hole Wannier functions as demonstrated in Ref. [54] (and the discussion around Eq. 11.20).

In LiF, the non-analytic contribution is independent of $\mathbf{Q}$. To see this, denote the longitudinal and transverse excitons by $|S_L\rangle$ and $|S_T\rangle$ respectively. We then find $\langle S_L\mathbf{Q}|K^{\,\mathrm{NA}}|S_L\mathbf{Q}\rangle = \Delta_{\mathrm{LT}}$ where $\Delta_{\mathrm{LT}} = 4\pi e^2|\mathbf{p}_S|^2/V_{\mathrm{xtal}}$ while $\langle S_L\mathbf{Q}|K^{\,\mathrm{NA}}|S_T\mathbf{Q}\rangle = \langle S_T\mathbf{Q}|K^{\,\mathrm{NA}}|S_T\mathbf{Q}\rangle = 0$. The analysis implies that the longitudinal exciton eigenergies should, be rigidly shifted relative to the two transverse branches. Indeed this behavior is corroborated by our BSE calculation (see Fig. 3.3). Importantly, our analysis and numerical results demonstrate that $\Omega_{S\mathbf{Q}}$, and more generally $H^{\mathrm{BSE}}(\mathbf{Q})$, remain analytic as $\mathbf{Q}\to\mathbf{0}$, a feature not shared in lower symmetry systems where the non-analyticity is expected and will manifest as kinks or discontinuities in the exciton dispersion [74]. In LiF, this simple behavior stems from the underlying cubic symmetry [90].

3.7 Wannier-Fourier Interpolation

At the one-electron level, a major benefit of working in the Wannier basis is that matrix elements of the form $|\langle m\mathbf{0}|\mathcal{O}|n\bar{\mathbf{R}}\rangle|$ decay rapidly with increasing $\bar{R}$. In turn, this allows for efficient Wannier-Fourier interpolation [62]. For instance taking $\mathcal{O}$ to be the one-particle DFT Hamiltonian, $H^{\,\mathrm{DFT}}$, an efficient scheme for interpolating DFT eigenvalues involves first Fourier transforming $\langle m\mathbf{0}|H^{\,\mathrm{DFT}}|n\bar{\mathbf{R}}\rangle$ to an arbitrary $\mathbf{k}$-point to obtain $H^{\mathrm{DFT}}_{mn}(\mathbf{k})$ and subsequently diagonalizing this matrix to arrive at DFT eigenvalues, $\epsilon_{n\mathbf{k}}$, and Wannier rotation matricies, $U_{mn}(\mathbf{k})$. The success of this method depends critically on the spatial localization of $|\langle m\mathbf{0}|H^{\mathrm{DFT}}|n\bar{\mathbf{R}}\rangle|$.

To interpolate exciton eigenenergies, $\Omega_{S\mathbf{Q}}$, in the same manner, $|\langle M\mathbf{0}|H^{\mathrm{BSE}}|N\bar{\mathbf{R}}\rangle|$ must decay rapidly with increasing $\bar{R}$. In Sec. 3.6.2, we found that while $|\langle M\mathbf{0}|K^{\mathrm{D}}|N\bar{\mathbf{R}}\rangle|$ decays exponentially in $\bar{R}$, $\langle M\mathbf{0}|K^{\mathrm{X}}|N\bar{\mathbf{R}}\rangle$ decays slowly in the same variable, namely as $1/|\bar{\mathbf{R}}|^3$. Further, in Sec. 3.6.3., we showed that the exchange term can give rise to non-analyticities in the exciton dispersion. As a direct consequence, we expect the Wannier-Fourier interpolation scheme to work well for spin-triplet excitons but to require further modifications for the spin-singlet case.

If Fig. 3.3 we show the results of our Wannier-Fourier interpolated exciton dispersion for LiF. In blue, we plot the singlet and triplet exciton dispersion obtained through explicitly diagonalizing the BSE Hamiltonian at 72 $\mathbf{Q}$-points along a high symmetry path. In red we overlay our Wannier-Fourier interpolated exciton dispersion, starting from a $4\times4\times4$ coarse $\mathbf{Q}$-grid. We find that applying the usual Wannier-Fourier interpolation scheme without modification gives excellent agreement for the spin-triplet exciton dispersion.

By contrast, for the spin-singlet exciton we see a large discrepancy between the Wannier-Fourier and BSE result at the origin. This discrepancy stems from the long-range dipole-dipole contribution to the spin-singlet kernel, see 3.13. One strategy to correct for this is to first subtract the real space, dipole-dipole contribution (see Eq. 3.13) from $\langle M\mathbf{0}|H^{\mathrm{BSE}}|N\bar{\mathbf{R}}\rangle$, Wannier-Fourier interpolate the remaining short-range part of the BSE Hamiltonian, and finally add the dipole-dipole contribution back on the interpolated grid in reciprocal space (see Eq. 3.15). A similar strategy is used to interpolate phonon frequencies in polar materials [95]. Here however the procedure is complicated by the fact that the dipoles, $\mathbf{p}_N$, are not known *a proiri*. Further the dipole-diople interaction $\langle M\mathbf{0}|K^{\mathrm{DD}}|N\bar{\mathbf{R}}\rangle$ tends to couple the lowest three exciton states with states outside the Wannierization window. This further complicates the proceedure and suggests that a set of 3 effective $\mathbf{p}_N$ should be used however the procedure for calculating these dipole moments is far from clear. The implementation of such a procedure will be left to future work.

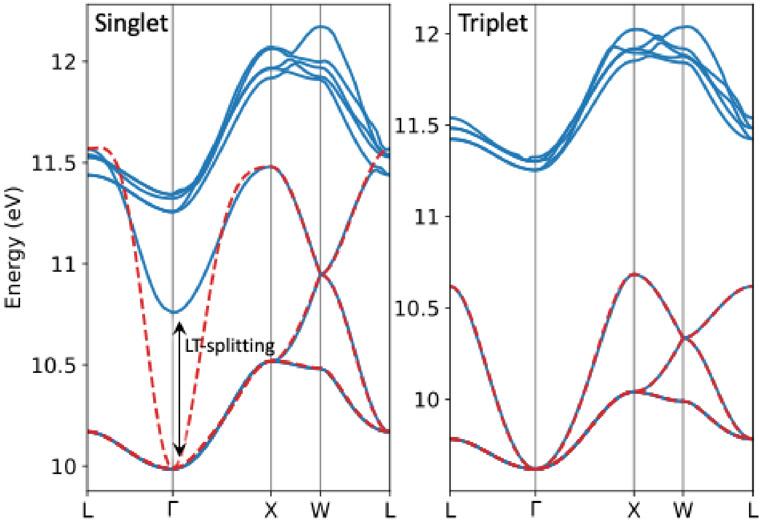

Figure 3.3: Singlet (left panel) and triplet (right panel) exciton dispersion. The solid blue curve is the result of our explicit BSE calculation while the dotted red curve is obtained through Wannier-Fourier interpolation. We have indicated the splitting of the longitudinal and transverse bands in the singlet dispersion.

3.8 On the Relation Between the Exciton Wannier Function and the Frenkel Exciton

An attractive feature of one-electron Wannier functions is their relation to linear combinations of atomic orbitals used in the construction of tight binding models. The relation often allows the practitioner to build chemical intuition especially in the context of understanding the role of chemical bonds in solid state systems.

In this section we show there is an analogous relation between the exciton Wannier functions and linear combinations of singly-excited molecular orbitals used as a basis in Frenkel's description [6] of the exciton. We begin by first reviewing the connection between one-electron Wannier functions and linear combinations of atomic orbitals and subsequently provide an analogous discussion for exciton Wanner functions.

Recall that in the tight-binding approximation, the one-electron Bloch state can be expressed as a sum over linear combinations of atomic-centered orbitals, namely

$$\psi_{n\mathbf{k}}(\mathbf{r}) = \sum_{m\bar{\mathbf{R}}} e^{i\mathbf{k}\cdot\bar{\mathbf{R}}} c_{mn} \phi_m(\mathbf{r}-\bar{\mathbf{R}}), \tag{3.17}$$

where $\phi_m(\mathbf{r}-\bar{\mathbf{R}})$ denotes an atomic-centered orbital with principle quantum number m and the coefficients c_{mn} are the expansion coefficients. (For simplicity we assume a Bravais lattice with only one site per cell.)

Meanwhile, the one-electron Wannier functions, $w_{n\bar{\mathbf{R}}}(\mathbf{r})$, by definition, are related to Bloch states through

$$\psi_{n\mathbf{k}}(\mathbf{r}) = \sum_{\bar{\mathbf{R}}} e^{i\mathbf{k}\cdot\bar{\mathbf{R}}} w_{n\bar{\mathbf{R}}}(\mathbf{r}), \tag{3.18}$$

where, for simplicity and to avoid proliferation of indices, we have omitted the Wannier rotation matrices. It should be noted that by definition, $w_{n\bar{\mathbf{R}}}(\mathbf{r})$ are chosen so as to reproduce the true Bloch state, that is they are rigorously Fourier expansion coefficients. This should be distinguished from the Eq. 3.17, where c_{mn} are determined through solving the Schrodinger equation and generally give only an approximate representation of the Bloch state as a result of the finite atomic-centered basis set. Nevertheless, the functional form of these two representations suggests the Wannier orbitals can be interpreted as a minimal tight-binding basis and in some cases may shed light on convalency, ionicity, and hybridization of chemical bonds as discussed in Ref. [20].

Frenkel's description of an exciton is analogous to the tight-binding representation at one-electron level. When the exciton radius is small so that the electron and hole reside mostly on a single molecule (or atom or site depending on the system) it is convenient to expand the exciton wavefunction as a sum over singly-excited site-centered orbitals, explicitly

$$\Psi_{S\mathbf{Q}}(\mathbf{r}_e,\mathbf{r}_h) = \sum_{\bar{\mathbf{R}}cv} e^{i\mathbf{Q}\cdot\bar{\mathbf{R}}} C_{Scv} \chi_c(\mathbf{r}_e-\bar{\mathbf{R}}) \chi_v^\star(\mathbf{r}_h-\bar{\mathbf{R}}) \tag{3.19}$$

where $\chi_n(\mathbf{r})$ denotes a molecular orbital with principle quantum number n so that $\chi_c(\mathbf{r}_e - \bar{\mathbf{R}})\chi_v^\star(\mathbf{r}_h-\bar{\mathbf{R}})$ denotes a singly-excited molecular orbital centered at $\bar{\mathbf{R}}$, where one electron has been removed from orbital v and promoted to orbital c. Analogous to the tight-binding case, Eq. 3.19, is only an approximate representation of the excitonic state, with the expansion coefficient chosen to diagonalize the BSE in this restricted basis.

It is interesting to compare Eq. 3.19 to the exciton expanded in terms of the exciton Wannier functions. Inverting Eq. 3.4 and reexpressing the wavefunction in electron and hole coordinates we find,

$$\Psi_{S\mathbf{Q}}(\mathbf{r}_e, \mathbf{r}_h) = \sum_{\bar{\mathbf{R}}} e^{i\mathbf{Q}\cdot\bar{\mathbf{R}}} W_{S\bar{\mathbf{R}}}(\mathbf{r}_e, \mathbf{r}_h). \tag{3.20}$$

Comparing Eq. 3.20 with Eq. 3.19, we immediately see the relation between exciton Wannier functions and Frenkel like excitons. Our analysis suggests that the exciton Wannier functions can be used to build chemical intuition especially in the Frenkel limit.

3.9 Conclusion and Outlook

In this work we have outlined a procedure for constructing maximally localized exciton Wannier functions. Our analysis helps to connect the classic Mott-Wannier and Frenkel pictures of excitons in a first principle context further bridging the gap between condensed matter and quantum chemistry methods for computing neutral excitations. We have benchechmarked our work on LiF, demonstrating the exciton Wannier-orbitals converge smoothly with **Q**-grid and can be used for post-processing applications, like Wannier-Fourier interpolation of the exciton dispersion. We expect this work will serve as a staring point for many other post-processing applications, for instance calculations related to the Berry curvature of the exciton bands. Finally, we note that in this work, we have generalized the 1-particle Wannierization procedure to handle a specific 2-particle excitation (the exciton). In theory this procedure may readily be adapted to handle other 2-particle excitations, for example the bipolaron, as well as excitations involving more than two particles, for instance, trions and bi-excitons.

Chapter 4

A Unified Ab-initio Framework for Phonon-Based Exciton Transport in Solids: The Case of Acene Crystals

4.1 Introduction

Exciton diffusion is of critical importance in next-generation organic photovoltaic and light-emitting diode devices, where strongly bound photo-excited excitons must first migrate to an interface before charge separation or recombination can occur [96]. Despite its importance, there are few fully *ab initio* treatments of exciton transport and no framework capable of handling different limits at the same level of theory e.g. diffusion vs. hopping. A major challenge is that the two standard limits of exciton diffusion – wave or band-like propagation vs. hopping [97, 98] – are not always tractable on the same footing or level of theory.

This challenge is particularly relevant to organic semiconductors, a promising class of materials for optoelectronic applications with strong electron-hole and electron-phonon interactions. In these systems, long-range van der Waals interactions promote crystallization with intermolecular separations typically on the order of ∼5Å– a length scale which favors relatively localized excitons. At the same time, because these organic materials are composed of light elements, the excitons couple strongly to lattice vibrations. Both these features tend to promote exciton self-trapping and exciton-polaron formation. Band-like exciton diffusion may be inappropriate, with hopping theories emerging as a better description of exciton migration. At the same time, the breakdown may not be so severe as to completely invalidate the band-like theories, and studying exciton transport from both perspectives would be enlightening.

The interplay between band and hopping-like transport regimes has a long and established history. It was originally investigated by Holstein [99] in the one-dimensional molecular crystal limit with Lang and Firsov later reformulating the approach in terms of the modern language of canonical transformations [21]. Around the same time, Toyozawa reexpressed

Bardeen's original Hamiltonian [100] – which described a single electron coupled linearly to a bath of harmonic phonons – in the excitonic basis, demonstrating that the effective exciton-phonon vertex can be expressed as a contraction of the electron (hole)-phonon vertices and exciton expansion coefficients [24]. Working with the single-band Hamiltonian of Toyozawa and leveraging the canonical transform of Lang and Firsov, Silbey and Munn later conducted an extensive analysis of phonon-based exciton diffusion arguing that charge and exciton transport always has some coherent band-like and incoherent hopping-like component [101]. Later, Silbey and Munn generalized their method to include nonlocal, also known as off diagonal, or Peierls, coupling [102]. More recently it has been argued that dynamics disorder, stemming from the aforementioned nonlocal coupling, may be particularly important in molecular crystals and gives rise to a regime where charge transport is mediated through transient localization [103]. A comprehensive discussion of the different regimes of charge and exciton transport can be found in Ref. [104].

While extensive prior work at the model Hamiltonian level undoubtedly lays a strong theoretical foundation for studying exciton transport, the problem of how best to construct and parameterize non-empirical Hamiltonians which describe the coupled exciton-phonon system remains an open question. This question is particularly pressing in organic crystals where *ab initio* calculations have established that lattice vibrations are complex in nature [105] coupling through different mechanisms to electronic degrees of freedom and for which exciton properties can be tuned depending on monomer, packing, and functionalization [73].

The majority of first-principles studies of exciton transport in organic materials have focused on a single aspect or regime of transport. For instance, in the strong lattice coupling regime, Marcus theory [106–108] or small-polaron theory [109] is often used. To the best of our knowledge, a thorough *ab initio* investigation of band-like exciton transport in organic crystals has yet to be performed. However there exist studies of charge transport in organic crystals using the Boltzmann equation, within the relaxation time approximation [110, 111] and in this work we will show how this approach can be trivially extended to neutral excitations. These works, which rely on perturbation theory in one of two limits, provide excellent insight into the microscopic nature of diffusion in their respective regimes but alone tell only part of the story and are often hard to compare given the different underlying computational frameworks.

To investigate the role of dynamic disorder, simplified Su-Schrieffer-Heeger-like Hamiltonians [112] have been parameterized from *ab initio* and real-time propagation performed using Ehrenfest [113] and QM/MM [114] procedures. By mapping to simplified models, these works broaden our understanding but at the expense of coarse graining many important microscopic details so that some predictive power is lost. At the other end of the spectrum, multi-scale studies of exciton diffusion combining non-adiabatic molecular dynamics, time-dependent density functional theory, and Monte-Carlo simulation [115, 116] provide an entirely non-empirical, although approximate, description of exciton diffusion; however, the fundamental mechanisms at play may be obscured by the complexity of such approaches.

The purpose of this work is to construct a unified starting point for studying exciton transport which both incorporates all microscopic parameters at the *ab initio* level while simultaneously remaining flexible enough to study exciton transport in the various regimes discussed above. Our reciprocal space-based, Green's function approach marries state-of-the-art density functional perturbation theory for describing phonon related quantities with the *ab-initio GW* plus Bethe-Salpeter equation approach for capturing excitonic properties. The consistent construction of such a starting point is complicated by the very different nature of the neutral excitation in the extreme band-like and hopping limits. A central feature of this work is the non-trivial extension of the Lang-Firsov polaron transformation to the multi-band case allowing us to pass freely between the extended Bloch exciton and localized exciton-polaron description of neutral excitations. Our generalized Lang-Firsov transformation introduces some gauge freedom and in general there are an infinity of ways to pass between the two descriptions. Here, we fix this gauge freedom using the recently developed maximally localized exciton Wannier functions discussed in the previous chapter. We use this framework to study the exciton diffusion of low-energy triplets in crystalline acenes, focusing on extreme band-like and hopping limits for now, reserving the careful study of nonlocal coupling for future works.

4.2 The Coupled Exciton-Phonon Hamiltonian

In this work, we consider a Hamiltonian which describes excitons coupled linearly to a bath of harmonic phonons with the following Hamiltonian

$$\mathcal{H} = \sum_{S\mathbf{Q}} \Omega_{S\mathbf{Q}} c^\dagger_{S\mathbf{Q}} c_{S\mathbf{Q}} + \sum_{\mathbf{q}\nu} \omega_{\mathbf{q}\nu} b^\dagger_{\mathbf{q}\nu} b_{\mathbf{q}\nu} + \sum_{SS'\mathbf{Q}\mathbf{q}\nu} \mathcal{G}_{S'S\nu}(\mathbf{Q},\mathbf{q}) c^\dagger_{S'\mathbf{Q}+\mathbf{q}} c_{S\mathbf{Q}} (b^\dagger_{-\mathbf{q}\nu} + b_{\mathbf{q}\nu}), \tag{4.1}$$

where $c^\dagger_{S\mathbf{Q}}$ ($c_{S\mathbf{Q}}$) and $b^\dagger_{\mathbf{q}\nu}$ ($b_{\mathbf{q}\nu}$) are exciton creation (annihilation) and phonon creation (annihilation) operators, respectively. The first term describes the free propagation of a Bloch-type exciton with dispersion, $\Omega_{S\mathbf{Q}}$, where S and $\mathbf{Q}$ denote the principle quantum number and center-of-mass momentum of the exciton respectively while the second term describes a bath of harmonic phonons with dispersion $\omega_{\mathbf{q}\nu}$, where ν and $\mathbf{q}$ denote the phonon branch index and crystal momentum respectively. Finally $\mathcal{G}_{S'S\nu}(\mathbf{Q},\mathbf{q})$ is the exciton-phonon vertex which encodes the probability amplitude for a phonon in state $\mathbf{q}\nu$ to scatter an exciton from state $S\mathbf{Q}$ to $S'\mathbf{Q}+\mathbf{q}$ described in Chap. 2.

4.3 Exciton Diffusion in the Band-like Regime

If the third term appearing in Eq. 4.1 is small, it may be treated perturbatively. In this limit, the exciton can be viewed as propagating freely and is only occasionally scattered by a phonon. This is the so called band-like regime, and, after thermal equilibrium has been reached, the diffusion coefficient is given by

$$D_{\alpha\beta}^{\text{band}} = \frac{1}{N_{\mathbf{Q}}} \sum_{S\boldsymbol{Q}} p_{S\mathbf{Q}} (\mathbf{v}_{S\mathbf{Q}})_{\alpha} (\mathbf{v}_{S\mathbf{Q}})_{\beta} \tau_{S\mathbf{Q}}, \tag{4.2}$$

where $p_{S\mathbf{Q}}$ is the normalized probability to find an exciton in state $(S\boldsymbol{Q})$ at thermal equilibrium, $(v_{S\mathbf{Q}})_{\alpha} = \nabla_{\mathbf{Q}\alpha} \Omega_{S\mathbf{Q}}$ is the exciton band velocity in the α-direction, and $\tau_{S\mathbf{Q}}$ is the state-dependent relaxation time, i.e., the average time between phonon scattering events. From Fermi's Golden rule

$$\frac{1}{\tau_{S\mathbf{Q}}} = \frac{2\pi}{\hbar} \frac{1}{N_{\mathbf{q}}} \sum_{S'\nu\mathbf{q},\pm} |\mathcal{G}_{S'S\nu}(\mathbf{Q},\mathbf{q})|^2 \times \left(n_{\mathbf{q}\nu} + \frac{1}{2} \pm \frac{1}{2} \right) \delta(\Omega_{S\mathbf{Q}} - \Omega_{S'\mathbf{Q}+\mathbf{q}} \mp \omega_{\mathbf{q}\nu}), \tag{4.3}$$

where $n_{\mathbf{q}\nu}$ is the Bose-Einstein occupation factor for phonons and the sum over ± denotes summing over both the phonon emission and absorption channels.

In the opposite limit, i.e. when the exciton-phonon coupling is large, it is no longer appropriate to treat the third term in Eq. 4.1 as a small perturbation. In this limit, the Hamiltonian in Eq. 4.1 may not be an ideal starting point for studying exciton diffusion; it is more appropriate to transform to a localized description of the exciton as detailed in the next section.

4.4 The Exciton-Phonon Hamiltonian in the MLXWF Basis

In the limit where the coupling to the lattice is very large, it may be energetically more favorable for the exciton to be localized and the lattice to deform about the excitation. As presently written, the Hamiltonian in Eq. 4.1 is expressed in terms of creation and annihilation operators for extended Bloch-type excitons. To facilitate the discussion of exciton hopping, it is helpful to rotate to a localized basis. In the previous chapter, we outlined a prescription for passing to a maximally localized representation of the exciton state. Here we will use these MLXWFs as a basis for studying exciton transport from a localized perspective.

To construct MLXWFs for the acenes, we work in the subspace of the lowest two excitonic states. This choice is guided by the fact that there are two nonequivalent molecules per unit cell. In Fig. 4.1 we depict one MLXWF for anthracene. We find that the MLXWF is well localized on a single molecule. There exists a second MLXWF (not shown here) which sits on the second molecule in the unit cell. As discussed in Chap. 2, the exchange term in the BSE Hamitlonain prevents the straightforward application of the MLXWF methodology to spin-singlet excitons. For the moment we restrict our attention to spin-triplet excitons. In Sec. 4.12 we outline the extension to the spin-singlet case.

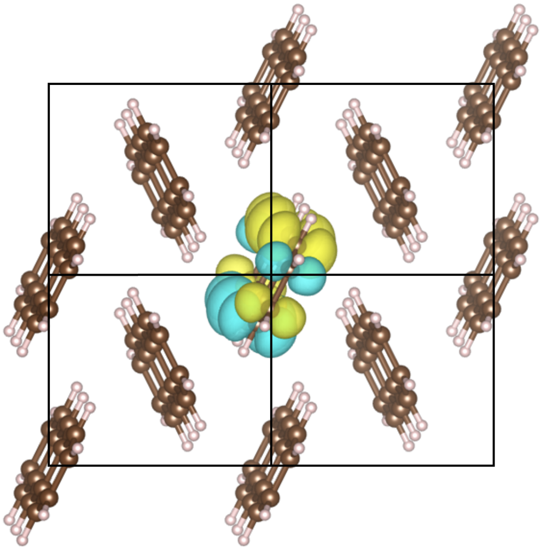

Figure 4.1: MLXWF for anthracene plotted as a function of the average coordinate $\mathbf{R}$ with the relative coordinate $\mathbf{r} = \mathbf{0}$ – i.e. $W_{\mathbf{10}}(\mathbf{R}, \mathbf{0})$ vs. $\mathbf{R}$. The Wannier function is entirely real so that yellow and blue lobes denote regions of positive and negative probability amplitude respectively.

In the following discussion, we re-express Eq. 4.1 in a basis of MLXWFs. In operator form, the transformation between exciton Bloch functions and MLXWFs reads

$$\begin{aligned} c^\dagger_{m\mathbf{R}} &= \sum_{S\mathbf{Q}} e^{-i\mathbf{Q}\cdot\mathbf{R}} U_{Sm}(\mathbf{Q}) c^\dagger_{S\mathbf{Q}} \\ c^\dagger_{S\mathbf{Q}} &= \frac{1}{N_{\mathbf{R}}} \sum_{m\mathbf{R}} e^{i\mathbf{Q}\cdot\mathbf{R}} U^\dagger_{mS}(\mathbf{Q}) c^\dagger_{m\mathbf{R}}, \end{aligned} \tag{4.4}$$

where $c^\dagger_{m\mathbf{R}}$ is the operator associated with the creation of a localized excitonic state on the m^{th} molecular site, $\mathbf{R}$ unit cells away from some origin, and $U_{Sm}(\mathbf{Q})$ are the Wannier rotation matrices discussed in Chap. 2.

With these transformations we rewrite Eq. 4.1 in the Wannier basis as

$$\begin{aligned} \mathcal{H}^{\mathrm{W}} = &\sum_{m\mathbf{R}n\mathbf{R}'} V_{mn}(\mathbf{R}-\mathbf{R}') c^\dagger_{m\mathbf{R}} c_{n\mathbf{R}'} + \sum_{\mathbf{q}\nu} \omega_{\mathbf{q}\nu} b^\dagger_{\mathbf{q}\nu} b_{\mathbf{q}\nu} \\ &+ \sum_{mn\mathbf{R}\mathbf{R}'\mathbf{q}\nu} e^{-i\mathbf{q}\cdot\mathbf{R}} \mathcal{G}^{\mathrm{W}}_{mn\nu}(\mathbf{R}-\mathbf{R}', \mathbf{q}) c^\dagger_{m\mathbf{R}} c_{n\mathbf{R}'} (b^\dagger_{-\mathbf{q}\nu} + b_{\mathbf{q}\nu}), \end{aligned} \tag{4.5}$$

where the couplings, $V_{mn}(\mathbf{R})$ and $\mathcal{G}^{\mathrm{W}}_{mn\nu}(\mathbf{R}, \mathbf{q})$ are related to the Wannier rotation matrices through

$$V_{mn}(\mathbf{R}) = \sum_{S\mathbf{Q}} e^{-i\mathbf{Q}\cdot\mathbf{R}} U^{\dagger}_{mS}(\mathbf{Q}) \Omega_{S\mathbf{Q}} U_{Sn}(\mathbf{Q}) \tag{4.6}$$

and

$$\mathcal{G}^{W}_{mn\nu}(\mathbf{R},\mathbf{q}) = \sum_{SS'\mathbf{Q}} e^{-i\mathbf{Q}\cdot\mathbf{R}} U^{\dagger}_{mS'}(\mathbf{Q}+\mathbf{q}) \mathcal{G}_{S'S\nu}(\mathbf{Q},\mathbf{q}) U_{Sn}(\mathbf{Q}). \tag{4.7}$$

Physically, $V_{mn}(\mathbf{R}-\mathbf{R}')$ and $\mathcal{G}^{\mathrm{W}}_{mn\nu}(\mathbf{R}-\mathbf{R}',\mathbf{q})$ are couplings associated with exciton hopping from molecular site $n\mathbf{R}'$ to $m\mathbf{R}$. The former is a purely electronic coupling stemming from exciton wavefunction overlap while the latter derives from coupling to the lattice and can be thought of as the probability amplitude for an exciton to hop from site $n\mathbf{R}'$ to $m\mathbf{R}$ accompanied by the emission or absorption of a phonon labeled by $\mathbf{q}\nu$. In this basis, it is conventional to further decompose $\mathcal{G}^{W}_{mn\nu}(\mathbf{Q},\mathbf{q})$ into a local ($n\mathbf{R} = m\mathbf{R}$) and nonlocal ($n\mathbf{R}' \neq m\mathbf{R}$) contribution, a point we will take up in the next section.

4.5 Local vs. Nonlocal Exciton-Phonon Coupling

The relative proportions of local vs. nonlocal exciton-phonon coupling in organic materials has been identified as a critical factor in further determining the diffusive mechanism for both charge and exciton transport. Two theoretical pictures are commonly invoked. When exciton-phonon coupling is predominantly local, it may be energetically more favorable for the exciton to localize and the lattice to relax about the exciton. It is appropriate to think of the exciton and deformed lattice as a single quantum mechanical state – an exciton-polaron [101]. The motion of the exciton-polaron is still inherently diffusive however in this case the exciton-polaron defaults to remaining localized about a lattice site, and hops to a nearby site when there is sufficient thermal energy.

By contrast, when the nonlocal coupling dominates, we can think of exciton-phonon interaction as modifying the hopping integrals, $V_{mn}(\mathbf{R})$. This coupling is often referred to as Peierl's coupling. Molecular dynamics simulations [103] have revealed that in this regime exciton diffusion decreases with increasing temperature, similar to the band-like mechanism. This mechanism has been proposed as a possible explanation for the high mobilities of observed in certain organic semiconductors, like rubrene, despite the fact that mean free paths in these materials at room temperature are on the order of the intermolecular separation.

To determine which transport regime is most appropriate for studying triplet exciton diffusion in acene crystals, we plot the relative contributions of the local and nonlocal exciton-phonon coupling in Fig. 4.2. In each panel, we plot the local, $g^2F_{\mathrm{loc}}(\omega)$, and nonlocal

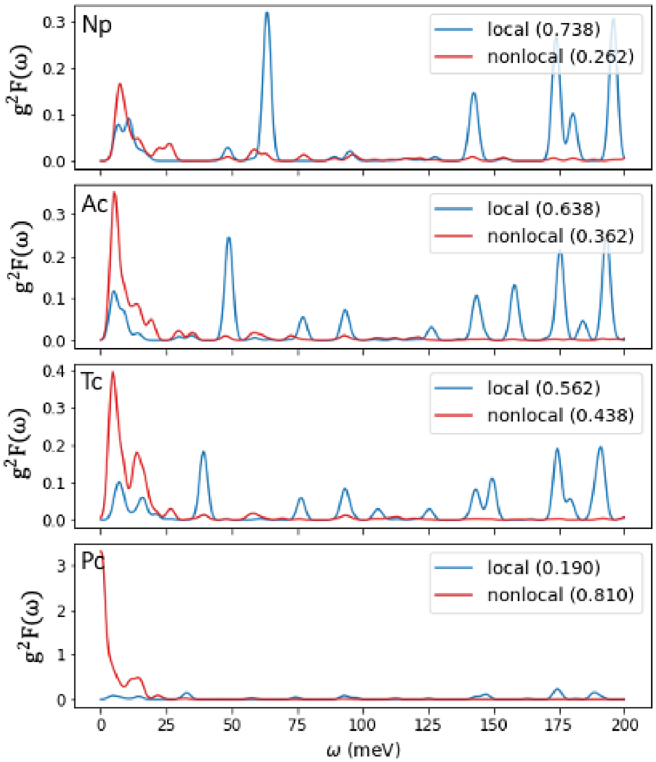

Figure 4.2: Local and nonlocal, exciton-phonon matrix element spectral decompositions computed according to Eq. 4.8 for all acenes. The numbers in the legend give the relative percentages of local and nonlocal coupling in these materials.

$g^2F_{\text{nonloc}}(\omega)$, spectral decompositions of the coupling defined as

$$\begin{aligned} g^2F_{\text{loc}}(\omega) &= \frac{1}{N_{\mathbf{q}}} \sum_{m\mathbf{q}\nu} \frac{|\mathcal{G}_{mm\nu}(\mathbf{0},\mathbf{q})|^2}{\omega_{\mathbf{q}\nu}} \delta(\omega - \omega_{\mathbf{q}\nu}) \\ g^2F_{\text{nonloc}}(\omega) &= \frac{1}{N_{\mathbf{q}}} \sum_{\mathbf{q}\nu,(n\mathbf{0})\neq(m\mathbf{R})} \frac{|\mathcal{G}_{mn\nu}(\mathbf{R},\mathbf{q})|^2}{\omega_{\mathbf{q}\nu}} \delta(\omega - \omega_{\mathbf{q}\nu}) \end{aligned} \tag{4.8}$$

Our analysis not only shows which type of coupling is dominant across the acenes but also clearly deptticts which phonons contribute most to this type of coupling. Several global trends appear. First, across all materials, we notice that the nonlocal coupling is mediated primarily by low energy phonons with energies below 30 meV. This is to be expected, such modes involve intermolecular sliding motions. It is easy to imagine how such motion could drastically alter the hopping integrals and give rise to large Peierls (nonlocal coupling). By contrast the local coupling stems mostly from higher energy (above 100 meV) localized optical modes. This too agrees well with our physical intuition, we expect these intramolecular distortions to have the largest effects on the on-site energy term and give rise to large Holstein (local couplings) as seen in Fig. 4.2.

Next, we note that as one moves from naphthalene to pentacene, the relative proportion of local to nonlocal coupling steadily decreases. Integrating under the spectral functions, we find that in naphthalene, roughly 75% of the total exciton-phonon coupling is local while in pentacene only 20% is local. This trend can also be rationalized. As acene length increases the size of the MLXWF is also expected to increase. With increasing size, we expect the MLXWF to be less sensitive to intermolecular vibrations so that the local coupling strength diminishes. By contrast larger MLXWF allow for more overlap with adjacent MLXWF as molecules move relative to one another. The implication is then that nonlocal coupling should increase with chain length. Taken together, both these observations will tend to decrease the ratio of nonlocal to local coupling, consistent with what is shown in Fig. 4.2.

At face value, Fig. 4.2, suggests that for napthalene, anthracene, and possibly tetracene it may be valid to think about transport within Holstein's small polaron framework. By contrast in pentacene, where Fig. 4.2 suggests that nonlocal coupling dominate, one would expect small polaron theory to be inadequate. In fact, we speculate that the extent of the nonlocal coupling is overestimated in this analysis due to anharmonic effects. When anharmonic effects are included, we expect the low-lying acoustic phonon modes to stiffen and the zero-point amplitude associated with these modes to decrease [117]. Both effects should lower the nonlocal exciton-phonon contribution. By contrast, the local coupling should remain the same after including anharmonicity as the high frequency optical modes are insensitive to anharmonic effects. Going forward, we will focus only on the polaronic picture in the harmonic limit.

4.6 Small Polaron Theory and the Lang-Firsov Transformation

To pass to the exciton-polaron picture, we make a similarity transform of the form $\mathcal{H}^{\mathrm{pol}} = e^{\mathcal{S}}\mathcal{H}^{W}e^{-\mathcal{S}}$ where

$$\mathcal{S} = -\sum_{m\mathbf{R}\mathbf{q}\nu} c^{\dagger}_{m\mathbf{R}}c_{m\mathbf{R}}\frac{e^{-i\mathbf{q}\cdot\mathbf{R}}\mathcal{G}^{W}_{mm\nu}(\mathbf{0},\mathbf{q})}{\omega_{\mathbf{q}\nu}}(b_{\mathbf{q}\nu} - b^{\dagger}_{-\mathbf{q}\nu}). \tag{4.9}$$

In Appendix A.3, we detail the derivation of $\mathcal{H}^{\mathrm{pol}}$. Here we note that $\mathcal{H}^{\mathrm{pol}}$ can be expressed in terms of the exciton-polaron $d^{\dagger}_{m\mathbf{R}}(d_{j\mathbf{R}})$ creation (annihilation) operators, the former is defined as

$$d^{\dagger}_{m\mathbf{R}} \equiv e^{\mathcal{S}}c^{\dagger}_{m\mathbf{R}}e^{-\mathcal{S}} = c^{\dagger}_{m\mathbf{R}}\exp\left[-\sum_{\nu\mathbf{q}}\frac{e^{-i\mathbf{q}\cdot\mathbf{R}}\mathcal{G}^{W}_{mm\nu}(\mathbf{0},\mathbf{q})}{\omega_{\mathbf{q}\nu}}(b_{\mathbf{q}\nu} - b^{\dagger}_{-\mathbf{q}\nu})\right]. \tag{4.10}$$

Physically, $c^{\dagger}_{m\mathbf{R}}$ acts to create a localized excitonic state on the m^{th} molecular site in unit cell $\mathbf{R}$, while the exponential term has the form of a displacement operator acting on the ionic degrees of freedom. Taken together, when acting on the vacuum $d^\dagger_{m\mathbf{R}}$ creates a localized exciton at lattice site $(m\mathbf{R})$ and deforms the ionic lattice about this excitation. This is our physical picture of an exciton-polaron.

In terms of these operators, $\mathcal{H}^{\text{pol}}$ reads

$$\mathcal{H}^{\text{pol}} = -\sum_{m\mathbf{R}} \Delta_{m\mathbf{R}} d^\dagger_{m\mathbf{R}} d_{m\mathbf{R}} + \sum_{\mathbf{q}\nu} \omega_{\nu\mathbf{q}} b^\dagger_{\mathbf{q}\nu} b_{\mathbf{q}\nu} + \sum_{nm\mathbf{R}\mathbf{R}'} V_{mn}(\mathbf{R}-\mathbf{R}') d^\dagger_{m\mathbf{R}} d_{n\mathbf{R}'} + \mathcal{H}^{\text{nonlocal}}, \tag{4.11}$$

where $\Delta_{m\mathbf{R}}$ is the exciton-polaron self-energy and $\mathcal{H}^{\text{nonlocal}}$ denotes a residual term stemming entirely from nonlocal exciton-phonon matrix elements. From here on we will neglect $\mathcal{H}^{\text{nonlocal}}$, based on results from the previous section, we expect this to be a better approximation from smaller acenes.

In zero temperature limit, the exciton-polaron energy $\Omega^{\text{pol}}_{m\mathbf{R}}$ can be read off from the diagonal components of $\mathcal{H}^{\text{pol}}$, explicitly

$$\Omega^{\text{pol}}_{m\mathbf{R}} = -\Delta_{m\mathbf{R}} + V_{m\mathbf{R}m\mathbf{R}}, \tag{4.12}$$

where $V_{m\mathbf{R},m\mathbf{R}}$ is

$$V_{m\mathbf{R},m\mathbf{R}} = \sum_{S\mathbf{Q}} |U_{mS}(\mathbf{Q})|^2 \Omega_{S\mathbf{Q}}, \tag{4.13}$$

which follows directly from Eq. 4.6. Notably $V_{m\mathbf{R},m\mathbf{R}}$ depends only on the exciton dispersion and we refer to this term as the electronic contribution to the exciton-polaron state. By contrast, the exciton-polaron self-energy $\Delta_{m\mathbf{R}}$ is given explicitly as

$$\begin{aligned} \Delta_{m\mathbf{R}} &= \frac{1}{N_{\mathbf{q}}} \sum_{\mathbf{q}\nu} \frac{|\mathcal{G}^W_{mm\nu}(\mathbf{0},\mathbf{q})|^2}{\omega_{\mathbf{q}\nu}} \\ &= \frac{1}{N_{\mathbf{q}}} \sum_{\mathbf{q}\nu} \frac{|\sum_{SS'\mathbf{Q}} U^\dagger_{mS'}(\mathbf{Q}+\mathbf{q}) \mathcal{G}_{S'S\nu}(\mathbf{Q},\mathbf{q}) U_{Sm}(\mathbf{Q})|^2}{\omega_{\mathbf{q}\nu}}. \end{aligned} \tag{4.14}$$

The exciton-polaron self-energy, $\Delta_{m\mathbf{R}}$ is independent of the unit cell, labeled by $\mathbf{R}$, as must be the case for a system with translational symmetry. A direct calculation shows that $-\Delta_{m\mathbf{R}}$ can also be interpreted as the energy release associated with the relaxation of the lattice about about the localized excitation $(m\mathbf{R})$. This term is often also referred to as the reorganization energy [40].

4.7 Exciton Diffusion in the Hopping Regime

As already discussed, in the polaronic picture, the default is for the exciton-polaron to remain localized about a lattice site, only when there is sufficient thermal energy can the exciton-polaron hop from one site to another. The motion is still diffusive and we expect the diffusion constant to be given by

$$D^{\text{hopping}}_{\alpha\beta} = \frac{1}{N_{\mathbf{R}}} \sum_{mn\mathbf{R}} p_{n\mathbf{R}} (\mathbf{x}_{n\mathbf{R}\to m\mathbf{R}'})_\alpha (\mathbf{x}_{n\mathbf{R}\to m\mathbf{R}'})_\beta k_{n\mathbf{R}\to m\mathbf{R}'}, \tag{4.15}$$

where $p_{m\mathbf{R}}$ is the normalized probability to find an exciton-polaron in state in the $(m\mathbf{R})$ at thermal equilibrium, while $\mathbf{x}_{n\mathbf{R}\to m\mathbf{R}'}$ and $k_{n\mathbf{R}\to m\mathbf{R}'}$, respectively denote the distance and hopping rate between exciton-polaron states labeled by $(n\mathbf{R})$ and $(m\mathbf{R}')$ with α and β again labeling Cartesian components. Finally, $N_{\mathbf{R}}$ denotes the number of unit cell used in the simulation.

We have written Eq. 4.15 is such a way that it is easily compared with Eq. 4.2 but have yet to specify how $x_{n\mathbf{R}\to m\mathbf{R}'}$, and $k_{n\mathbf{R}\to m\mathbf{R}'}$ should be computed. We take $x_{n\mathbf{R}\to m\mathbf{R}'}$ to be the distance between Wannier centers of our MLXWF. As already depicted in Sec. 4.4, these centers coincide with the centroid of the molecules in our system so that we can think about the exciton-polaron as hopping between molecules. To determine $k_{n\mathbf{R}\to m\mathbf{R}'}$, we treat the hopping term in Eq. 4.11 perturbatively at the level of Fermi's Golden Rule. The calculation gives

$$k_{n\mathbf{0}\to m\mathbf{R}} = \frac{V^2_{mn}(\mathbf{R})}{\hbar^2} e^{-2S_{mn}(\mathbf{R})} \int_{-\infty}^{\infty} dt \Big[\exp\Big(-\frac{1}{N_{\mathbf{q}}} \sum_{\nu\mathbf{q}} M^2_{mn\nu}(\mathbf{R},\mathbf{q}) \Phi_{\mathbf{q}\nu}(t) \Big) - 1 \Big], \tag{4.16}$$

where

$$\begin{aligned} M^2_{mn\nu}(\mathbf{R},\mathbf{q}) &= \frac{|\mathcal{G}_{mm\nu}(\mathbf{0},\mathbf{q}) e^{i\mathbf{q}\cdot\mathbf{R}} - \mathcal{G}_{nn\nu}(\mathbf{0},\mathbf{q})|^2}{\omega^2_{\mathbf{q}\nu}}, \\ S_{mn}(\mathbf{R}) &= \frac{1}{N_{\mathbf{q}}} \sum_{\nu\mathbf{q}} M^2_{mn\nu}(\mathbf{R},\mathbf{q}) [2n_{\mathbf{q}\nu} + 1], \\ \Phi_{\mathbf{q}\nu}(t) &= n_{\mathbf{q}\nu} e^{i\omega_{\mathbf{q}\nu} t} + (n_{\mathbf{q}\nu}+1) e^{-i\omega_{\mathbf{q}\nu} t}. \end{aligned} \tag{4.17}$$

The subtraction of unity at the end of Eq. 4.16 removes the coherent contribution. In the limit where $k_B T \gg \omega_{\mathbf{q}\nu}$, the integrand oscillates rapidly and it is possible to make a saddle-point approximation to Eq. 4.16. The result is

$$k_{n\mathbf{0}\to m\mathbf{R}} = \frac{|V_{mn}(\mathbf{R})|^2}{\hbar^2} \sqrt{\frac{\pi}{\lambda_{mn}(\mathbf{R}) k_B T}} \exp\Big[-\frac{\lambda_{mn}(\mathbf{R})}{4 k_B T} \Big], \tag{4.18}$$

where

$$\lambda_{mn}(\mathbf{R}) = \frac{1}{N_{\mathbf{q}}} \sum_{\mathbf{q}\nu} M^2_{mn}(\mathbf{R},\mathbf{q}) \omega_{\mathbf{q}\nu}. \tag{4.19}$$

Eq. 4.18, has an Arrhenius form with activation energy $E_a = \lambda_{mn}(\mathbf{R})/4$, to hop from $(n\mathbf{0})$ to $(m\mathbf{R})$. In the limit of a single band with nearest neighbor hopping, Eq. 4.18 reduces to the textbook result [40]. A similar result can also be derived starting from Marcus theory [118].

For the acene crystals we found that the phonons which couple locally to the excitons are typically high energy ($\sim$ 100meV) optical modes (see Fig. 4.2). Thus the replacement of Eq 4.16 with Eq. 4.18 is not strictly valid and it would be better to explicitly perform the time integral in Eq. 4.16. However in this work, as a first approximation, we will use Eq. 4.18 which is ubiquitous in the quantum chemistry literature. In future work we will compare the two expressions and quantify the error made in using the Marcus theory result.

4.8 Phonon-Induced Exciton Renormalization

Before computing hopping and scattering rates, as a first application of our exciton-phonon formalism, we compute the exciton-polaron energy computed with the aid of Eq. 4.12.

	Ω^{BSE} (eV)	Ω^{pol} (eV)	$\Delta\Omega$ (meV)	Ω^{exp} (eV)
Np ($N = 2$)	2.97	2.69	-280	2.6
Ac ($N = 3$)	2.05	1.86	-190	1.9
Tc ($N = 4$)	1.43	1.31	-120	1.3
Pc ($N = 5$)	0.96	0.90	-60	0.9

Table 4.1: Bare, Ω, phonon dressed, Ω^{pol}, and experimental, Ω^{exp}, energies for the lowest lying spin-triplet. Experimental values taken from [73] and references therein.

In Tab. 4.1, we report lowest spin-triplet exciton energies for napthalene (Np), anthracene (Ac), tetracene (Tc), and pentacene (Pc) computed though solving the *ab-initio* BSE with ions clamped at equilibrium positions, Ω^{BSE}, and after coupling to phonons has been included by evaluating Eq. 4.12. Including polaronic effects tends to decrease Ω^{pol} relative to Ω^{BSE} and, over all compounds, brings theory into better agreement with experiment. In the third column we report the exciton-polaron formation energy defined as $\Delta\Omega = \Omega^{\text{BSE}} - \Omega^{\text{pol}}$. We observe that the formation energy steadily decreases as the number of acene rings, N, increases. The trend stems from two factors: as N increases, $V_{m\mathbf{R},m\mathbf{R}}$, the energy cost associated with exciton localization increases, while $\Delta_{m\mathbf{R}}$, the energy gain associated with lattice relaxation decreases. Both trends tend to decrease $\Delta\Omega$ with increasing N.

4.9 Relaxation Times and Hopping Rates

While Tab. 4.1 validates our approach, with this information alone, it is difficult to ascertain whether the exciton or exciton-polaron quasiparticle basis is more appropriate for studying transport in these systems. Notably a negative exciton-polaron formation energy does not guarantee the formation of an exciton-polaron as coupling to phonons in any formalism will nearly always tend to decrease the excitation energy. To determine which basis is more appropriate for studying dynamics, in Tab. 4.2, we report the phonon-limited exciton, τ_{xct}, and exciton-polaron, $\tau_{\text{xct-pol}}$, relaxation times. The former is defined the as the average time an exciton remains in its lowest energy quantum state while the latter is the average time an exciton-polaron remains in its lowest energy quantum state . By definition, the former is equal to the relaxation time (see Eq. 4.3) while the latter is related to the exciton-polaron hopping rate through

$$\tau_{\text{xct-pol}} = \frac{1}{\sum_{m\mathbf{R}'} k_{1\mathbf{0}\to m\mathbf{R}'}}, \tag{4.20}$$

i.e. summing over all possible hopping events given the exciton polaron is initially at site $n = 1$ in the home cell ($\mathbf{R} = \mathbf{0}$). As expected, $\tau_{\text{xct-pol}}$ increases with increasing chain length, N, a direct by-product of an increase in hopping, V, and decrease in activation energy, E_a, with N. Somewhat surprisingly we find that τ_{xct} is roughly independent of acene chain length. This constant exciton coherence time stems from an off-set of two effects – as N increases the phase space for phonon scattering increases while the exciton-phonon coupling strength simultaneously decreases. In the final column, we report the ratio of $\tau_{\text{xct}}/\tau_{\text{xct-pol}}$ finding this quantity is strictly less than unity across all acenes, physically indicating that the exciton-polaron is a more stable (longer lived) triplet quasiparticle state.

	$\tau_{\text{xct-pol}}$	τ_{xct}	$\tau_{\text{ xct}}/\tau_{\text{ xct-pol}}$
Np ($N = 2$)	26.1 ps	30 fs	0.001
Ac ($N = 3$)	3.8 ps	30 fs	0.008
Tc ($N = 4$)	230 fs	20 fs	0.086
Pc ($N = 5$)	90 fs	30 fs	0.333

Table 4.2: Exciton, τ_{xct} and exciton-polaron, $\tau_{\text{xct-pol}}$ relaxation times.

Our analysis of the coherence times suggest that across all acenes, triplet diffusion is better described with thermally activated hopping, instead of phonon-limited band-like diffusion models. Nevertheless, for larger acenes like Tc and Pc, τ_{xct} and $\tau_{\text{xct-pol}}$ are similar enough in magnitude that computing the diffusion coefficients in both limits is a worthwhile endeavour. For this calculation, we require relaxation times throughout the BZ, $\tau_{S\mathbf{Q}}$, and site resolved hopping rates, $k_{n\mathbf{0}\to m\mathbf{R}}$.

In the first row of Fig. 4.3, we plot the exciton dispersion for the two lowest triplet excitons overlaying relaxation times computed via Eq. 4.3 at $T = 300$K. Relaxation times are relatively uniform throughout the Brillouin zone (BZ) in Np and Ac ranging from 25-50 fs. By contrast in Tc and Pc, there is slightly greater anisotropy in relaxation times. We further observe that in Tc relaxation times are largest at the X and Y BZ corners while in Pc the longest relaxation time occurs at Γ. In Pc there are narrowly avoided crossings at X and Y, too small to see in Fig. 4.3, while in Tc, the crossings at X and Y are real. Such behavior suggests that the character of the Tc and Pc bands should be very different and it is likely that different trends in the relaxation times throughout the BZ stem from this feature in the dispersion.

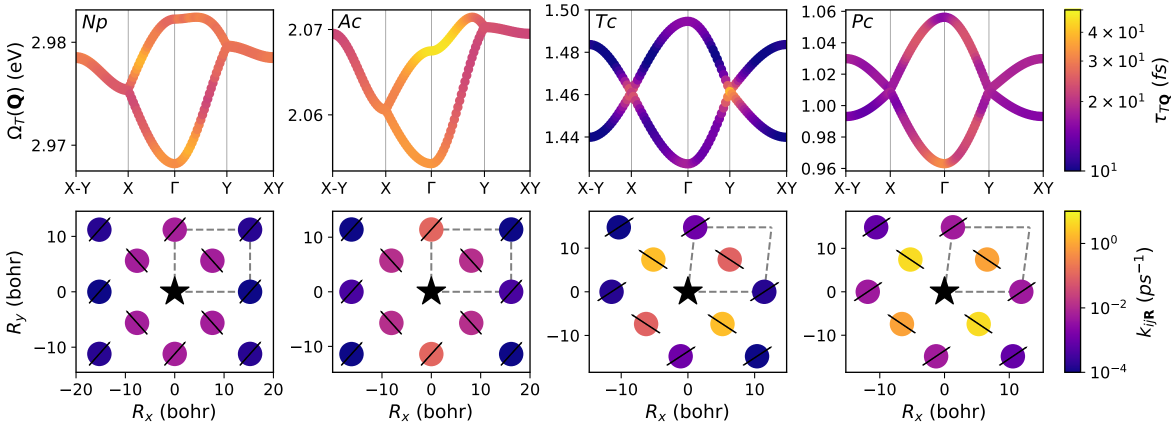

Figure 4.3: In the first row we depict the triplet exciton dispersion, computed through solving the BSE, for the lowest two states in naphthalene (Np), anthracene (Ac), tetracene (Tc), and pentacene (Pc) with state-dependent relaxation times, $\tau_{T\mathbf{Q}}$ computed via Eq. 4.3 and overlaid in color. In the second row we depict the hopping rates $k_{ij\mathbf{R}}$ computed in the exciton-polaron picture. The star at the center of each figure denotes the initial exciton-polaron state. Hash marks denote nearby molecular sites which excitons can hop to. The colored dots which overlay the hash marks correlate with the rate at which the exciton-polaron hops to nearby states. For instance in the final plot, the red arrow depicts a nearest neighbor hopping event while the bright yellow color dot signifies average rate for this hopping is 6 ps^{-1} – put another way, the exciton, on average makes this type of hop 6 times every picosecond. The gray dashed squares denote the unit cell and all calculations are performed at $T = 300$K

In the second row of Fig. 4.3, we provide a real-space depiction of the exciton hopping rates. The star in the center of these plots indicates the center-of-mass of the initial exciton-polaron state, while the surrounding hash marks denote nearby molecular sites the exciton-polaron can hop to. The colored dots depict the rate at which hopping occurs to that site computed with Eq. 4.16. In general, the hopping rates decrease as one considers sites further from the initial exciton-polaron state, however the details vary across the acenes. For instance in Np and Ac, the rate of hopping to the nearest four sites is identical due to a nonsymmorphic symmetry these two acenes possess. This symmetry is also responsible for the degeneracy seen in the exciton dispersion in row 1 for Np and Ac along the first and final segments of the band plots. By contrast, Tc and Pc do not possess this symmetry, as a result the four fold degeneracy in the hopping rate to nearest neighbor sites splits and we find slight preference to hop along a specific direction.

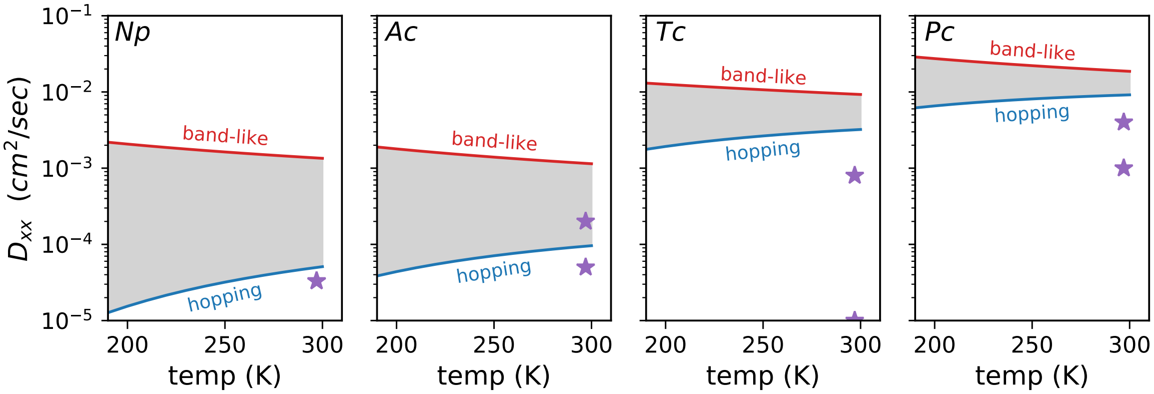

Figure 4.4: The ab-plane averaged exciton diffusion coefficient $\langle D\rangle_{ab}$ as a function of temperature for Np, Ac, Tc, and Pc, with the red and blue curves denoting the diffusion coefficient computed via Eqs. 4.2 and 4.15 respectively. The two curves give rough upper and lower theoretical bounds on exciton diffusion coefficients and we shade the intermediate region gray. Purple stars denote experimentally reported diffusion coefficients compiled in Ref. [96].

4.10 Diffusion Coefficients From Band and Hopping Theories

With these ingredients, we are in a position to compute the diffusion coefficients, $D_{\alpha\beta}$, in the band and hopping limits via Eqs. 4.2 and 4.15 respectively. In Fig. 4.4, we show the results of these calculations plotting the diffusion coefficient averaged over the ab plane, $\langle D\rangle_{ab}$, over a 100K temperature range, plotting the band-like and hopping limits in red in and blue respectively. There are several universal, and expected, trends seen across all crystals. In all cases, we find that $\langle D^{\text{ band}}\rangle_{ab} > \langle D^{\text{ hopping}}\rangle_{ab}$ implying that in this temperature range, the coherent band-like transport is more efficient than thermally activated hopping-like transport. Further the two curves display opposite temperature dependences, as expected. With increasing temperature the band-like diffusion coefficients decrease, reflecting the fact that band-like diffusion is phonon-limited. By contrast the hopping diffusion coefficient increases with temperature reflecting the fact that incoherent hopping-like diffusion is phonon mediated.

In Np and Ac the diffusion coefficients in the band and hopping limits are separated by roughly two orders of magnitude at $T = 300$K. By contrast in Tc and Pc the band and hopping predictions are much closer in magnitude differing by only a factor of two or so at $T = 300$K. That the band and hopping expressions give similar results for these larger acenes, parallels nicely the coherence times reported in Tab. 4.2 where we found that exciton and exciton-polaron coherence times were relatively close.

In Fig. 4.4, we have also plotted experimentally reported diffusion coefficients (purple stars) taken from the review article [96]. In Np and Ac, we find very good agreement between experiment and the theoretically determined $\langle D^{\text{ hopping}}\rangle_{ab}$ computed at room temperature while $\langle D^{\text{ band}}\rangle_{ab}$ significantly and systematically overestimates experiment. The result is particularly satisfying given that prior analysis suggests that for these materials the hopping regime is the more appropriate of the two limits to consider. In Tc and Pc, we find that both our theoretical band-like and hopping predictions overestimate experimentally reported values by a factor of roughly 2-10, with the hopping diffusion coefficients fairing somewhat better. There are a plethora of possible explanations as to why this might be the case. First, the larger acenes host a number of multi-exciton processes such as triplet-triplet annihilation [119]. These processes provide other avenues for exciton decay and have not been included in the present analysis. Their inclusion would undoubtedly act to decrease the theoretically computed exciton diffusion coefficient and could partially explain discrepancies with experiment and theory. Second, in this study we have neglected to include the effects of thermal lattice expansion opting instead to use experimental lattice parameters often taken from diffraction measurements below room temperature. Thermal expansion will tend to increase the spacing between molecules in turn decreasing the exciton overlap integrals, band-velocities, and through these quantities both the hopping and band-like diffusion coefficients. Finally we note that accurate experimental determination of triplet diffusion coefficients is quite complicated, often involving deconvolution of the spin-triplet and singlet excitations and subsequent fitting to intricate kinetic models. As a result a range of experimental diffusion coefficients have been reported in the literature further hindering comparison between experiment and theory.

This concludes our discussion of computational results. In the subsequent two sections, we discuss extensions and future directions related to this work before giving our conclusion in Sec. 4.13

4.11 Variational Determination of U

In this work, we choose to work in a basis of MLXWFs. By definition, this basis is an upper bound on the extent to which the lattice can localize the exciton. For systems clearly in the polaronic regime, we expect the use of this basis to be a decent approximation. However for systems like pentacene, where exciton transport is intermediate between hopping and band-like it may be possible to find a better basis for our calculation.

One option is to treat the Wannier rotation matrices, $U_{Sj}(\mathbf{Q})$ appearing in Eq. 4.4 as variational parameters. In this approach we can view the polaronic operators, $d^{\dagger}_{m\mathbf{R}}[U]$ as a functional of U. Explicitly

$$\begin{aligned} d^{\dagger}_{m\mathbf{R}}[U] = &\left(\sum_{S\mathbf{Q}} e^{-i\mathbf{Q}\cdot\mathbf{R}} U_{Sm}(\mathbf{Q}) c^{\dagger}_{S\mathbf{Q}}\right) \\ &\times \exp\left[-\sum_{\nu\mathbf{q}} \frac{\sum_{SS'\mathbf{Q}} U^{\dagger}_{mS'}(\mathbf{Q}+\mathbf{q})\mathcal{G}_{S'S\nu}(\mathbf{Q},\mathbf{q})U_{Sm}(\mathbf{Q})}{\omega_{\mathbf{q}\nu}}(b_{\mathbf{q}\nu} - b^{\dagger}_{-\mathbf{q}\nu})\right]. \end{aligned} \tag{4.21}$$

To fix U, we minimize the polaron energy, at $T = 0$, we find

$$\begin{aligned}\Omega^{\text{pol}}_{m\mathbf{R}}[U] &= \langle 0|d_{m\mathbf{R}}[U]\mathcal{H}d^{\dagger}_{m\mathbf{R}}[U]|0\rangle \\ &= V_{m\mathbf{R},m\mathbf{R}}[U] - \Delta_{m\mathbf{R}}[U]\end{aligned} \tag{4.22}$$

where $V_{m\mathbf{R},m\mathbf{R}}[U]$ and $\Delta_{m\mathbf{R}}[U]$ are defined explicitly in Eqs. 4.13 and 4.14 respectively. In the dilute limit, where the probability of finding two exciton-polarons in the same unit-cell is unlikely, the m^{th} row of U may be determined by minimizing the m^{th} exciton-polaron excitation energy $\Omega^{\text{pol}}_{m\mathbf{0}}[U]$ subject to the constraint U is unitary, ensuring orthogonality of the exciton-polaron states.

This approach of determining U is similar in spirit to the seminal work of Lee, Low, and Pines on polarons in the intermediate coupling regime [120] and later by Pollmann and Büttner to describe an exciton interacting with a polar lattice [18]. In their approach they embed the variational parameter in U in the generator of the canonical transform $\mathcal{S}'[U]$ and then fix U by minimizing the expectation value, $\langle 0|e^{-\mathcal{S}'[U]}\mathcal{H}e^{\mathcal{S}'[U]}|0\rangle$ with respect to U. While the framework is the same, we emphasize the in both the Lee, Low, and Pines and Pollmann and Büttner framework the generator of the canonical transform they use, $\mathcal{S}'[U]$, differs fundamentally from the one used in this work $\mathcal{S}[U]$ which is why we have distingushed them with a prime.

To the best of our knowledge, determining U though *ab-initio* minimization of $\Omega^{\text{pol}}[U]$ has yet to be fully explored. Only very recently, has Sio et. al., carried out an analogous minimization in the context of describing the lowest energy electron-polaron and hole-polaron state in a few representative semiconducting materials [121, 122]. Indeed, minimizing the lowest energy excitation $\Omega_1^{\text{pol}}[U]$, with respect to the first row of U it is possible to recover expressions originally derived by Sio et. al.

In future work, it will be very interesting to minimize Eq. 4.22 explicitly and compare the ensuing results to those determined with the MLXWF ansatz.

4.12 Extension to Spin-singlet Excitons and the Connection to Dexter and Förster Coupling

In this work we have restricted our analysis to spin-triplet excitons only. The extension to the spin-singlet case is nontrivial but highlights the connection between Dexter and Förster coupling in quantum chemistry and is interesting to discuss here.

As discussed in Chap. 2, for spin singlets, the exchange term of the BSE electron-hole kernel gives rise to long range dipole-dipole interaction. With this interaction, in the Wannier basis, Eq. 4.5 reads

$$\mathcal{H}^{\mathrm{W,singlet}} = \sum_{m\mathbf{R}n\mathbf{R}'} \left[V_{mn}(\mathbf{R}-\mathbf{R}') + \frac{\mathbf{p}_m \cdot \mathbf{p}_n}{d^3} - 3\frac{(\mathbf{p}_m \cdot \mathbf{d})(\mathbf{p}_n \cdot \mathbf{d})}{d^5} \right] c^{\dagger}_{m\mathbf{R}} c_{n\mathbf{R}'} + \sum_{\mathbf{q}\lambda} \omega_{\mathbf{q}\nu} b^{\dagger}_{\mathbf{q}\nu} b_{\mathbf{q}\nu}$$
$$+ \sum_{mn\mathbf{R}\mathbf{R}'\mathbf{q}\nu} e^{-i\mathbf{q}\cdot\mathbf{R}} \mathcal{G}^{\mathrm{W}}_{mn\nu}(\mathbf{R}-\mathbf{R}', \mathbf{q}) c^{\dagger}_{m\mathbf{R}} c_{n\mathbf{R}'} (b^{\dagger}_{-\mathbf{q}\nu} + b_{\mathbf{q}\nu}) \tag{4.23}$$

where $\mathbf{p}_m$ are the dipole moments associated with Wannier orbital $W_{m\mathbf{0}}$ in the average electron-hole coordinate as defined in Chap. 1, and $\mathbf{d}$ is the distance between Wannier centers, explicitly $\mathbf{d} = \mathbf{R} + \boldsymbol{\tau}_m - (\mathbf{R}' + \boldsymbol{\tau}_n)$. Carrying through the same manipulations that led to the Marcus theory-like expression for the hopping rate given in Eq. 4.18, we find

$$k_{n\mathbf{0}\to m\mathbf{R}} = \frac{1}{\hbar^2} \left| V_{mn}(\mathbf{R}) + \frac{\mathbf{p}_m \cdot \mathbf{p}_n}{d^3} - 3\frac{(\mathbf{p}_m \cdot \mathbf{d})(\mathbf{p}_n \cdot \mathbf{d})}{d^5} \right|^2 \sqrt{\frac{\pi}{\lambda_{mn}(\mathbf{R}) k_B T}} \exp\left[-\frac{\lambda_{mn}(\mathbf{R})}{4 k_B T} \right]. \tag{4.24}$$

Eq. 4.24 is essentially equivalent to 4.18 except for the appearance of a dipole-dipole term in the leading matrix element of the expression. When squared, this dipole-dipole interaction falls off as $1/d^6$. By contrast, the $V_{mn}(\mathbf{R})$ is a measure of the overlap between nearby MLXWFs and falls off at exponentially in d. In quantum chemistry the dipole-dipole term is often referred to as a Fërester interaction [123] while the short range term proportional to the overlap $V_{mn}(\mathbf{R})$ is the Dexter interaction [124].

Presently the extension of this theory to the singlet case is hindered only by the accurate determination of the Wannier exciton dipole moments as discussed in Chap 2 where we found that the exchange kernel mixes many states and the determination effective low-lying Wannier exciton dipole moments is a non-trivial task.

4.13 Conclusion

In this work, we have developed an *ab-initio* framework for studying exciton diffusion based on linear exciton-phonon coupling that treats the band-like and hopping limits on equal footing for crystalline solids. In the hopping limit, we have generalized the original Lang-Firsov polaron transformation to the multi-band case explicitly considering the gauge freedom this introduces. Using a physically motivated choice of gauge in the hopping limit, we apply our framework to the acene series. We find significant renormalization of triplet exciton energies due to the lattice. Analysis of the exciton and exciton-polaron coherence times suggest that for shorter acenes (Np and Ac) the exciton-polaron basis is a better starting point for studying triplet exciton transport while for longer acenes (Tc and Pc) it is somewhat ambiguous. We compute the diffusion coefficient as a function of temperature for all materials finding excellent agreement between theory and experiment for Np and Ac. In Tc and Pc we find the agreement with theory and experiment is less good, possibly due to the neglect of multi-exciton processes which have not been considered in this work. We expect that the formalism developed here can be used as a starting point for an even more general predictive description of exciton transport going beyond these two limits without resorting to empirical parameters.

Chapter 5

Phonon Screening of Excitons in Semiconductors: Halide Perovskites and Beyond

This chapter is adapted from Ref. [125] and includes work in collaboration with Marina R. Filip.

5.1 Introduction

Excitons are central to a wide range of optoelectronic applications, from photovoltaics and photocatalysis, to light emission and lasing [98, 126–128]; they emerge from the many-body interactions between charge carriers, photons, and phonons in optoelectronic materials [2]. In many bulk semiconductors, weakly bound Wannier-Mott excitons can be understood with a hydrogenic model [5, 129], in which the attractive Coulomb interaction between a photoexcited electron-hole pair is screened by a dielectric constant ε. In this picture, the exciton binding energy is $\mu/2\varepsilon^2$ in atomic units, where μ is the magnitude of the reduced effective mass of the electron-hole pair [5]. Optical measurements under high magnetic fields use this model to extract the exciton binding energy, E_B and μ [130, 131]. In ionic or multicomponent semiconductors, an "effective dielectric constant", $\varepsilon_{\text{eff}} = \sqrt{2E_B/\mu}$, is frequently reported, usually taking values between the optical, ε_∞, and static, ε_0, dielectric constants. The use of ε_{eff} approximately accounts for the fact that the electron-hole interaction is screened by both the electrons and phonons [17, 127, 132]. However, it also obscures the details of specific phonons contributing to ε_{eff}, and it does not explain whether or why electron or phonon screening might be important in a given case. Rigorous *ab initio* calculations would therefore be of great value in this context.

Ab initio many-body perturbation theory calculations within the GW approximation [11, 43] and the Bethe-Salpeter equation (BSE) [12, 133] approach have been successful in quantitatively understanding the quasiparticle band structure and optical excitations of materials ranging from the simplest III-V semiconductors [12] to materials with heavy elements [134] or hybrid organic-inorganic components [135], low dimensionality [136], and intrinsic defects [137]. First principles methods including the effects of lattice vibrations have led to new understanding of the renormalization of the electronic band structure due to electron-phonon interactions [38, 138, 139], as well as optical absorption [140, 141] and photoluminescence lineshapes [19, 142].

Recently, several first principles studies of a broad range of materials predicted exciton binding energies which are overestimated with respect to experiment [143–147]. In particular, Ref. [146] recently reported calculated exciton binding energies of hybrid organic-inorganic lead-halide perovskites which overestimate experimental measurements by up to a factor of 3. Ref. [146] attributed this overestimation to the coupling of the constituent free electrons and holes to phonons (hereafter referred to as "polaronic effects"). On the other hand, Ref. [147] used an approximate model dielectric function to conclude that phonon screening due to infrared active phonons renormalizes the exciton binding energy by up to 50%, bringing calculated values in much closer agreement with experiment. Since both reports are based on approximate hypotheses and implementations of phonon effects, it is not yet clear how these conclusions may be reconciled, in the absence of a complete *ab initio* calculation.

The problem of electrons and holes interacting in a phonon field has been studied using phenomenological models, assuming parabolic electronic band structure and a phonon spectrum consisting of a single dispersionless phonon [17, 132, 148–150]. Ref [132] showed that calculation of the exciton binding energy within such models must account for polaronic and phonon screening effects, with both contributions leading to a net decrease of the calculated exciton binding energy, as compared with the standard hydrogenic model expression [132]. However, rigorous inclusion of polaronic and phonon screening effects within the BSE formalism remains an open challenge. In this work, we focus on the latter.

The remainder of this chapter is organized as follows. In Sec. 5.2 we review the screened phonon formalism and give a diagrammatic description of this screening. In Sec. 5.3 we show the Bethe-Salpeter Equation approach can be rigorously generalized to include phonon screening. In Sec. 5.4 we give results of $\mathrm{CsPbX_3}$ family of perovskites. In Sec. 5.5 we review how Haken's phenomenological potential can be recovered in the present approach and use this result to give a simple expression for the renormalization of the exciton binding energies in terms of physical macroscopic quantities. In Sec. 5.6 we discuss effects beyond the virtual exchange of a phonon focusing especially on polaron interference effects. In Sec. 5.8 and 5.9 we discuss future directions focusing on the imaginary part of the phonon correction as well as the screening of excitons due to other low energy bosonic excitations, using the carrier plasmon is a specific example of recent work in this space.

5.2 Electronic and Ionic Contributions to the Screened Electron-Electron Interaction

Central to the framework presented here is the equivalent treatment of electronic and ionic contributions to the screened Coulomb interaction, W. As discussed by Hedin and Lundquist [22], and reviewing in Chap. 2, W can rigorously be written as the sum of an electronic, W^{el}, and ionic (or phonon), W^{ph} part, explicitly in the frequency domain,

$$W(\mathbf{r}, \mathbf{r}'; \omega) = W^{\text{el}}(\mathbf{r}, \mathbf{r}'; \omega) + W^{\text{ph}}(\mathbf{r}, \mathbf{r}'; \omega). \tag{5.1}$$

where the separation highlights the fact that both the electronic and ionic degrees of freedom independently screen the bare electron-electron interaction.

The electronic contribution to the screened interaction is often expressed in frequency space as

$$W^{\text{el}}(\mathbf{r}, \mathbf{r}', \omega) = \varepsilon^{-1}(\mathbf{r}, \mathbf{r}', \omega) v_c(\mathbf{r} - \mathbf{r}'). \tag{5.2}$$

where $\varepsilon(\mathbf{r}, \mathbf{r}', \omega)$ and $v_c(\mathbf{r} - \mathbf{r}')$ denote the frequency dependent (optical) dielectric function and bare Coulomb interaction, respectively. This form is particularly convenient for numerical calculations where $\varepsilon(\mathbf{r}, \mathbf{r}', \omega)$ is frequently computed within the random-phase approximation (RPA). By contrast the general form of W^{ph} is less familiar. In Ref [22] it is given as

$$W^{\text{ph}}(\mathbf{r}, \mathbf{r}'; \omega) = \frac{1}{N_{\mathbf{q}}} \sum_{\mathbf{q}\nu} g_{\mathbf{q}\nu}(\mathbf{r}) D_{\mathbf{q}\nu}(\omega) g^{\star}_{\mathbf{q}\nu}(\mathbf{r}'), \tag{5.3}$$

where the phonon propagator, $D_{\mathbf{q}\nu}(\omega)$, and electron-phonon matrix elements, $g_{\mathbf{q}\nu}(\mathbf{r})$, are given by

$$D_{\mathbf{q}\nu}(\omega) = \frac{1}{\omega - \omega_{\mathbf{q}\nu} + i\eta} - \frac{1}{\omega + \omega_{\mathbf{q}\nu} + i\eta}, \tag{5.4}$$

and

$$g_{\mathbf{q}\nu}(\mathbf{r}) = \int d^3\mathbf{r}' \varepsilon^{-1}(\mathbf{r}, \mathbf{r}') g^{b}_{\mathbf{q}\nu}(\mathbf{r}'), \tag{5.5}$$

respectively. Here $\omega_{\mathbf{q}\nu}$ are the phonon frequencies associated with phonon with crystal momentum $\mathbf{q}$ in branch ν while η is an infinitesimal positive number which ensures correct time-ordering. In Eq. 5.5, we have expressed the screened electron-phonon interaction in terms of the bare electron-phonon interaction, $g^b(\mathbf{r}) = \partial_{\mathbf{q}\nu} V_{\text{ion}}(\mathbf{r})$, with $\partial_{\mathbf{q}\nu} V_{\text{ion}}(\mathbf{r})$ symbolically denoting the change in the ionic part of the potential upon displacing ions along phonon mode $(\mathbf{q}\nu)$.

To build intuition for these expressions it is helpful to write the W^{el} and W^{ph} as a series in the electronic polarizability, P_e. Recall the relation between ε^{-1} and P_e, namely,

$$\begin{aligned} \varepsilon^{-1} &= \frac{1}{1 - v_c P_e} \\ &= 1 + v_c P_e + v_c P_e v_c P_e + \cdots , \end{aligned} \tag{5.6}$$

where space and time indices have been suppressed and it is understood that the notation $v_c P_e$ implies $\int d^3\mathbf{r}' v_c(\mathbf{r},\mathbf{r}') P_e(\mathbf{r}',\mathbf{r}'',\omega)$. Substituting this expansion in Eq. 5.2 for W^{el}, we find

$$\begin{aligned} W^{\mathrm{el}} &= \varepsilon^{-1} v_c \\ &= (v_c + v_c P_e v_c + v_c P_e v_c P_e v_c + \cdots). \end{aligned} \tag{5.7}$$

At lowest order in perturbation theory $P_e(\mathbf{r}t,\mathbf{r}'t') = iG(\mathbf{r}t,\mathbf{r}'t')G(\mathbf{r}'t',\mathbf{r}t)$ where $G(\mathbf{r}t,\mathbf{r}t')$ is the single particle Greens function. At this order, we physically associate P_e with the creation of a virtual electron hole-pair. Eq. 5.7 can then be interpreted as screening of the Coulomb interaction by virtual electron-hole pairs with each subsequent term accounting for an additional screening event.

We can develop similar microscopic intuition for the W^{ph} by expressing it directly as a function of the irreducible polarizability, P_e. Plugging Eq. 5.6 into 5.5 we find

$$\begin{aligned} g &= \varepsilon^{-1} g^{b} \\ &= g_b + v_c \chi_0 g_b + v_c \chi_0 v_c \chi_0 g_b + \cdots . \end{aligned} \tag{5.8}$$

Then, plugging Eq. 5.8 into the definition of W^{ph} given in Eq. 5.3 and explicitly retaining all terms up to 2$^{\mathrm{nd}}$ order in v_c, we arrive at the following expression

$$\begin{aligned} W^{\mathrm{ph}} &= g D g^{\star} \\ &= (g_b + v_c P_e g_b + v_c P_e v_c P_e g_b + \cdots) D (g_b^{\star} + v_c P_e g_b^{\star} + v_c P_e v_c P_e g_b^{\star} + \cdots) \\ &= g_b D g_b + \\ &\quad v_c P_e g_b D g_b^{\star} + g_b D g_b^{\star} P_e v_c + \\ &\quad v_c P_e v_c P_e g_b D g_b^{\star} + g_b D g_b^{\star} P_e v_c P_e v_c + \\ &\quad \cdots . \end{aligned} \tag{5.9}$$

We find that W^{ph} has nearly the same from as W^{el} but with a phonon propagator $g_b D g_b^{\star}$ inserted at every possible position. It is worth pausing to note the obvious asymmetry. We observe that for a general term in this expansion, the Coulomb interaction can "fire" many times – i.e. a virtual photon can be exchanged many times – however a phonon is never exchanged more than once per term. Physically we expect this to be a reasonable first approximation since the Coulomb interaction is mediated on a much shorter time scale than the those associated with ionic motion.

To build additional insight, and connect with familiar textbook expressions, we explicitly derive an expression for W^{ph} assuming the screening is mediated by a single dispersionless longitudinal optical phonon mode with frequency ω_{LO} which couples to electrons through a Fröhlich vertex with the form

$$g_{\mathbf{q}}(\mathbf{r}) = \frac{i}{|\mathbf{q}|}\left[\frac{4\pi}{NV}\frac{\omega_{\mathrm{LO}}}{2}\left(\frac{1}{\varepsilon_\infty} - \frac{1}{\varepsilon_0}\right)\right]^{\frac{1}{2}} e^{i\mathbf{q}\cdot\mathbf{r}}. \tag{5.10}$$

Plugging Eq. 5.10 and 5.4 into Eq. 5.3, we find

$$W^{\mathrm{ph}}(\mathbf{r},\mathbf{r}';\omega) = \left[\left(\frac{1}{\varepsilon_\infty} - \frac{1}{\varepsilon_0}\right)\frac{\omega_{\mathrm{LO}}^2}{\omega^2 - \omega_{\mathrm{LO}}^2 + i\eta}\right] v_c(\mathbf{r}-\mathbf{r}'). \tag{5.11}$$

We immediately recognize the term in square brackets as the dynamical lattice contribution to the dielectric function derived in elementary treatments of the subject from the motion of a harmonic oscillator. For $\omega \gg \omega_{\mathrm{LO}}$, $W^{\mathrm{ph}} \to 0$ reflecting the fact that at high frequencies the ions can not adjust quickly enough to screen the excitation. While in the $\omega = 0$ limit, $W^{\mathrm{ph}}(\omega = 0) = (\varepsilon_0^{-1} - \varepsilon_\infty^{-1})v_c$. When this $W^{\mathrm{ph}}(\omega = 0)$ is added to $W^{\mathrm{el}}(\omega = 0)$, one finds $W(\omega = 0) = \varepsilon_0^{-1} v_c$ as expected.

In the following sections we detail how to rigorously include both W^{el} and W^{ph} in the GW-BSE approach.

5.3 The GW^{ph} correction

As discussed in Chap. 2, when Hedin's equations are extended to include ionic motion, the first order self-energy correction takes the from $\Sigma = iGW$ where W is given by Eq. 5.1. The electronic contribution to the screened interaction gives rise to the usual GW approximation (here GW^{el}), while the phonon contribution gives rise to the Fan-Migdal self-energy correction. Explicitly

$$\begin{aligned}\Sigma^{\mathrm{ph}}_{nn'}(\mathbf{k},\omega) &= \frac{i}{2\pi}\int G(\mathbf{r},\mathbf{r}';\omega+\omega')W^{\mathrm{ph}}(\mathbf{r},\mathbf{r}';\omega')e^{i\eta\omega'}d\omega \\ &= \sum_{m\mathbf{q}\nu} \langle n\mathbf{k}|g^{\star}_{\nu\mathbf{q}}(\mathbf{r})|m\mathbf{k}+\mathbf{q}\rangle\,\langle m\mathbf{k}+\mathbf{q}|g_{\nu\mathbf{q}}(\mathbf{r}')|n'\mathbf{k}\rangle \\ &\quad\times\left[\frac{f_{m\mathbf{k}+\mathbf{q}}}{\omega - E_{m\mathbf{k}+\mathbf{q}} + \omega_{\nu\mathbf{q}} - i\eta} + \frac{1-f_{m\mathbf{k}+\mathbf{q}}}{\omega - E_{m\mathbf{k}+\mathbf{q}} - \omega_{\nu\mathbf{q}} + i\eta}\right]\end{aligned} \tag{5.12}$$

where the electron-phonon self-energy $\Sigma^{\mathrm{ph}}_{nn';\mathbf{k}}(\omega) = \langle n\mathbf{k}|\Sigma^{\mathrm{ph}}(\mathbf{r},\mathbf{r}';\omega)|n'\mathbf{k}\rangle$ while $E_{n\mathbf{k}}$, $|n\mathbf{k}\rangle$, and $f_{n\mathbf{k}}$, denote the eigenenergy, Bloch eigenstate, and Fermi-Dirac occupation factor (at $T = 0K$) for an electron with band index n and crystal momentum $\mathbf{k}$.

The diagonal component of the electron-phonon self-energy is routinely computed in standard electronic software packages [151]. Physically, the real part of this self-energy gives rise to the renormalization of the electronic eigenvalues due to electron-phonon interactions. This self-energy correction reduces to the Fröhlich's large polaron analysis in the limit where (i) the general electron-phonon matrix element is replaced with the Fröhlich vertex (see Eq. 5.10), (ii) the phonon frequency is replaced with a single dispersionless mode, ω_{LO}, and (iii) isotropic, parabolic bands with effective mass, m are assumed, explicitly $E_{\mathbf{k}} = \mathbf{k}^2/2m$.

With these approximations,

$$\begin{aligned}\mathrm{Re}[\Sigma^{\mathrm{ph}}(\mathbf{k},E_{\mathbf{k}})] &= \frac{-\alpha\omega_{\mathrm{LO}}^{3/2}}{\sqrt{E_{\mathbf{k}}}}\sin^{-1}\left(\frac{E_{\mathbf{k}}}{\omega_{\mathrm{LO}}}\right)^{1/2} \\ &= -\alpha\omega_{\mathrm{LO}} + E_{\mathbf{k}}\left(1-\frac{\alpha}{6}\right) + \cdots ,\end{aligned} \tag{5.13}$$

where, atomic units continue to be used throughout and $\alpha = \sqrt{m/(2\omega_{\mathrm{LO}})}(\varepsilon_{\infty}^{-1} - \varepsilon_{0}^{-1})$. In the second line we have expanded in arcsine to second order in $\sqrt{E_{\mathbf{k}}/\omega_{\mathrm{LO}}}$. We arrive at the usual result; the interaction with the polar phonon lowers the electron energy by amount and $-\alpha\omega_{\mathrm{LO}}$ and increase the effective mass to $m^{\star} = m/(1-\alpha/6)$. The latter will be important in Sec. 5.10 when we discuss polaronic effects on the renormalization of the exciton binding energy.

The imaginary part of Σ^{ph} also contains physical information, namely it is proportional to the phonon-limited relaxation time, i.e. the time between electron-phonon scattering events. Explicitly for the diagonal component we find

$$\begin{aligned}\mathrm{Im}[\Sigma^{\mathrm{ph}}_{nn}(\mathbf{k},E_{n\mathbf{k}})] = \pi\frac{\pi}{N_{\mathbf{q}}}\sum_{m\nu\mathbf{q}}|g_{nm\nu}(\mathbf{k},\mathbf{q})|^2 \\ \times\left[(1-f_{m\mathbf{k}+\mathbf{q}})\delta(E_{n\mathbf{k}}-E_{m\mathbf{k}+\mathbf{q}}-\omega_{\mathbf{q}\nu}) + f_{m\mathbf{k}+\mathbf{q}}\delta(E_{n\mathbf{k}}-E_{m\mathbf{k}+\mathbf{q}}+\omega_{\mathbf{q}\nu})\right].\end{aligned} \tag{5.14}$$

Making the same approximations as above it is possible to derive a model expression for this quantity,

$$\mathrm{Im}[\Sigma^{\mathrm{ph}}(\mathbf{k},E_{\mathbf{k}})] = \alpha\sqrt{\frac{\omega_{\mathrm{LO}}^3}{E_{\mathbf{k}}}}\ln\left[\frac{\sqrt{\omega_{\mathrm{LO}}+E_{\mathbf{k}}}+\sqrt{E_{\mathbf{k}}}}{\sqrt{\omega_{\mathrm{LO}}+E_{\mathbf{k}}}-\sqrt{E_{\mathbf{k}}}}\right]. \tag{5.15}$$

Many of the following sections will be devoted to deriving expressions similar to those presented here but at the exciton level.

5.4 The Bethe-Salpeter Equation Approach

As discussed in Chap. 2, in the standard *ab initio* reciprocal-space GW-BSE approach, the BSE can be written, in the Tamm-Dancoff approximation [**Rohlfing2000**, 152], as

$$(E_{c\mathbf{k}} - E_{v\mathbf{k}})A^{S}_{cv\mathbf{k}} + \sum_{c'v'\mathbf{k}'} K_{cv\mathbf{k},c'v'\mathbf{k}'}(\Omega_S)A^{S}_{c'v'\mathbf{k}'} = \Omega_S A^{S}_{cv\mathbf{k}}, \tag{5.16}$$

where $E_{c\mathbf{k}}$ and $E_{v\mathbf{k}}$ are the quasiparticle energies of the free electron and hole with band indices and wavevectors $c\mathbf{k}$ and $v\mathbf{k}$, respectively, usually calculated within the GW approximation [43, 53]. Exciton energies and expansion coefficients, in the electron-hole basis, are given by Ω_S, and $A^{S}_{cv\mathbf{k}} = \langle cv\mathbf{k}|S\rangle$ respectively, with S the principal quantum number for the exciton, and $|cv\mathbf{k}\rangle$ the product state of an electron-hole pair, where the components of the products are typically Kohn-Sham wave functions computed with DFT [153].

The electron-hole kernel, K, couples products of the single-particle states and is, at lowest order, written as the sum of two terms, a repulsive exchange term, K^{X}, which is negligible for weakly bound excitons [54], and an attractive direct term, K^{D}, given by, as in Ref. [54],

$$\begin{aligned} K^{\mathrm{D}}_{cv\mathbf{k},c'v'\mathbf{k}'}(\Omega) = -\Bigg\langle cv\mathbf{k}\Bigg|\frac{i}{2\pi}\int d\omega\; e^{-i\omega\eta}W(\mathbf{r},\mathbf{r}';\omega)\times \\ \left[\frac{1}{\Omega-\omega-(E_{c'\mathbf{k}'}-E_{v\mathbf{k}})+i\eta}+\frac{1}{\Omega+\omega-(E_{c\mathbf{k}}-E_{v'\mathbf{k}'})+i\eta}\right]\Bigg|c'v'\mathbf{k}'\Bigg\rangle, \end{aligned} \tag{5.17}$$

where η is again a positive infinitesimal quantity. In general, the BSE must be solved self-consistently, as K^{D} depends on Ω_S and we use the convention

$$\langle cv\mathbf{k}|f(\mathbf{r},\mathbf{r}')|c'v'\mathbf{k}'\rangle \equiv \int d^3\mathbf{r}d^3\mathbf{r}'\psi^{\star}_{c\mathbf{k}}(\mathbf{r})\psi_{c'\mathbf{k}'}(\mathbf{r})f(\mathbf{r},\mathbf{r}')\psi_{v\mathbf{k}}(\mathbf{r}')\psi_{v'\mathbf{k}'}(\mathbf{r}').$$

Plugging Eq. 5.1 into Eq. 5.17, we see that there are two contributions to the direct kernel, one due to electronic screening, W^{el}, which we label K^{el} and one due to phonon screening, W^{ph}, which we label K^{ph}. To date, the vast majority of contemporary BSE calculations only use K^{el} when constructing the direct kernel. Further it is common practice to neglect the frequency dependence in evaluating K^{el} so that

$$K^{\mathrm{el}}_{cv\mathbf{k};c'v'\mathbf{k}'} = -\left\langle cv\mathbf{k}|W^{\mathrm{el}}(\mathbf{r},\mathbf{r}',\omega=0)|c'v'\mathbf{k}'\right\rangle, \tag{5.18}$$

an approximation which is valid in the limit where the intrinsic carrier plasmon frequency is much greater than the exciton binding energy. To the best of our knowledge an equivalent expression for K^{ph}, suitable for present day first principles BSE calculations, has yet to appear in the literature. To derive this correction, we plug Eq. 5.3 into Eq. 5.17 and perform the frequency integral, an easy task given the simple pole structure of the phonon propagator, $D_{\mathbf{q}\nu}$ (see Eq. 5.4). The result is

$$\begin{aligned} K^{\mathrm{ph}}_{cv\mathbf{k},c'v'\mathbf{k}'}(\Omega) = &-g_{cc'\nu}(\mathbf{k}',\mathbf{q})g^{*}_{vv'\nu}(\mathbf{k}',\mathbf{q}) \\ &\times\left[\frac{1}{\Omega-(E_{c'\mathbf{k}'}-E_{v\mathbf{k}})-\omega_{\mathbf{q}\nu}+i\eta}+\frac{1}{\Omega-(E_{c\mathbf{k}}-E_{v'\mathbf{k}'})-\omega_{\mathbf{q}\nu}+i\eta}\right], \end{aligned} \tag{5.19}$$

where $g_{nm\nu}(\mathbf{k}',\mathbf{q}) = \langle m\mathbf{k}'+\mathbf{q}|g_{\mathbf{q}\nu}|n\mathbf{k}'\rangle$, with $\mathbf{q}=\mathbf{k}-\mathbf{k}'$.

Eq. 5.19 represents a central result of work. In its present form, K^{ph} can be added directly to the electron-hole kernel and the BSE solved to include the effect of phonon screening. In practice we find it simpler to work with the phonon kernel in the exciton basis, explicitly

$$K^{\mathrm{ph}}_{SS'}(\Omega) = \sum_{cv\mathbf{k}c'v'\mathbf{k}'} A^{S\star}_{cv\mathbf{k}}K^{\mathrm{ph}}_{cv\mathbf{k},c'v'\mathbf{k}'}(\Omega)A^{S}_{c'v'\mathbf{k}'}, \tag{5.20}$$

In this basis, exciton eigenenergies including renormalization due to phonons, denoted by Ω, are found through solving the characteristic equation

$$\det[(\Omega_S-\Omega)\delta_{SS'}+K^{\mathrm{ph}}_{SS'}(\Omega)] = 0, \tag{5.21}$$

where Ω_S denotes exciton eigenenergies before phonon effects are included. When the entire matrix $\langle S|K^{\mathrm{ph}}|S'\rangle$ is used and Eq. 5.21 solved, the solutions are guaranteed to give the same result as solving the BSE directly with $\langle cv\mathbf{k}|K^{\mathrm{ph}}|\mathbf{k}'c'v'\rangle$ – i.e. we have just chosen to solve the BSE in a different basis. An advantage to working in this basis is that diagonal elements of $K^{\mathrm{ph}}_{SS'}$ are often small relative to the off diagonal elements. In the limit where off-diagonal elements are entirely neglected the characteristic equation decouples to give

$$\Delta\Omega_S = \mathrm{Re}[K^{\mathrm{ph}}_{SS}(\Omega_S + \Delta\Omega_S)], \tag{5.22}$$

where $\Delta\Omega_S = \Omega - \Omega_S$, is the change in the exciton eigenenergy due to phonon screening. As written, Eq. 5.22 must be solved self-consistently as is typical in Brillouin-Wigner perturbation theory. Taking $\Delta\Omega_S = 0$ on the right-hand side of this equation we arrive at the Rayleigh-Schrödinger result, namely

$$\begin{aligned}\Delta\Omega_S &= \mathrm{Re}[K^{\mathrm{ph}}_{SS}(\Omega_S)] \\ &= -\sum_{cv\mathbf{k},c'v'\mathbf{k}'} A^{S\star}_{cv\mathbf{k}} g_{cc'\nu}(\mathbf{k}',\mathbf{q}) g^{*}_{vv'\nu}(\mathbf{k}',\mathbf{q}) A^{S}_{c'v'\mathbf{k}'} \\ &\quad \times \left[\frac{1}{\Omega_S - (E_{c'\mathbf{k}'} - E_{v\mathbf{k}}) - \omega_{\mathbf{q}\nu}} + \frac{1}{\Omega_S - (E_{c\mathbf{k}} - E_{v'\mathbf{k}'}) - \omega_{\mathbf{q}\nu}}\right].\end{aligned} \tag{5.23}$$

It is possible to also derive this final expression directly from second order Rayleigh-Schrödinger perturbation theory. In the next section we compute $\Delta\Omega_S$ after making several justified approximations.

5.5 Results for the CsPbX$_3$ Family

We now use the above formalism to study CsPbX$_3$ lead halide perovskites, with X = Cl, Br, I. For all calculations on lead-halide perovskites, we use experimental lattice parameters reported in Refs. [154, 155], and relax the atomic positions. We study the low temperature orthorhombic phase, with lattice parameters summarized in Table 5.1. All DFT calculations are performed using the generalized gradient approximation within the Perdew Burke Erzerhof parametrization (PBE) [156], including spin orbit coupling as implemented in the QUANTUM ESPRESSO package [157]. For all calculations we use the norm conserving fully relativistic pseudopotentials from the PseudoDojo database [88, 158], with the following valence electrons configuration: Pb ($5d^{10}\ 6s^2\ 6p^4$), I ($5s^2\ 5p^5$), Br ($4s^2\ 4p^5$), Cl ($3s^2 3p^5$) and Cs ($5s^2\ 5p^6\ 6s^1$). We use a plane wave cutoff of 50 Ry and discretize the Brillouin zone using a half shifted Monkhorst-Pack grid of 6 × 4 × 6, following the aspect ratio of the unit cell.

We calculate the quasiparticle eigenvalues of the lead-halide perovskites with a one-shot G_0W_0 approximation as implemented in the BerkeleyGW code [13]. We calculate the static screened Coulomb interaction within the random-phase approximation (RPA) [50, 51], and extend this dielectric function to finite frequencies using the Godby-Needs plasmon pole

	a (Å)	b (Å)	c (Å)	Space Group	Ref.
$CsPbCl_3$	7.902	11.248	7.899	$Pnma$	[154]
$CsPbBr_3$	8.250	11.753	8.204	$Pnma$	[154]
$CsPbI_3$	8.856	8.576	12.472	$Pbnm$	[155]

Table 5.1: Experimental lattice parameters and space groups of the orthorhombic phases of the three halide perovskites studied in this work. Complete structural information can be found in the references cited in the table.

model [52]. We use a half-shifted 4 × 4 × 4 **k**-point mesh, a 14 Ry plane wave cutoff and 1000 bands to calculate the dielectric screening. In addition, we sum over 1000 bands in order to calculate the electronic self-energy on a Γ-centered $4\times4\times4$ **k**-point mesh, following convergence studies reported in Ref. [159], and used the static remainder approximation to optimize convergence with respect to the number of empty states [160]. These computational parameters are similar to previous GW calculations on the quasiparticle band gap in halide perovskites, and are expected to yield band gaps converged within 0.1 eV [155, 159, 161, 162].

In Table 5.2 we compare calculated G_0W_0 band gaps and reduced effective masses to experiment. The computed gaps consistently underestimate experiment by up to 0.5 eV, a shortcoming of one-shot G_0W_0 approximation previously identified in a number of computational studies [135, 163–165]. The reduced effective masses of $CsPbI_3$ and $CsPbBr_3$ agree well with recent magneto-optical measurements at high magnetic fields, while for $CsPbCl_3$ the reduced mass is slightly underestimated with respect to experiment [9, 130].

	E_g^{PBE} (eV)	$E_g^{G_0W_0}$ (eV)	E_g^{exp} (eV)	$\mu(m_e)$	$\mu^{\mathrm{exp}}(m_e)$
$CsPbI_3$	0.85	1.46	1.7 [166]	0.142	0.202 ± 0.01
$CsPbBr_3$	0.95	1.85	2.4 [166]	0.102	0.126 ± 0.02
$CsPbCl_3$	1.35	2.74	3.0 [167]	0.93	0.114 ± 0.01

Table 5.2: Summary of band gaps calculated within DFT+SOC and G_0W_0@PBE + SOC in this work, and compared with experimental band gaps reported in Refs. [166, 167].

In Tab. 5.4 we report exciton binding energies calculated within the standard BSE approach, i.e. including only electronic screening when constructing the electron-hole kernel. We calculate the exciton binding energy by solving the Bethe-Salpeter equation within the Tamm-Dancoff approximation, as implemented in the BerkeleyGW code [13]. We construct the electron-hole kernel on a $4\times4\times4$ **k**-point grid, using 20 valence and 20 conduction bands, which is then interpolated to a fine mesh with 4 valence and 2 conduction bands (spin degenerate). It was previously shown in the case of $MAPbI_3$ that the exciton binding energy is sensitive to the density of the **k**-point mesh used to diagonalize the BSE Hamiltonian, which constitutes the principal bottleneck for the calculation of exciton binding energies in halide perovskites [146]. In order to reach very dense **k**-point meshes, we employ the patched sampling scheme, originally introduced in Ref. [152], whereby for the diagonalization of the BSE Hamiltonian we take into account only **k**-points in a small patch around the Γ-point. The electron-hole interaction kernel and quasiparticle eigenvalues are interpolated on the fine grid using the method described in Ref. [12, 13].

In agreement with previous calculations [146, 147], we find that exciton binding energies neglecting phonon screening overestimate experiment by up to a factor of 3. Despite these discrepancies, after blue-shifting the calculated optical absorption spectrum to align with experiment, we find the lineshape to be in good agreement with measurements at low temperature as seen in Fig. 5.1. We further observe that low-lying optical excitations are well described using a Mott-Wannier hydrogen model. In Figure 5.2 we compare the BSE solutions for the 1s and 2s excitonic states with those predicted by the hydrogen model with μ calculated from G_0W_0 band structure, and with ε_∞ calculated within the RPA [50, 51]. We find a maximum difference between the hydrogenic model and the standard BSE calculations of 6 meV for both 1s and 2s excitonic energies across all three halide perovskites. Finally, in Figure 5.3, we plot the exciton expansion coefficients obtained from our BSE against the analytic expressions for hyrodgenic 1s and 2s states. We take $a = \varepsilon_\infty/\mu$ and find excellent agreement between the BSE excitonic wave functions and the analytic forms.

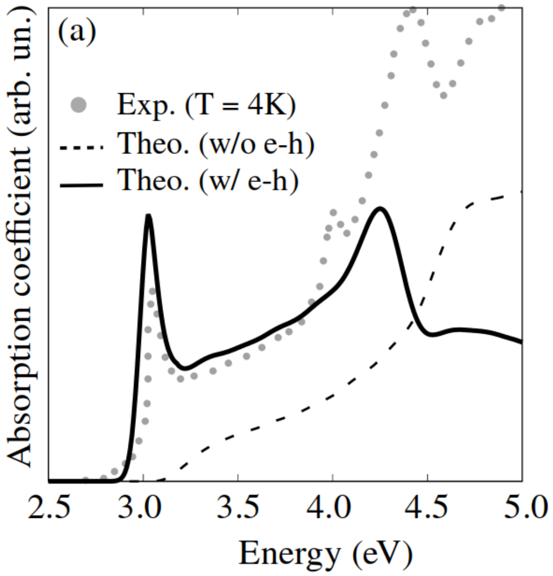

Figure 5.1: Optical absorption spectrum calculated within GW/BSE (continuous line), RPA (dotted line), and from experiment (grey dots) [167] for CsPbCl$_3$. Calculated spectra are blue-shifted by 0.3 eV to match the experimental onset from Ref. [167].

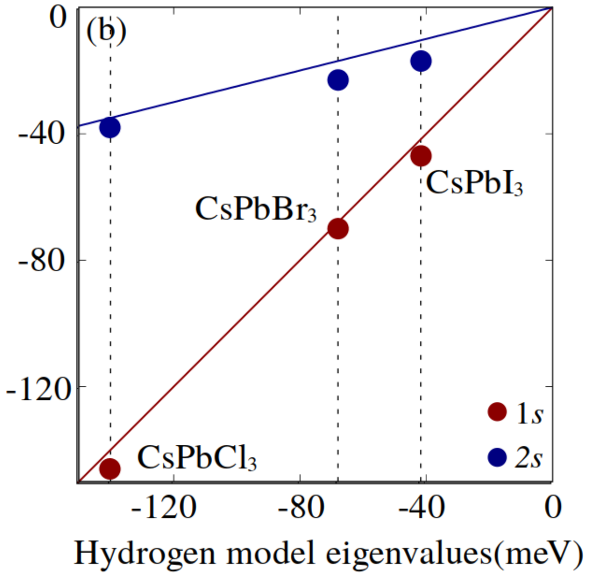

Figure 5.2: Exciton binding energies predicted from GW/BSE (filled circles) and the hydrogen model (lines).

	ω_{LO} (meV)	$\omega^{\mathrm{exp}}_{\mathrm{LO}}$ (meV)	ε_∞	$\varepsilon^{\mathrm{exp}}_\infty$	ε_0
$\mathrm{CsPbI_3}$	14	14.2	5.5	N/A	22.5
$\mathrm{CsPbBr_3}$	18	17.9/20.4	4.5	N/A	18.6
$\mathrm{CsPbCl_3}$	26	25.3/28.0	3.7	3.7	17.5

Table 5.3: Summary of the computed and experimental LO phonon frequencies, ω_{LO}, optical, ε_∞, and static, ε_0, dielectric constants.

To reduce the computational cost associated with a direct evaluation of Eq. 5.23, we make two additional approximations. First we use the analytic hydrogenic expressions for the $1s$ exciton coefficients, namely

$$A^S_{cv\mathbf{k}} \to A_{\mathbf{k}} = \frac{(2a)^{3/2}}{\pi}\frac{1}{[1+a^2k^2]^2} \tag{5.24}$$

where $a = \varepsilon_\infty/\mu$, denotes the exciton radius, an approximation which has already been justified in Fig. 5.3. And second, we approximate the electron-phonon matrix elements using a multi-mode, *ab initio* Fröhlich vertex, introduced in Ref. [23]:

$$g_{mn\nu}(\mathbf{k},\mathbf{q}) \to g_{\mathbf{q}\nu} = i\frac{4\pi}{V_{\mathrm{uc}}}\sum_{\kappa}\left(\frac{1}{2NM_\kappa\omega_{\mathbf{q}\nu}}\right)^{1/2}\frac{\mathbf{q}\cdot\mathbf{Z}_\kappa\cdot\mathbf{e}_{\kappa\nu}(\mathbf{q})}{\mathbf{q}\cdot\varepsilon_\infty\cdot\mathbf{q}}, \tag{5.25}$$

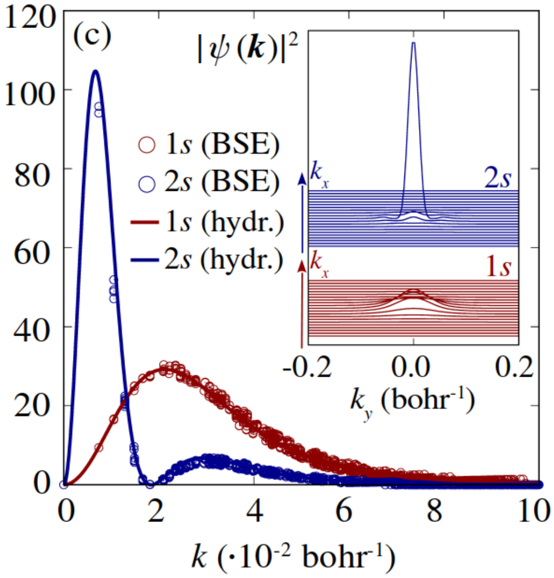

Figure 5.3: Exciton radial probability density (main) and probability of localization (inset) in reciprocal space, calculated from GW/BSE and the hydrogen model for 1s (dark red) and 2s (dark blue) states.

where V_{uc} is the unit cell volume, M_κ are the atomic masses, $\mathbf{Z}_\kappa$ Born effective charge tensor and $\mathbf{e}_{\kappa\nu}(\mathbf{q})$ are the eigenvectors corresponding to the phonon modes, $\omega_{\mathbf{q}\nu}$, for each atom indexed by κ. Here the justification is again given through comparison of the multimode-Fröhlich model with the electron-phonon vertex computed from density functional perturbation theory. In Fig. 5.4, we show that for small q, the two vertices agree very well.

With these simplifications, Eq. 5.23 reduces to

$$\begin{aligned}\Delta\Omega_S &= -\sum_{\mathbf{kq}\nu} A_{\mathbf{k+q}}\left[\frac{|g_{\mathbf{q}\nu}|^2}{\Omega_S-(E_{c\mathbf{k}}-E_{v\mathbf{k+q}})-\omega_{\mathbf{q}\nu}}+\frac{|g_{\mathbf{q}\nu}|^2}{\Omega_S-(E_{c\mathbf{k+q}}-E_{v\mathbf{k}})-\omega_{\mathbf{q}\nu}}\right]A_{\mathbf{k}}\\ &\equiv -\sum_{\mathbf{kq}} A_{\mathbf{k+q}}K^{\mathrm{ph}}(\mathbf{k},\mathbf{q})A_{\mathbf{k}},\end{aligned} \tag{5.26}$$

where we have dropped the primes on the band indicies since we are now working in a two band model. To recover the Brillouin-Wigner result we could replace Ω_S appearing in the energy denominator with $\Omega_S+\Delta\Omega_S$ and then solve the equation self consistently. In practice we find the Brillouin-Wigner result and Rayleigh-Schrödinger result differ by less than 1 meV so we will stick with Eq. 5.26 going forward. Finally, by definition, the change in the exciton binding energy is $\Delta E_B = -\Delta\Omega_S$.

The standard BSE exciton binding energies and phonon screening corrections are summarized in Table 5.4 for all three $\mathrm{CsPbX_3}$ perovskites. We find that phonon screening

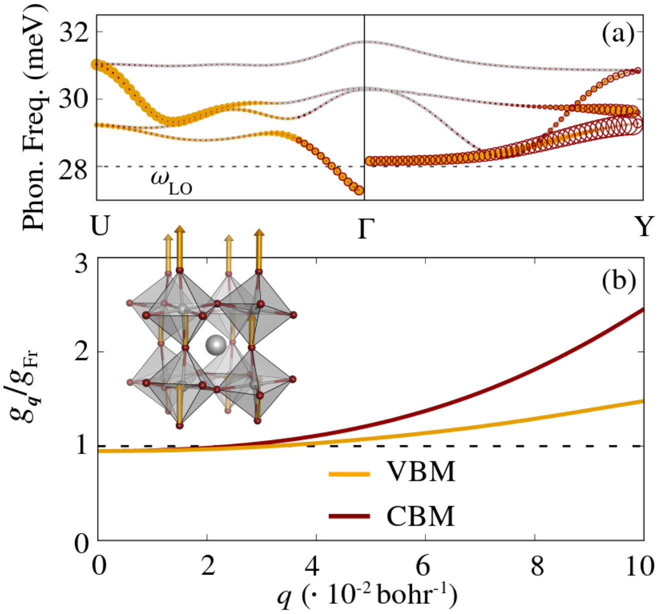

Figure 5.4: In panel (a) the DFPT phonon dispersion is shown. The overlayed red and yellow circles are the magnitude of the phonon vertex $|\mathbf{q}|g_{\mathbf{q}}$ for the CBM and VBM respectively. In panel (b) the ratio of the DFPT to Fröhlich vertex is plotted as a function of $\mathbf{q}$.

contributes to the reduction of the exciton binding energy between 12% and 17% for the $CsPbX_3$ series, improving the agreement with measurements reported in Refs. [166, 168, 169]. However, for $CsPbI_3$, our calculated relative phonon screening correction of 17% is less than half of the 50% correction predicted in Ref. [147]; as we show in the following, this discrepancy can be attributed to electronic band dispersion contributions, accounted for here but neglected in prior work.

	E_B (meV)	ΔE_B (meV)	E_B^{exp} (meV)
$CsPbI_3$	47	-8	15 ± 1
$CsPbBr_3$	70	-12	33 ± 1; 38 ± 3
$CsPbCl_3$	146	-17	72 ± 3; 64 ± 1.5

Table 5.4: Exciton binding energy computed from BSE, E_B with only the electronic contribution, the correction due to phonon screening ΔE_B, and experimentally measured values.

To further investigate the contribution of phonon screening to the exciton binding energy, we perform a spectral decomposition on the phonon kernel in Fig. 5.5. For all three halide perovskites, we find that the contribution of the highest lying IR active phonons accounts for more than 90% of the expectation value of K^{ph}, with the remaining contribution due to the lower energy LO modes. Furthermore, as shown in Fig. 5.5, the phonon kernel drops sharply outside of the $\mathbf{q} \to 0$ range, a trend attributed to the strong localization of the exciton wavefunction around the center of the Brillouin zone, and the fast decay of the long-range electron-phonon vertex in reciprocal space.

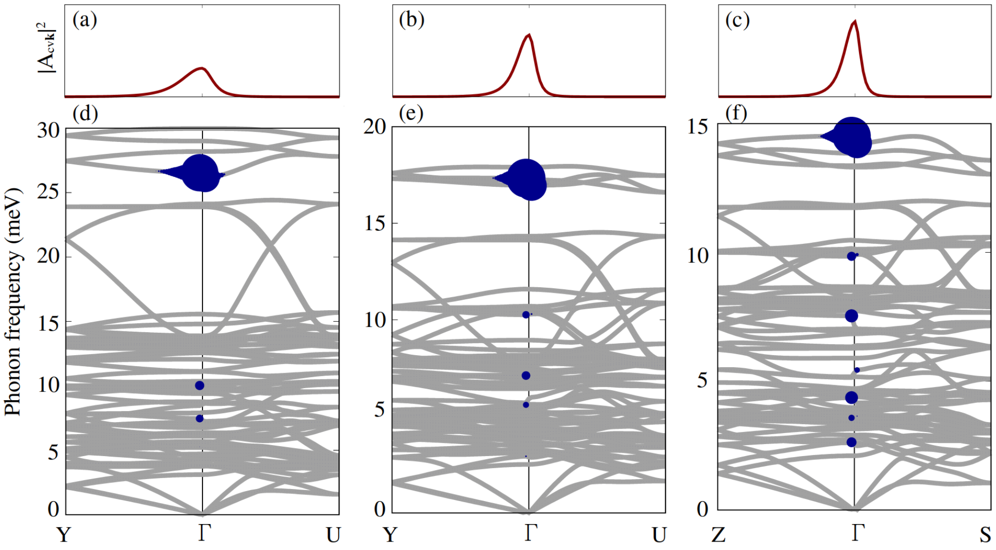

Figure 5.5: Exciton wave functions plotted along the high symmetry path for $CsPbCl_3$ (a), $CsPbBr_3$ (b) and $CsPbI_3$ (c). Phonon decomposition of the phonon screening correction computed using the *ab initio* Fröhlich vertex (dark blue circles) overlayed over the phonon dispersion spectrum $CsPbCl_3$ (d), $CsPbBr_3$ (e) and $CsPbI_3$ (f) from DFPT. The size of the points is proportional the phonon screening correction, in logarithmic scale.

5.6 Relation to the Haken Potential and Derivation of Model Expressions

As pointed out by Strinati [54], the phonon kernel is closely related to Haken's potential. We briefly outline the connection here and use these results to derive a simple correction to the exciton binding energy in terms the ratios ω_{LO}/E_B and $\varepsilon_\infty/\varepsilon_0$. We take Eq. 5.23 as our starting point and insert Fourier transforms to express the first order correction as an integral in real space. We find

$$\Delta\Omega_S = \int d^3\mathbf{r} d^3\mathbf{r}' F^\star(\mathbf{r}) v_{\mathrm{eff}}(\mathbf{r},\mathbf{r}') F(\mathbf{r}') \tag{5.27}$$

where

$$F(\mathbf{r}) = \sum_{\mathbf{k}} e^{i\mathbf{k}\cdot\mathbf{r}} A_{\mathbf{k}} = \frac{1}{\sqrt{\pi a^3}} e^{-r/a}, \tag{5.28}$$

and

$$v_{\text{eff}}(\mathbf{r}, \mathbf{r}') = \sum_{\mathbf{kq}} e^{i(\mathbf{k}+\mathbf{q})\cdot\mathbf{r}} K^{\text{ph}}(\mathbf{k}, \mathbf{q}) e^{-i(\mathbf{k}+\mathbf{q})\cdot\mathbf{r}'}, \tag{5.29}$$

with $K^{\text{ph}}(\mathbf{k}, \mathbf{q})$ is defined in Eq. 5.23. For general $K^{\text{ph}}(\mathbf{k}, \mathbf{q})$, $v_{\text{eff}}(\mathbf{r}, \mathbf{r}')$ is nonlocal. However in the limit where $K^{\text{ph}}(\mathbf{k}, \mathbf{q})$ depends only on $\mathbf{q}$, v_{eff} becomes entirely local in $\mathbf{r}$ and takes the form of an effective central potential – ie, $v_{\text{eff}}(\mathbf{r}, \mathbf{r}') = v_{\text{eff}}(\mathbf{r})\delta(\mathbf{r}-\mathbf{r}')$. To derive a specific from for K^{ph} starting from Eq. 5.23, we now make several approximations. We (i) restrict ourselves to a single dispersionless longitudinal-optical mode with energy ω_{LO} which couples to both the electron and hole through a traditional Fröhlich vertex (see Eq. 5.10), (ii) assume the conduction and valence energies appearing in Eq. 5.23 are described near the band edge by parabolic bands with effective masses m_e and m_h respectively. Under these approximations,

$$\begin{aligned} v_{\text{eff}}(\mathbf{r}, \mathbf{r}') = \frac{\omega_{\text{LO}}}{2}\left(\frac{1}{\varepsilon_\infty} - \frac{1}{\varepsilon_0}\right) \sum_{\mathbf{kq}} e^{i(\mathbf{k}+\mathbf{q})\cdot\mathbf{r}} \frac{4\pi}{q^2} \Bigg[& \frac{1}{E_B + \mathbf{k}^2/2m_e + (\mathbf{k}+\mathbf{q})^2/2m_h + \omega_{\text{LO}}} \\ & + \frac{1}{E_B + (\mathbf{k}+\mathbf{q})^2/2m_e + \mathbf{k}^2/2m_h + \omega_{\text{LO}}} \Bigg] e^{i\mathbf{k}\cdot\mathbf{r}'}, \end{aligned} \tag{5.30}$$

where E_B is the exciton binding energy. For excitons which are very localized in $\mathbf{k}$-space, such as hydrogenic excitons, it may be appropriate to neglect their $\mathbf{k}$ dependence, then the Fourier transform is readily performed to arrive at the following effective potential

$$v_{\text{eff}}(\mathbf{r}, \mathbf{r}') = \frac{1}{2} \frac{\omega_{\text{LO}}}{\omega_{\text{LO}} + E_B} \left(\frac{1}{\varepsilon_\infty} - \frac{1}{\varepsilon_0}\right) \frac{1}{r} (e^{-r/r_e} + e^{-r/r_h}) \delta(\mathbf{r} - \mathbf{r}'), \tag{5.31}$$

where, $r_{e,h}$ take the form

$$r_{e,h} = \sqrt{\frac{1}{2m_{e,h}(E_B + \omega_{\text{LO}})}}. \tag{5.32}$$

In the limit $E_B \to 0$, $r_{e,h}$ coincides with the conventional definition of the polaron radius. Further, in this limit, $v_{\text{eff}}(\mathbf{r})$ reduces to the effective potential derived by Haken, for an exciton coupled to a polar phonon. Going forward, we retain the E_B dependence as in many systems of interest the exciton binding energy is similar or even larger in magnitude than the energy of the screening phonon. To compute the change in energy associated with this effective potential, we plug Eq. 5.31 into Eq. 5.27 to find

$$\Delta E_B = -2\omega_{\text{LO}}\left(1 - \frac{\varepsilon_\infty}{\varepsilon_0}\right) \frac{1}{(1 + \omega_{\text{LO}}/E_B)(1 + \sqrt{1/2 + \omega_{\text{LO}}/(2E_B)})^2} \qquad (\mathbf{k} = 0 \text{ approx.}), \tag{5.33}$$

In Ref. [125], instead of neglecting the $\mathbf{k}$ dependence in $K^{\mathrm{ph}}(\mathbf{k}, \mathbf{q})$, we neglect the $\mathbf{q}$ dependence of the interacting phonon. With this approximation, a similar, though not entirely equivalent, expression for the change in exciton binding energy can be derived. We find

$$\Delta E_B = -2\omega_{\mathrm{LO}}\left(1 - \frac{\epsilon_\infty}{\varepsilon_0}\right)\frac{\sqrt{1+\omega_{\mathrm{LO}}/E_B}+3}{\left(1+\sqrt{1+\omega_{\mathrm{LO}}/E_B}\right)^3} \qquad (\mathbf{q}=0 \text{ approx.}). \tag{5.34}$$

Since the exciton wave function is highly localized at the center of the Brillouin zone (see Fig. 5.5), it is tempting to assume that the dispersion of the electronic band structure may also be neglected. This approximation leads to an even simpler expression for the change in the exciton binding energy, namely

$$\Delta E_B = -2\omega_{\mathrm{LO}}\left(1 - \frac{\varepsilon_\infty}{\varepsilon_0}\right)\frac{1}{1+\omega_{\mathrm{LO}}/E_B} \qquad (\mathbf{k}=\mathbf{q}=0 \text{ approx.}). \tag{5.35}$$

We note that in the $\omega_{\mathrm{LO}}/E_B \gg 1$ limit Eqs. 5.33, 5.34, and 5.35 approach $\sim 1/3, 1$ and 2 times the quantity $-\omega_{\mathrm{LO}}(1-\varepsilon_\infty/\varepsilon_0)$ respectively. The discrepancy highlights the care with which one must use when working with these model expressions. In Tab. 5.5, we compare the results of these simple analytic models to the numerical results computed with Eq. 5.23. For the lead-halide perovskites, we find that Eq. 5.34 performs best. We emphasize that this may not always be the case and the performance of a given model maybe be material specific. Nevertheless, in the following paragraphs we will work with this particular model to build a qualitative understanding for how the exciton binding energy is renormalized of over a wide range of material parameters.

	Numeric (meV)	Eq. 5.33 (meV)	Eq. 5.34 (meV)	Eq. 5.35 (meV)
$CsPbI_3$	-8	-5	-9	-15
$CsPbBr_3$	-12	-6	-12	-18
$CsPbCl_3$	-17	-9	-19	-30

Table 5.5: Summary of how model corrections in Eqs. 5.33- 5.35 compare with the numeric results computed according to Eq. 5.23 .

To examine phonon screening trends across a wide range of semiconductors and insulators, we plot the phonon kernel relative to the bare exciton binding energy E_B, $|\Delta E_B|/E_B$, as a function of E_B/ω_{LO}, and $\varepsilon_0/\varepsilon_\infty$, in Figure 5.6, following Eq. 5.34. We overlay our calculations for the $CsPbX_3$ series, as well as some other isotropic semiconductors and insulators such as CdS, GaN, AlN and MgO. In all cases considered, the inclusion of phonon screening effects reduces the exciton binding energy significantly, bringing calculated values in closer agreement with experiment.

Particularly for halide perovskites, our calculations reconcile prior reports, and clearly establish the importance of phonon screening effects for excitons in halide perovskites, in

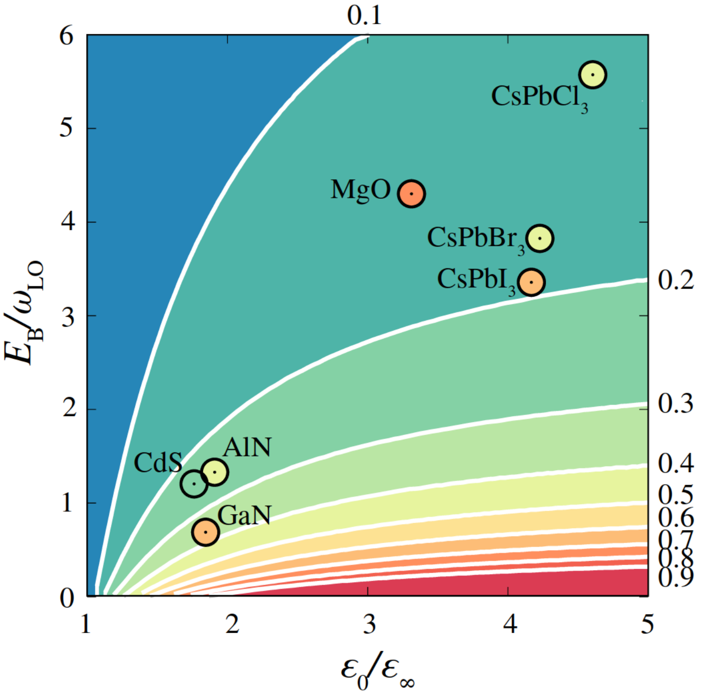

Figure 5.6: Color map of $\Delta E_B/E_B$, calculated using Eq. 5.34, as a function of $\varepsilon_0/\varepsilon_\infty$ and E_B/ω_{LO}. The isoline values are marked at the upper and rightmost edge of the plot. The color of each circle corresponds to the ratio $(E_B - E_B^{\text{exp}})/E_B$, as read on the color map.

agreement with Ref. [147]. However, corrections due to phonon screening do not fully account for the discrepancy between calculated and measured exciton binding energies. Considering the systematic overestimation of exciton binding energies for all systems beyond halide perovskites, we expect that the net contribution of polaronic mass enhancement [170] and interference effects [132] will further reduce the exciton binding energies and improve the agreement with experiment, as proposed by Ref. [17, 132] for MgO and several other semiconductors. However, G_0W_0-BSE calculations of halide perovskites are known to exhibit a strong dependence to the mean-field starting point [164], and the electron-phonon matrix elements, computed starting from the standard Kohn-Sham eigensystem may underestimate couplings obtained from higher level theory [171, 172]. Therefore, a detailed benchmarking of these effects is required, in addition to simply including polaronic effects. While we reserve this detailed analysis to future studies, we emphasize that the relative phonon screening correction derived in this study is robust, and the formalism introduced here is independent of the choice of computational setup.

As a general trend, Figure 5.6 highlights that the magnitude of the phonon screening correction increases as the ratio E_B/ω_{LO} decreases, and in systems with a large static dielectric constant. Further, all parameters appearing in Eq. 5.34 and depicted in Figure 5.6 can be readily computed or measured experimentally so that this simplified picture can be used in both theoretical and experimental contexts to directly assess the expected phonon screening correction to the bare exciton binding energy, and identify systems for which phonon screening is expected to be significant.

5.7 Polaronic Effects

Up to this point we have neglected the renormalization of the underlying electronic states which compose the exciton. However, the analysis of Sec. 5.3 suggests that, from a theoretical standpoint, this renormalization should be included. To qualitatively appreciate the effect of naively including polaronic effects, we assume both the electron and hole couple with the same strength, α, to an LO phonon. In the weak coupling limit, the exciton binding energy is enhanced to $E_B \rightarrow E_B/(1-\alpha/6)$ which follows immediately from the Eq. 5.13 and the linear dependence of E_B on the reduced effective mass. In all model expressions for renormalization of the binding energy due to phonon effects, we find that the correction, ΔE_B, decreases (becomes less negative) with increasing E_B. Both these results will tend to increase the exciton binding energy, undoing the effect of K^{ph} and worsening agreement with experiment.

That naive renormalization of the underlying electron and hole bands leads to worse agreement with experiment has been pointed out before [132] and is linked to so-called polaron interference effects. To illustrate the concept of polaron interference, in Fig. 5.7 we give a high level illustration of separating an exciton-polaron. When the electron and hole polaron are far apart, the lattice can relax about the carriers without issue. We refer to the ionic distortion which follows the electron (hole) as a polaron cloud. Now when the electron and hole are nearby, their polaron clouds overlap and the ionic relaxation is reduced. We refer to this overlap as polaron interference. Clearly the magnitude of the reorganization energy associated with the exciton, λ_{xct}, is smaller than the sum of the reorganization energies of an electron and hole which are well separated, $\lambda_e + \lambda_h$.

To see the effect polaron interference has on the exciton binding energy, consider a system with fundamental gap, E_g, and exciton energy Ω_S. Before phonon screening is taken into account, the binding energy is given by $E_B = E_g - \Omega_S$ (with this convention the binding energy is positive). When the polaronic interference is taken into account both the energy gap and exciton energy are reduced by $\lambda_e + \lambda_h$ and λ_{xct} respectively. So that the binding energy is now $E_B = (E_g - (\lambda_e + \lambda_h)) - (\Omega_S - \lambda_{\text{xct}})$. The change in the binding energy after including polaronic interference is $\Delta E_B = \lambda_{xct} - (\lambda_e + \lambda_h) < 0$, where the last inequality follows from the fact that $(\lambda_e + \lambda_h) > \lambda_{\text{xct}}$ – i.e. the energy associated with the sum of individual electron and hole relaxation exceeds the energy associated with relaxation about entire exciton due to interference effects as discussed above.

The effect is difficult to capture with our formalism since ionic relaxation is typically poorly described with perturbative methods. In our present formulation it is especially difficult given we have only included the lowest order term in W^{ph}. In Sec. 5.2 we saw that

Figure 5.7: Depiction of the polaron cloud interference for nearby electron-, hole-polarons (left most panel) and distant electron-, hole-polarons, (rightmost panel). Grey dots are the pristine lattice while teal dots show how the lattice distorts in the presence of the electon and hole.

this included the exchange of only a single phonon. By contrast, we expect that the polaron interference effect we have just described would require multiple phonon propagators. It is possible that higher order perturbation theory may be able to capture this effect and it will be interesting to investigate this in the future.

5.8 Phonon Assisted Exciton Dissociation

In this work, we focused exclusively on the real part of the phonon kernel, $\mathrm{Re}[K^{\mathrm{ph}}]$, however the imaginary component, $\mathrm{Im}[K^{\mathrm{ph}}]$, also contains valuable information. Specifically, the imaginary part is related to rate of phonon assisted exciton dissociation into free electron-hole pairs, namely

$$\begin{aligned}\mathrm{Im}[K^{\mathrm{ph}}_{SS}(\Omega_S)] = \pi \sum_{cc'vv'\mathbf{kq}} & A^{S\star}_{cv\mathbf{k+q}} g_{cc'\nu}(\mathbf{k},\mathbf{q}) g_{vv'\nu}(\mathbf{k},\mathbf{q}) A^{S}_{c'v'\mathbf{k}} \\ & \times \Big[\delta(\Omega_S - (E_{c'\mathbf{k}} - E_{v\mathbf{k+q}}) - \omega_{\mathbf{q}\nu}) + \delta(\Omega_S - (E_{c\mathbf{k+q}} - E_{v'\mathbf{k}}) - \omega_{\mathbf{q}\nu})\Big]\end{aligned} \tag{5.36}$$

To understand Eq. 5.36, we start with the delta functions. The delta functions enforce the energy/momentum conservation laws

$$\begin{aligned}\Omega_S - \omega_{\mathbf{q}\nu} &= (E_{c'\mathbf{k+q}} - E_{v\mathbf{k}}) \\ \Omega_S - \omega_{\mathbf{q}\nu} &= (E_{c\mathbf{k}} - E_{v'\mathbf{k+q}}).\end{aligned} \tag{5.37}$$

The energy conservation here is for a process where an initial exciton with energy Ω_S emits a phonon with energy with energy $\omega_{\mathbf{q}\nu}$ and scatters a free electron hole pair with energy

$(E_{c\mathbf{k}+\mathbf{q}} - E_{v\mathbf{k}})$ or $(E_{c\mathbf{k}} - E_{v\mathbf{k}+\mathbf{q}})$. That there are two energy conditions reflects the fact that the phonon momentum can be imparted either to the electron or hole and we must weigh both processes equally when computing the dissociation rate.

For direct gap materials we expect the energy condition given in Eq. 5.37 is never met for bound excitons because $\Omega_S < E_g$ where E_g is the fundamental gap. By contrast for the indirect gap materials, for instance silicon, where the band gap is 3eV and the indirect gap 1.1 eV, we expect there should be some phase space for this scattering event to occur. If Eq. 5.36 is generalized to include finite temperatures, we expect additional delta functions which allow for processes where a bound exciton absorbs a phonon and scatters to a free electron-hole state. The result can also be derived directly from Rayleigh-Schrödinger perturbation theory.

It would be of significant interest to derive an analytic approximation to Eq. 5.36 in the spirit of those derived at the single electron and hole level in Sec. 5.3.

5.9 Screening of Excitons Due to Carrier Plasmon

The framework outlined here for including dynamical sources of screening beyond the usual electronic contribution is of general nature and can be easily adapted to include other sources of dynamical screening. An important example is screening due to carrier plasmons in doped semiconductors. Briefly, in much the same way that polar phonons contribute to the total screened Coulomb interaction, we expect carrier plasmons will also provide a contribution to the dielectric function, namely

$$W^{\text{plasmon}}(\mathbf{q},\omega) = \left[\left(\frac{1}{\varepsilon_\infty} - \frac{1}{\varepsilon_0}\right)\frac{\omega_p^2(\mathbf{q})}{\omega^2 - \omega_p^2(\mathbf{q}) + i\eta}\right]v_c(\mathbf{q}). \tag{5.38}$$

where $\omega_p^2(\mathbf{q})$ is the carrier plasmon frequency, proportional to the doping density, n. Indeed such a framework was previously explored in [173]. In work to be published we consider the effect doping has on exciton properties in monolayer TMDs specifically MoTe_2 explicitly adapting Eq. 5.38 to include local field effects.

5.10 Conclusion

In summary, we generalized the *ab initio* Bethe-Salpeter equation approach to include both electronic and phonon contributions to the screened Coulomb interaction, W, and studied phonon screening effects on the electron-hole interactions in halide perovskites and other important semiconductors. We showed that *ab initio* BSE calculations including phonon screening can reduce the exciton binding energy of lead-halide perovskites significantly as compared to electronic screening alone, reconciling two previous contradictory hypotheses on the importance of phonon screening in metal-halide perovskites. We rationalized our results by generalizing the Wannier-Mott model for excitons in a phonon-screened environment. Within this model, we showed that phonon screening is important for other semiconductors, and can be traced back to four material specific parameters, μ, ω_{LO}, ε_∞ and ε_0. We derived a simple expression providing intuition for the importance of lattice vibrations on the excitonic properties of materials and outlined a general, simple, and quantitative approach to estimate the exciton binding energy correction using physical quantities that can be readily calculated theoretically or measured experimentally. By introducing a general framework to quantitatively account for phonon screening in *ab initio* BSE calculations, our study clarifies the importance of phonon screening corrections, and provides a necessary foundation for future treatment of polarons and higher order processes beyond two particle excitations for these and other complex materials.

Chapter 6

Exciton-Phonon Dephasing and Linewidth From First-Principles in Monolayer MoS2

This chapter is adapted from work done in collaboration with lead author Yang-Hao Chan, as well as Mit Naik, Diana Qiu, and Felipe da Jornada. At the time of writing this work is not yet in print.

6.1 Introduction

In low-dimensional or nanostructured semiconductors, the low-energy excitations are dominated by strongly bound correlated electron-hole pairs known as excitons. Understanding exciton energetics and dynamics is essential for diverse applications across optoelectronics, quantum information and sensing, as well as energy harvesting and conversion. By now, it is well-established that these large excitonic effects are a combined consequence of quantum confinement and reduced screening in low dimensions [136, 174–176]. However, many challenges remain in understanding the dynamics of these excitons, especially when it comes to correlating complex experimental signatures with underlying dynamical processes through the use of quantitatively predictive *ab initio* theories.

Exciton-phonon interactions play a key role in determining exciton nonradiative dynamics, decoherence times, temperature-dependent behavior, linewidths, and diffusion. Experimentally, exciton-phonon interaction can be probed by various spectroscopic methods including absorption, photoluminescence, and four-wave mixing measurements. For example, the exciton-phonon coupling strength has been inferred for various transition metal dichalogenides (TMDs), such as WSe_2 and MoS_2, based on the spectroscopic linewidth or the evolution of exciton spectral intensity in pump-probe setups. However, the reported lifetimes vary by an order of magnitude [177–179] as a consequence of variations in substrate and sample preparations, highlighting the need for accurate first principles theories.

On the theoretical side, *ab initio* methods for determining electron-phonon interactions using density-functional perturbation theory (DFPT) are by now well-established [27, 180]. In the limit where the exciton binding energy is small, one can approximate the exciton-phonon renormalization of the exciton energy and linewidth in terms of the electron-phonon renormalization for the constituent electrons and holes of each exciton state [181], and it has been demonstrated that such a simplified approach is nonetheless essential for reproducing the experimental line-shape in optical spectra of monolayer MoS_2 [136, 182]. At a higher level of theory, one can also derive the exciton-phonon coupling matrix elements and the self-energy within many-body perturbation theory [19, 24, 75, 183–187], and the diagonal part of the exciton-phonon self-energy has been recently applied to study exciton-phonon interactions in bulk hexagonal boron nitride [75, 188]. However, model calculations based on the semiconductor Bloch equations suggest that off-diagonal contributions to the electron-phonon self-energy, which have thus far been overlooked in *ab initio* calculations, may play an important role in the exciton linewidth [189–192]. The full phase space of *ab initio* calculations of exciton-phonon interactions in low-dimensional materials, where exciton effects are strongest, has also not yet been explored, with extant studies limited to either frozen phonons [193] or Γ-point only [194].

6.2 Exciton Dispersion and Relaxation in MoS_2

Motivated by the great interest in exciton dynamics and the lack of a predictive *ab initio* theory, we develop an *ab initio* theory to study exciton-phonon coupling and apply it to compute both exciton relaxation and the lineshape of the absorption spectrum in monolayer MoS_2, a prototypical quasi two-dimensional (quasi-2D) material. Using a fully relativistic formalism, we reveal that the relaxation time of the lowest-energy bright A exciton due to exciton-phonon interactions is longer than that of the lower-energy spin forbidden states. This counterintuitive result arises as a consequence of the selection rules of the exciton-phonon coupling, which do not allow for direct intervalley scattering from the A state. We show that phonon-mediated intervalley exciton scattering must be facilitated through other valleys in the conduction band [195, 196]. Additionally, we find that the absorption spectrum of the A exciton features an asymmetric lineshape due to interference effects from transitions between distinct exciton bands, which cannot be understood in the context of previous *ab initio* theories. The computed linewidth and energy shift in the absorption spectrum with interference effects are in excellent agreement with experimental results.

Computational details for our calculation are given below. DFT calculations are performed with the Quantum Espresso [86] package. We use PBE pseudopotentials [87] from the SG15 ONCV potentials database [88, 197]. For the ground state calculation, we use a $\mathbf{k}$-mesh of $12 \times 12 \times 1$ and a plane wave energy cutoff of 80 Ry. A vacuum of 15 Å is chosen to prevent spurious interactions between periodic images. The GW-BSE calculation is done in the BerkeleyGW package [11–13]. A k-point grid of $24 \times 24 \times 1$ with a subsampling of 10 points in the mini-Brillouin zone [198] and dielectric energy cutoff 10 Ry and 5000 bands are

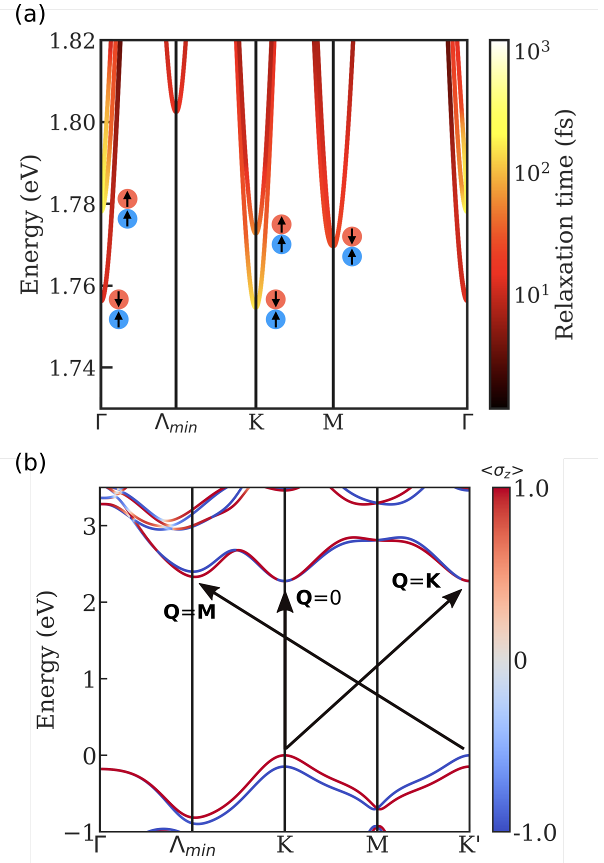

Figure 6.1: (a) Exciton dispersion of monolayer MoS_2 including both spin-allowed and spin-forbidden states. Color indicates the relaxation time due to exciton-phonon coupling at 300K. Dots with arrows indicate the internal spin structure of excitons at valleys. (b) Electron band dispersion with a color map of spin expectation values. Energy transition corresponding to excitons with center of mass momentum $\mathbf{Q} = \Gamma$, $\mathbf{Q} = K$, and $\mathbf{Q} = M$ are shown with the labeled arrows. The other $\mathbf{Q} = M$ excitons with the transition from K' valley valence electron to Λ_{min} conduction electron is not shown.

used in GW calculation. The frequency-dependence of the dielectric screening is computed using the Hybertsen-Louie generalized plasmon pole model [11]. The direct band gap in our DFT calculation is 1.77 eV and the GW corrected direct band gap is 2.27 eV. BSE with finite exciton COM $\mathbf{Q}$ are solved on a uniform 48×48 grid including 4 conduction and 4 valence bands.

Phonon calculations are performed with the density functional perturbation theory method (DFPT) implemented in the Quantum Espresso package. We solve phonon and perturbed self-consistent potential on a uniform 48×48 $\mathbf{q}$-grid. Electron-phonon coupling matrix elements are then computed with EPW package [16, 62]

We first analyze the exciton dispersion of $\mathrm{MoS_2}$ by solving the Bethe-Salpeter equation for excitons with finite center-of-mass (COM) momentum $\mathbf{Q}$. Fig. 6.1 (a) shows the dispersion along a high symmetry path. The lowest energy exciton states at Γ are doubly degenerate spin-forbidden ($S^{\mathrm{tot}} = 1$) dark excitons. We use the total spin S^{tot} to label exciton states, which is approximately a good quantum number in the K valleys even in the presence of SOC. Two bright exciton states, corresponding to the 'A' peak, are about 20 meV higher in energy. These bright exciton bands are doubly degenerate at Γ, with one band dispersing linearly and one band dispersing parabolically, consistent with previous calculations [55, 74]. The lowest-energy exciton with $\mathbf{Q} = K$ consists of electrons and holes from the K and K' valleys, respectively, (Fig. 6.1 (b)) and is a spin-forbidden state. In contrast, the second-lowest $\mathbf{Q} = K$ exciton is a spin-allowed ($S^{\mathrm{tot}} = 0$) state. The lowest energy $\mathbf{Q} = M$ exciton also consists of a spin-forbidden state – composed of a hole in the K' valley and an electron in the conduction band valley along the Λ high-symmetry line (i.e., the Λ_{min} valley) –, while the second lowest-energy exciton is a spin-allowed state. This well-defined internal spin-texture of the excitons, leads to strict selection rules for exciton-phonon coupling that significantly extend the lifetime of the spin-allowed states, as we discuss later.

Exciton-phonon coupling matrix elements can be written as a superposition of electron-phonon coupling matrix elements weighted by the exciton envelope function as derived in previous works [19, 24, 75]. The lowest-order exciton-phonon self-energy expression derived from many-body perturbation theory is similar to the Fan-Migdal term in the electron-phonon self-energy and reads

$$\Sigma_{S\mathbf{Q}}(\omega) = \frac{1}{N_{\mathbf{q}}} \sum_{S',\mathbf{q},\nu,\pm} \frac{|G_{S'S\nu}(\mathbf{Q},\mathbf{q})|^2 (N_{\nu\mathbf{q}} + \frac{1}{2} \pm \frac{1}{2})}{\omega - E_{S'\mathbf{Q}+\mathbf{q}} \mp \omega_{\nu\mathbf{q}} + i\eta}, \tag{6.1}$$

where $E_{S'\mathbf{Q}+\mathbf{q}}$ is the exciton energy of a state with principle quantum number S' and a COM momentum $\mathbf{Q} + \mathbf{q}$; $\omega_{\nu\mathbf{q}}$ and $N_{\nu\mathbf{q}}$ are the phonon frequency and Bose-Einstein occupation factor with ν labeling the branch index and $\mathbf{q}$ the crystal momentum; $N_{\mathbf{q}}$ is the number of the wavevectors sampled in the Brillouin zone; and finally, $G_{S'S\nu}(\mathbf{Q},\mathbf{q})$ is the exciton-phonon coupling matrix element encoding the probability amplitude for an exciton initially in state $(S,\mathbf{Q})$ to scatter to state $(S',\mathbf{Q}+\mathbf{q})$ through the emission or absorption of a phonon $(\nu, \pm\mathbf{q})$. The real part of Eq. 6.1 determines exciton energy renormalization while the imaginary part is proportional to the phonon-limited relaxation time of excitons.

We show in Fig. 1 (a) the calculated exciton dispersion and a color map of the exciton-phonon relaxation times in monolayer $\mathrm{MoS_2}$ at 300K. In our calculation and consistent with previous results [55], the lowest-energy exciton has a COM momentum $\mathbf{Q} = K$ while the lowest exciton with momentum $\mathbf{Q} = \Gamma$ is 1.7 meV higher in energy. Consequently, the lowest energy $\mathbf{Q} = K$ exciton has a longer lifetime of about 100 fs, since the available phase space for exciton-phonon scattering is limited at the band edge. However, to our surprise, the first bright exciton, the zero-momentum A exciton, also has a long lifetime comparable with the lowest $\mathbf{Q} = K$ exciton, while the lowest energy dark exciton at Γ has a much shorter lifetime.

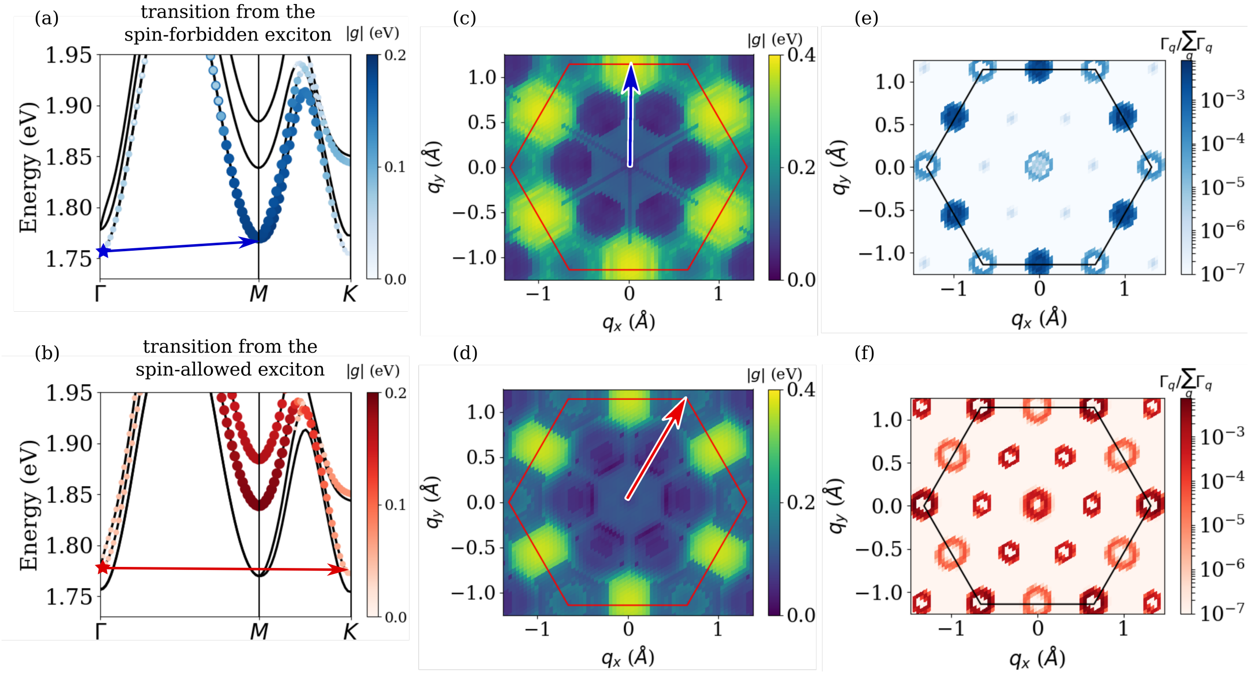

Figure 6.2: Exciton-phonon coupling strength and phonon momentum **q**-resolved contribution to the total scattering rate for the lowest spin-forbidden (blue star and panel (a),(c),(e)) and spin-allowed exciton (red star and panel (b),(d),(f)) state with a center of mass momentum $\mathbf{Q} = \Gamma$. The color map and symbol sizes in (a) and (b) indicate the coupling strength from the starred state to other states summed over phonon modes. (c) and (d) are color maps of coupling strength from the starred state to the lowest four states in the full BZ summed over exciton states and phonon modes. (e) and (f) show the normalized contribution to the scattering rate of the starred state from different phonon momentum **q**. Arrows in (a), (b), (c), and (d) highlight the region of large contribution to the scattering rate as shown in (e) and (f). (a) and (b) show strong state-selective couplings due to spin structure of the excitons.

This is counterintuitive as one would expect the available scattering phase space for the A exciton to be larger than the lowest energy dark exciton with the same COM momentum.

To understand this result, we analyze momentum and state-resolved exciton-phonon coupling in Fig. 6.2. In Fig. 6.2 (a) and (b) we show color maps of the absolute value of exciton-phonon coupling strength from the lowest-energy $\mathbf{Q} = \Gamma$ exciton (blue-starred) and the A exciton (red-starred) to other states summed over all phonon modes. We observe that both excitons are strongly coupled to $\mathbf{Q} = M$ excitons in the same bands while the coupling strength is zero to excitons in other bands with a different internal spin structure, which is well-defined for electronic states around M and K. For example, the A exciton does not couple to the lowest two $\mathbf{Q} = M$ excitons and the lowest-energy $\mathbf{Q} = K$ exciton. This highly selective exciton-phonon coupling plays a crucial role in determining the relaxation time of the A exciton. In Fig. 6.2 (c) and (d) we show color maps of exciton-phonon coupling from the starred states in Fig. 6.2 (a) and (b) summed over phonon modes and the four lowest final exciton states. These maps together with Fig. 2 (a) and (b) further demonstrate that the strongest coupling is the intra-exciton band coupling between $\mathbf{Q} = \Gamma$ to $\mathbf{Q} = M$. However, since excitons of the same spin states around $\mathbf{Q} = M$ as the A exciton lay about 70 meV higher in energy, which is larger than the highest phonon energy (60 meV) in MoS_2, they are not able to contribute to the scattering rate. Furthermore, we find that the major contributions come from low-energy LA and TA modes at 300 K. In contrast, the excitons near the band edge with $\mathbf{Q} = M$ are energetically close to the lowest exciton state with $\mathbf{Q} = \Gamma$ so the coupling between these two states dominate the contribution to the large scattering rate seen in Fig. 6.1. In Fig. 6.2 (e) and (f) we show the phonon momentum $\mathbf{q}$-resolved contribution $\Gamma_{\mathbf{q}}$ to the total scattering rates of the starred states in Fig. 6.2 (a) and (b), respectively. We find that indeed for the blue-starred state phonon with momentum close to M contribute most to the scattering rate while phonon with momentum near K and Γ both have smaller contribution. On the other hand the A exciton mostly scatters via phonons with $\mathbf{q} \sim K$ while $\mathbf{q} \sim 0$ and $\mathbf{q} \sim \Lambda_{min}$ also contribute. We note that the ring shape seen in Fig. 6.2 (e) and (f) is due to the mismatch in the velocity of exciton and phonon bands near the band edge, which limits the scattering density of states.

6.3 Exciton Lineshapes Including Off-Diagonal Exciton-Phonon Interactions

Experimentally, exciton-phonon interactions can be accessed by measuring the absorption linewidth and its temperature dependence. The absorption spectrum including exciton-phonon scatterings can be studied within the semiconductor Bloch equation [189, 190, 199, 200] or from the second order perturbation theory [183–185, 201]. A derivation connecting the two approaches is given in Appendix A.3. We summarize the equation of motion of the exciton polarization,

$$\begin{aligned}\frac{dP^S_{\mathbf{0}}(t)}{dt} =& \frac{1}{i\hbar}\sum_{\lambda}\left(E_{S\mathbf{0}}\delta_{S\lambda} - \Sigma_{S\lambda\mathbf{0}}(\omega = E_{\lambda\mathbf{0}})\right)P^{\lambda}_{\mathbf{0}} \\ &- \frac{1}{i\hbar}e\mathbf{E}(t)\cdot\mathbf{\Omega}^S,\end{aligned} \tag{6.2}$$

where $P^S_{\mathbf{0}} \equiv P^S_{\mathbf{Q}=0} = \sum_{cv\mathbf{k}}\psi^{S*}_{c\mathbf{k}v\mathbf{k}}\langle c^{\dagger}_{v\mathbf{k}}c_{c\mathbf{k}}\rangle$ is the exciton polarization with zero COM momentum, $\psi^S_{c\mathbf{k}v\mathbf{k}}$ is the exciton envelope function of a state S, and $c^{\dagger}_{v\mathbf{k}}$ ($c_{c\mathbf{k}}$) is the creation (annihilation) operator for an valence electron v (a conduction electron c) with crystal momentum $\mathbf{k}$. The second term in Eq. 6.2 describes the coupling to an external field $\mathbf{E}(t)$ within the dipole approximation where $\mathbf{\Omega}^S$ is the exciton dipole operator. Finally for the self-energy operator, we employ a matrix generalization of Eq. 6.1,

$$\Sigma_{S\lambda,\mathbf{0}}(\omega) = \frac{1}{N_{\mathbf{q}}} \sum_{n\nu\mathbf{q}} G^{*}_{nS\nu}(0,\mathbf{q}) G_{n\lambda\nu}(0,\mathbf{q}) \\ \times \frac{N_{\nu\mathbf{q}} + \frac{1}{2} \pm \frac{1}{2}}{\omega - E_{n\mathbf{q}} \mp \omega_{\nu\mathbf{q}} + i\gamma}. \tag{6.3}$$

When the off-diagonal elements of Eq. 6.3 are ignored, the computed spectrum is a superposition of Lorentzian functions centered at exciton energies with linewidth equivalent to the relaxation time computed by taking the imaginary part of Eq. 6.1. This approximation (diagonal approximation) is widely used in the literature [19, 75, 188, 194]. The slope of the temperature dependence of the linewidth is often taken as a measure of the exciton-phonon coupling strength. In Fig. 6.5 (a) we plot the temperature dependence of the calculated linewidth using a diagonal approximation as the dashed orange line. Within the diagonal approximation, the linewidth is severely underestimated when compared with the experiment from Ref. [178]. The computed linewidth at 300 K is less than 2 meV which is about 3 times smaller than the experimental value. On the other hand, when the linewidth is evaluated at $\omega = E_\lambda$, the full self-energy expression Eq. 6.3 the results agree very well with the experiment. Not only is the magnitude closer to experiment but the overall temperature dependence also agrees. We emphasize that the same exciton-phonon matrix elements are used in both calculations and only when using the full self-energy matrix are we able to obtain good agreement with the experiment.

The importance of including these off-diagonal terms and their effects on the exciton lineshape has been discussed at length by Toyozawa [184], Hopfield [183], and others over 50 years ago; however, with rare exceptions [202], such terms have not been included in contemporary calculations and never before from first principles. To map to Toyozawa's formalism, we take the external filed to be monochromatic, $\mathbf{E}(t) = \mathbf{E}_0 e^{i\omega t}$, and Fourier transform Eq. 6.2, solve for $\epsilon_2(\omega) = P^{tot}(\omega)/\epsilon_0 E$ and explicitly rewrite the off-diagonal self-energy in terms of the exciton-phonon coupling matrix elements with the aid of Eq. 6.3 to find

$$\varepsilon_2(\omega) \sim \frac{1}{N_{\mathbf{q}}} \sum_{S\mathbf{q}\nu} \left| \hat{\mathbf{e}} \cdot \sum_{S'} \frac{G_{SS'\nu}(0,\mathbf{q}) \mathbf{\Omega}_{S'}}{\omega - \tilde{E}_{S'}} \right|^2 \delta(\omega - E_{S\mathbf{q}} \mp \omega_{\nu\mathbf{q}}), \tag{6.4}$$

where $\hat{\mathbf{e}} = \mathbf{E}_0/|\mathbf{E}_0|$ is the polarization unit vector and $\tilde{E}_S = E_S + \mathrm{Re}\Sigma_S + i\Gamma_S$ with $\mathrm{Re}\Sigma_S$ and $\Gamma_S = \mathrm{Im}\Sigma_S$ denoting the real and imaginary part of the diagonal exciton self-energy defined in Eq. 6.1 respectively. More explicit details connecting Eqs. 6.2 and 6.4 are given in the Appendix for this chapter. An advantage of this expression over the semiconductor Bloch expression is that it is readily interpreted as describing a two step process at second order perturbation theory where a photon is absorbed and a phonon subsequently scatters off the excitation. We depict this process in Fig. 6.3. Expanding the innermost sum on S' in Eq. 6.4 and taking the square modulus, we can regroup the resulting terms based on whether

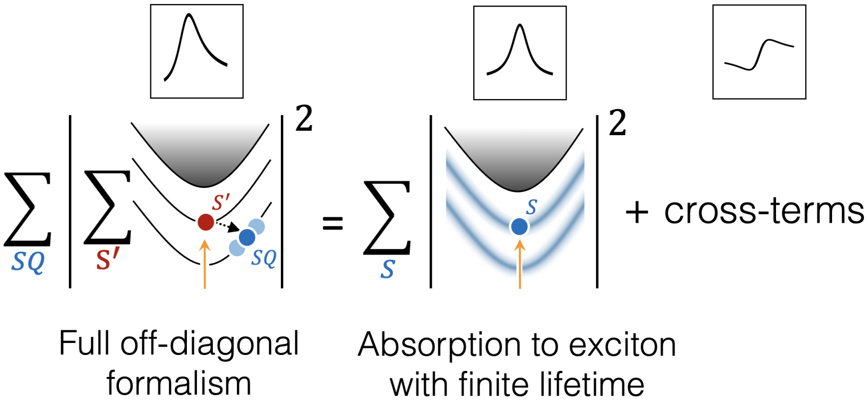

Figure 6.3: Computing $\varepsilon_2(\omega)$ with the off-diagonal exciton self-energy, $\Sigma_{SS'}(\omega)$ captures the all the physics contained in a second order phonon-assisted absorption process, where a photon is first absorbed creating a virtual exciton, S' (red dots), which subsequently scatters off a phonon to some final state S$\mathbf{Q}$ (blue dot), Expanding the innermost sum and subsequently taking the square modulus, two types of terms arise, those diagonal in S' and those not cross-terms. The former gives rise to a symmetric Lorentzian line shape and physically stems from photo-exciting to a finite lifetime quasiparticle band with finite broadening. Cross-terms are frequently not included in *ab initio* calculations but can be important and give rise to all the asymmetry seen in the total line shape.

they are diagonal or off-diagonal in the S' index. Retaining only terms diagonal in S' we arrive at the so-called diagonal approximation for $\varepsilon_2(\omega)$,

$$\begin{aligned}\varepsilon_2^{\text{diag}}(\omega) &\sim \frac{1}{N_{\mathbf{q}}}\sum_{SS'\mathbf{q}\nu}\left|\hat{\mathbf{e}}\cdot\frac{G_{SS'\nu}(0,\mathbf{q})\boldsymbol{\Omega}_{S'}}{\omega-\tilde{E}_{S'}}\right|^2\delta(\omega-E_{S\mathbf{q}}\mp\omega_{\nu\mathbf{q}}),\\ &\approx \sum_{S'}|\hat{\mathbf{e}}\cdot\boldsymbol{\Omega}_{S'}|^2\frac{\Gamma_{S'}}{(\omega-E_{S'}-\text{Re}\Sigma_{S'})^2+\Gamma_{S'}^2},\end{aligned} \tag{6.5}$$

where we identify $\Gamma_S = \text{Im}\Sigma_{SS\mathbf{0}}$ with the diagonal part of the self-energy defined in Eq. 6.1. We see in this diagonal limit we recover the familiar Lorentzian lineshape with a full width at half maximum given by the imaginary part of the diagonal exciton self-energy. This symmetric lineshape is a familiar spectroscopic signature stemming from the process of photo-exciting to a transient excitonic state with some finite lifetime. Cross-terms neglected in passing from Eq. 6.4 to Eq. 6.5 are in some cases very important and give rise to asymmetric contributions to the exciton lineshape as we show below. To summarize the above discussion, in Fig. 6.3 we give a pictorial representation of the relation between the full and diagonal approximations for $\varepsilon_2(\omega)$.

In Fig. 6.4 (a) we show the absorption spectrum computed from Eq. 6.2 at different temperature. At 10 K the A exciton absorption line shows a sharp peak while the B exciton

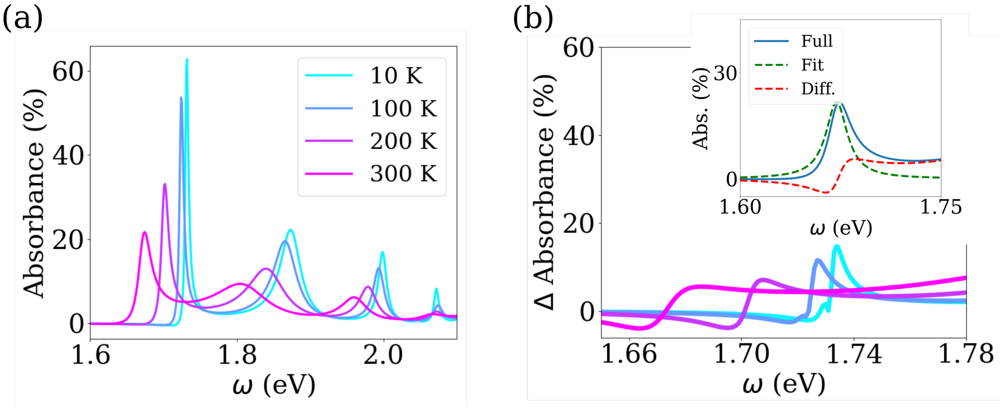

Figure 6.4: (a) Absorption spectrum of in-plane polarized light at various temperature show the asymmetric lineshape. (b) Asymmetry in the A exciton peak in (a) is quantified by subtracting a Lorentzian fit with the computed broadening. The inset in (b) shows the full calculation (blue line), the Lorentzian fit (green dashed line), and the difference (red dashed line).

peak has a larger linewidth, which is similar to the relaxation time comparison shown in Fig. 1. As temperature increases, all peak shift to the low energy side and the spectrum is considerably broadened. We discover that the off-diagonal formula further modify the lineshape considerably. As can be seen in Fig. 6.4 (a) the absorption lines are asymmetric, which is different from a symmetric Lorentzian function usually adopted to describe the experiment data. Hence, the asymmetry in Fig. 6.4 (a) is due to the off-diagonal formula we used. To further quantify the asymmetry we plot in Fig. 6.4 (b) the change in the absorption by subtracting the Lorentzian function computed in the diagonal formula. The asymmetry in lineshape is most pronounced at low temperature and features a larger intensity at higher energy side. It is suppressed at higher temperature but the deviation from a symmetric Lorentizian function remains visible. However, the excited exciton lines are also broadened at higher temperature, which makes it difficult to isolate the asymmetry due to exciton-phonon couplings. It would be interesting to carefully analyze the experiment lineshape for different materials as a further check for the off-diagonal formula.

In Fig. 6.5 (b) we further show the temperature dependence of the shift of the A exciton peak, which represents the renormalization of exciton energy due to exciton-phonon couplings. Again we find surprisingly good agreement between the calculation and the extracted experimental values. The computed energy shift is around 60 meV at 300 K, which is comparable to the band gap renormalization due to electron-phonon couplings [182]. However, when the effects from lattice expansion [203] are included the results deviate from the experiments as shown by the blue line. We expect that the Debye-Waller term which is not considered in this work could partially compensate the lattice thermal expansion [204] effect.

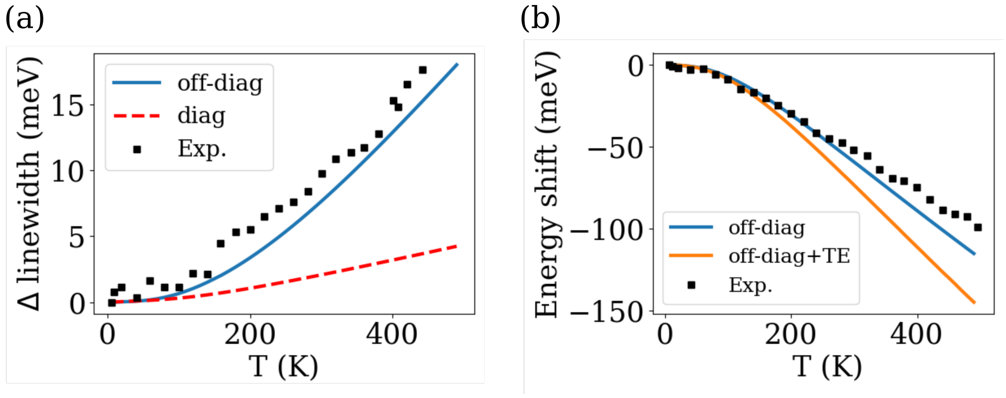

Figure 6.5: ((a) Temperature dependence of the linewidth computed with off-diagonal (blue line) and diagonal only (red dashed line) formula together with the experiment results from Ref. [178]. The computed results are shifted by the experiment low temperature value. (b) Shift of the absorption peak as a function of temperature (blue line) compared with the same experiment results in (a). Energy shift due to lattice thermal expansion (TE) effects are included and shown in the orange line.

6.4 Conclusion

In conclusion, our first-principle calculation of the exciton-phonon coupling strength in a monolayer MoS_2 shows highly selective nature of exciton-phonon couplings due to the internal spin structure of excitons. In particular, we have shown the A exciton has surprisingly long life time about 100 fs at 300 K, which is longer than the first $Q = 0$ dark exciton state at the band edge. Although it has strong couplings with excitons around M in the same band the large difference in energy limits the available scattering phase space. Hence the dominant contribution comes from the relatively weak couplings from K excitons. Moreover, we show that absorption linewidth and peak energy shift computed with the full exciton self-energy matrix agrees much better with the experimental data, which emphasize the importance of the interference effects between inter-exciton band transitions. The theory also leads to an asymmetric lineshape when inter-exciton couplings are strong, an interesting feature worth of further investigation in experiment.

Bibliography

[1] R. D. Mattuck. *A Guide to Feynman Diagrams in the Many-body Problem.* en. Courier Corporation, (1992).

[2] R. S. Knox. *Theory of excitons.* New York: Academic Press, (1963).

[3] M. Born and K. Huang. Dynamical Theory of Crystal Lattices. *Am. J. Phys.* **23**, 474 (1955).

[4] N. F. Mott and M. J. Littleton. Conduction in polar crystals. I. Electrolytic conduction in solid salts. en. *Trans. Faraday Soc.* **34**, 485 (1938).

[5] G. H. Wannier. The Structure of Electronic Excitation Levels in Insulating Crystals. *Phys. Rev.* **52**, 191 (1937).

[6] J. Frenkel. On the Transformation of light into Heat in Solids. I. *Phys. Rev.* **37**, 17 (1931).

[7] S. Manzeli, D. Ovchinnikov, D. Pasquier, O. V. Yazyev, and A. Kis. 2D transition metal dichalcogenides. en. *Nature Reviews Materials* **2**, 1 (2017).

[8] C. J. Bardeen. The Structure and Dynamics of Molecular Excitons. *Annu. Rev. Phys. Chem.* **65**, 127 (2014).

[9] M. Baranowski and P. Plochocka. Excitons in Metal-Halide Perovskites. *Adv. Energ. Mater.* **10**, 1903659 (2020).

[10] G. Onida, L. Reining, and A. Rubio. Electronic excitations: density-functional versus many-body Green's-function approaches. *Rev. Mod. Phys.* **74**, 601 (2002).

[11] M. S. Hybertsen and S. G. Louie. Electron correlation in semiconductors and insulators: Band gaps and quasiparticle energies. en. *Phys. Rev. B Condens. Matter* **34**, 5390 (1986).

[12] M. Rohlfing and S. G. Louie. Electron-hole excitations and optical spectra from first principles. *Phys. Rev. B Condens. Matter* **62**, 4927 (2000).

[13] J. Deslippe, G. Samsonidze, D. A. Strubbe, M. Jain, M. L. Cohen, and S. G. Louie. BerkeleyGW: A massively parallel computer package for the calculation of the quasiparticle and optical properties of materials and nanostructures. *Comput. Phys. Commun.* **183**, 1269 (2012).

[14] M. Ueta, H. Kanzaki, K. Kobayashi, Y. Toyozawa, and E. Hanamura. *Excitonic Processes in Solids*. en. Springer Science & Business Media, (2012).

[15] Y. Toyozawa. *Optical Processes in Solids*. Cambridge University Press, (2003).

[16] S. Poncé, E. R. Margine, C. Verdi, and F. Giustino. EPW: Electron–phonon coupling, transport and superconducting properties using maximally localized Wannier functions. *Comput. Phys. Commun.* **209**, 116 (2016).

[17] S. D. Mahanti and C. M. Varma. Effective Electron-Hole Interactions in Polar Semiconductors. *Phys. Rev. B* **6**, 2209 (1972).

[18] J. Pollmann and H. Büttner. Effective Hamiltonians and bindings energies of Wannier excitons in polar semiconductors. *Phys. Rev. B Condens. Matter* **16**, 4480 (1977).

[19] G. Antonius and S. G. Louie. Theory of exciton-phonon coupling. *Phys. Rev. B Condens. Matter* **105**, 085111 (2022).

[20] N. Marzari, A. A. Mostofi, J. R. Yates, I. Souza, and D. Vanderbilt. Maximally localized Wannier functions: Theory and applications. *Rev. Mod. Phys.* **84**, 1419 (2012).

[21] I. G. Lang and Y. A. Firsov. Kinetic theory of semiconductors with low mobility. *Sov. Phys. JETP* **16**, 1301 (1963).

[22] L. Hedin and S. Lundqvist. "Effects of Electron-Electron and Electron-Phonon Interactions on the One-Electron States of Solids". *Solid State Physics*. Ed. by F. Seitz, D. Turnbull, and H. Ehrenreich. Vol. 23. Academic Press, (1970), pp. 1–181.

[23] C. Verdi and F. Giustino. Fröhlich Electron-Phonon Vertex from First Principles. *Phys. Rev. Lett.* **115**, 176401 (2015).

[24] Y. Toyozawa. Theory of Line-Shapes of the Exciton Absorption Bands. en. *Progr. Theoret. Phys.* **20**, 53 (1958).

[25] J. M. Ziman. "Electrons and Phonons: The Theory of Transport Phenomena in Solids". en. *Electrons and Phonons*. 1st ed. Oxford University Press, (2007).

[26] P. Hohenberg and W. Kohn. Inhomogeneous Electron Gas. *Phys. Rev.* **136**, B864 (1964).

[27] S. Baroni, S. de Gironcoli, A. Dal Corso, and P. Giannozzi. Phonons and related crystal properties from density-functional perturbation theory. *Rev. Mod. Phys.* **73**, 515 (2001).

[28] X. Gonze and C. Lee. Dynamical matrices, Born effective charges, dielectric permittivity tensors, and interatomic force constants from density-functional perturbation theory. *Phys. Rev. B Condens. Matter* **55**, 10355 (1997).

[29] W. Kohn and L. J. Sham. Self-Consistent Equations Including Exchange and Correlation Effects. *Phys. Rev.* **140**, A1133 (1965).

[30] R. G. Parr and Y. Weitao. "Density-Functional Theory of Atoms and Molecules". en. *Density-Functional Theory of Atoms and Molecules*. Oxford University Press, (2020).

[31] E. Engel and R. M. Dreizler. *Density Functional Theory.* Springer Berlin Heidelberg.

[32] D. M. Ceperley and B. J. Alder. Ground State of the Electron Gas by a Stochastic Method. *Phys. Rev. Lett.* **45**, 566 (1980).

[33] W. E. Pickett. Pseudopotential methods in condensed matter applications. *Computer Physics Reports* **9**, 115 (1989).

[34] J. C. Phillips and L. Kleinman. New Method for Calculating Wave Functions in Crystals and Molecules. *Phys. Rev.* **116**, 287 (1959).

[35] D. R. Hamann, M. Schlüter, and C. Chiang. Norm-Conserving Pseudopotentials. *Phys. Rev. Lett.* **43**, 1494 (1979).

[36] R. M. Sternheimer. Electronic Polarizabilities of Ions from the Hartree-Fock Wave Functions. *Phys. Rev.* **96**, 951 (1954).

[37] X. Gonze and J.-P. Vigneron. Density-functional approach to nonlinear-response coefficients of solids. *Phys. Rev. B Condens. Matter* **39**, 13120 (1989).

[38] F. Giustino. Electron-phonon interactions from first principles. *Rev. Mod. Phys.* **89**, 015003 (2017).

[39] J. P. Perdew and M. Levy. Physical Content of the Exact Kohn-Sham Orbital Energies: Band Gaps and Derivative Discontinuities. *Phys. Rev. Lett.* **51**, 1884 (1983).

[40] G. D. Mahan. *Many-Particle Physics.* Springer, Boston, MA, (2000).

[41] A. L. Fetter and J. D. Walecka. *Quantum Theory of Many-Particle Systems.* en. Courier Corporation, (2012).

[42] E. N. Economou. *Green's Functions in Quantum Physics.* Springer Berlin Heidelberg.

[43] L. Hedin. New Method for Calculating the One-Particle Green's Function with Application to the Electron-Gas Problem. *Phys. Rev.* **139**, A796 (1965).

[44] M. E. Peskin and D. V. Schroeder. *An Introduction to quantum field theory.*

[45] C. Itzykson and J. B. Zuber. Quantum field theory (2012).

[46] J. Hubbard. Calculation of Partition Functions. *Phys. Rev. Lett.* **3**, 77 (1959).

[47] J. C. Inkson. "Green's Functions of the Single-Particle Schrödinger Equation". *Many-Body Theory of Solids: An Introduction.* Ed. by J. C. Inkson. Boston, MA: Springer US, (1984), pp. 27–41.

[48] F. Aryasetiawan and O. Gunnarsson. The GW method. en. *Rep. Prog. Phys.* **61**, 237 (1998).

[49] D. Golze, M. Dvorak, and P. Rinke. The GW Compendium: A Practical Guide to Theoretical Photoemission Spectroscopy. en. *Front Chem* **7**, 377 (2019).

[50] S. L. Adler. Quantum Theory of the Dielectric Constant in Real Solids. *Phys. Rev.* **126**, 413 (1962).

[51] N. Wiser. Dielectric Constant with Local Field Effects Included. *Phys. Rev.* **129**, 62 (1963).

[52] R. W. Godby, M. Schlüter, and L. J. Sham. Self-energy operators and exchange-correlation potentials in semiconductors. en. *Phys. Rev. B Condens. Matter* **37**, 10159 (1988).

[53] M. S. Hybertsen and S. G. Louie. Ab initio static dielectric matrices from the density-functional approach. I. Formulation and application to semiconductors and insulators. *Phys. Rev. B Condens. Matter* **35**, 5585 (1987).

[54] G. Strinati. Application of the Green's functions method to the study of the optical properties of semiconductors. *La Rivista del Nuovo Cimento (1978-1999)* **11**, 1 (1988).

[55] D. Y. Qiu, T. Cao, and S. G. Louie. Nonanalyticity, Valley Quantum Phases, and Lightlike Exciton Dispersion in Monolayer Transition Metal Dichalcogenides: Theory and First-Principles Calculations. en. *Phys. Rev. Lett.* **115**, 176801 (2015).

[56] N. Marzari and D. Vanderbilt. Maximally localized generalized Wannier functions for composite energy bands. *Phys. Rev. B Condens. Matter* **56**, 12847 (1997).

[57] A. J. Williamson, R. Q. Hood, and J. C. Grossman. Linear-scaling quantum Monte Carlo calculations. en. *Phys. Rev. Lett.* **87**, 246406 (2001).

[58] X. Wang, J. R. Yates, I. Souza, and D. Vanderbilt. Ab initio calculation of the anomalous Hall conductivity by Wannier interpolation. *Phys. Rev. B Condens. Matter* **74**, 195118 (2006).

[59] J. Ibañez-Azpiroz, S. S. Tsirkin, and I. Souza. Ab initio calculation of the shift photocurrent by Wannier interpolation. *Phys. Rev. B Condens. Matter* **97**, 245143 (2018).

[60] S. S. Tsirkin, P. A. Puente, and I. Souza. Gyrotropic effects in trigonal tellurium studied from first principles. *Phys. Rev. B Condens. Matter* **97**, 035158 (2018).

[61] R. D. King-Smith and D. Vanderbilt. Theory of polarization of crystalline solids. *Phys. Rev. B Condens. Matter* **47**, 1651 (1993).

[62] F. Giustino, M. L. Cohen, and S. G. Louie. Electron-phonon interaction using Wannier functions. *Phys. Rev. B Condens. Matter* **76**, 165108 (2007).

[63] J. Noffsinger, F. Giustino, B. D. Malone, C.-H. Park, S. G. Louie, and M. L. Cohen. EPW: A program for calculating the electron–phonon coupling using maximally localized Wannier functions. *Comput. Phys. Commun.* **181**, 2140 (2010).

[64] I. Souza, N. Marzari, and D. Vanderbilt. Maximally localized Wannier functions for entangled energy bands. *Phys. Rev. B Condens. Matter* **65**, 035109 (2001).

[65] J.-M. Lihm and C.-H. Park. Wannier Function Perturbation Theory: Localized Representation and Interpolation of Wave Function Perturbation. *Phys. Rev. X* **11**, 041053 (2021).

[66] D. Y. Qiu, F. H. da Jornada, and S. G. Louie. Optical Spectrum of MoS_2: Many-Body Effects and Diversity of Exciton States. *Phys. Rev. Lett.* **111**, 216805 (2013).

[67] X. Zhu, H. Su, R. A. Marcus, and M. E. Michel-Beyerle. Computed and Experimental Absorption Spectra of the Perovskite CH3NH3PbI3. en. *J. Phys. Chem. Lett.* **5**, 3061 (2014).

[68] A. Molina-Sánchez. Excitonic States in Semiconducting Two-Dimensional Perovskites. *ACS Appl. Energy Mater.* **1**, 6361 (2018).

[69] R. I. Biega, M. R. Filip, L. Leppert, *et al.* Chemically Localized Resonant Excitons in Silver–Pnictogen Halide Double Perovskites. *The journal of physical* (2021).

[70] M. L. Tiago, J. E. Northrup, and S. G. Louie. Ab initio calculation of the electronic and optical properties of solid pentacene. *Phys. Rev. B Condens. Matter* **67**, 115212 (2003).

[71] S. Sharifzadeh, A. Biller, L. Kronik, and J. B. Neaton. Quasiparticle and optical spectroscopy of the organic semiconductors pentacene and PTCDA from first principles. *Phys. Rev. B Condens. Matter* **85**, 125307 (2012).

[72] S. Sharifzadeh, P. Darancet, L. Kronik, and J. B. Neaton. Low-Energy Charge-Transfer Excitons in Organic Solids from First-Principles: The Case of Pentacene. *J. Phys. Chem. Lett.* **4**, 2197 (2013).

[73] T. Rangel, K. Berland, S. Sharifzadeh, F. Brown-Altvater, K. Lee, P. Hyldgaard, L. Kronik, and J. B. Neaton. Structural and excited-state properties of oligoacene crystals from first principles. *Phys. Rev. B Condens. Matter* **93**, 115206 (2016).

[74] D. Y. Qiu, G. Cohen, D. Novichkova, and S. Refaely-Abramson. Signatures of Dimensionality and Symmetry in Exciton Band Structure: Consequences for Exciton Dynamics and Transport. en. *Nano Lett.* **21**, 7644 (2021).

[75] H.-Y. Chen, D. Sangalli, and M. Bernardi. Exciton-Phonon Interaction and Relaxation Times from First Principles. *Phys. Rev. Lett.* **125**, 107401 (2020).

[76] V. K. Kozin, V. A. Shabashov, A. V. Kavokin, and I. A. Shelykh. Anomalous Exciton Hall Effect. en. *Phys. Rev. Lett.* **126**, 036801 (2021).

[77] M. Onga, Y. Zhang, T. Ideue, and Y. Iwasa. Exciton Hall effect in monolayer MoS2. en. *Nat. Mater.* **16**, 1193 (2017).

[78] S.-I. Kuga, S. Murakami, and N. Nagaosa. Spin Hall effect of excitons. *Phys. Rev. B Condens. Matter* **78**, 205201 (2008).

[79] W. Yao and Q. Niu. Berry phase effect on the exciton transport and on the exciton Bose-Einstein condensate. en. *Phys. Rev. Lett.* **101**, 106401 (2008).

[80] W. R. Heller and A. Marcus. A note on the propagation of excitation in an idealized crystal. *Phys. Rev.* **84**, 809 (1951).

[81] J. J. Hopfield and D. G. Thomas. On some observable properties of longitudinal excitons. *J. Phys. Chem. Solids* **12**, 276 (1960).

[82] X. Wang and T. C. Berkelbach. Excitons in Solids from Periodic Equation-of-Motion Coupled-Cluster Theory. en. *J. Chem. Theory Comput.* **16**, 3095 (2020).

[83] A. A. Mostofi, J. R. Yates, G. Pizzi, Y.-S. Lee, I. Souza, D. Vanderbilt, and N. Marzari. An updated version of wannier90: A tool for obtaining maximally-localised Wannier functions. *Comput. Phys. Commun.* **185**, 2309 (2014).

[84] G. Pizzi *et al.* Wannier90 as a community code: new features and applications. en. *J. Phys. Condens. Matter* **32**, 165902 (2020).

[85] D. M. Roessler and W. C. Walker. Electronic spectrum of crystalline lithium fluoride. *J. Phys. Chem. Solids* **28**, 1507 (1967).

[86] P. Giannozzi *et al.* Advanced capabilities for materials modelling with Quantum ESPRESSO. en. *J. Phys. Condens. Matter* **29**, 465901 (2017).

[87] J. P. Perdew, K. Burke, and M. Ernzerhof. Generalized Gradient Approximation Made Simple. en. *Phys. Rev. Lett.* **77**, 3865 (1996).

[88] D. R. Hamann. Optimized norm-conserving Vanderbilt pseudopotentials. *Phys. Rev. B Condens. Matter* **88**, 085117 (2013).

[89] M. J. van Setten, M. Giantomassi, E. Bousquet, M. J. Verstraete, D. R. Hamann, X. Gonze, and G.-M. Rignanese. The PseudoDojo: Training and grading a 85 element optimized norm-conserving pseudopotential table. *Comput. Phys. Commun.* **226**, 39 (2018).

[90] Y. Onodera and Y. Toyozawa. Excitons in Alkali Halides. *J. Phys. Soc. Jpn.* **22**, 833 (1967).

[91] W. Kohn. Analytic Properties of Bloch Waves and Wannier Functions. *Phys. Rev.* **115**, 809 (1959).

[92] J. D. Cloizeaux. Energy Bands and Projection Operators in a Crystal: Analytic and Asymptotic Properties. *Phys. Rev.* **135**, A685 (1964).

[93] G. Panati. Triviality of Bloch and Bloch–Dirac Bundles. *Annales Henri Poincaré* **8**, 995 (2007).

[94] C. Brouder, G. Panati, M. Calandra, C. Mourougane, and N. Marzari. Exponential localization of Wannier functions in insulators. en. *Phys. Rev. Lett.* **98**, 046402 (2007).

[95] X. Gonze, J.-C. Charlier, D. C. Allan, and M. P. Teter. Interatomic force constants from first principles: The case of α-quartz. *Phys. Rev. B Condens. Matter* **50**, 13035 (1994).

[96] S. Matthew Menke and R. J. Holmes. Exciton diffusion in organic photovoltaic cells. en. *Energy Environ. Sci.* **7**, 499 (2014).

[97] A. Chenu and G. D. Scholes. Coherence in energy transfer and photosynthesis. en. *Annu. Rev. Phys. Chem.* **66**, 69 (2015).

[98] N. S. Ginsberg and W. A. Tisdale. Spatially Resolved Photogenerated Exciton and Charge Transport in Emerging Semiconductors. *Annu. Rev. Phys. Chem.* **71**, 1 (2020).

[99] T. Holstein. Studies of polaron motion: Part I. The molecular-crystal model. *Ann. Phys.* **8**, 325 (1959).

[100] J. Bardeen. Conductivity of Monovalent Metals. *Phys. Rev.* **52**, 688 (1937).

[101] R. Silbey and R. W. Munn. General theory of electronic transport in molecular crystals. I. Local linear electron–phonon coupling. *J. Chem. Phys.* **72**, 2763 (1980).

[102] R. W. Munn and R. Silbey. Theory of electronic transport in molecular crystals. III. Diffusion coefficient incorporating nonlocal linear electron–phonon coupling. *J. Chem. Phys.* **83**, 1854 (1985).

[103] A. Troisi and G. Orlandi. Charge-transport regime of crystalline organic semiconductors: diffusion limited by thermal off-diagonal electronic disorder. en. *Phys. Rev. Lett.* **96**, 086601 (2006).

[104] S. Fratini, D. Mayou, and S. Ciuchi. The transient localization scenario for charge transport in crystalline organic materials. en. *Adv. Funct. Mater.* **26**, 2292 (2016).

[105] F. Brown-Altvater, T. Rangel, and J. B. Neaton. Ab initio phonon dispersion in crystalline naphthalene using van der Waals density functionals. *Phys. Rev. B: Condens. Matter Mater. Phys.* (2016).

[106] V. Stehr, B. Engels, C. Deibel, and R. F. Fink. Anisotropy of singlet exciton diffusion in organic semiconductor crystals from ab initio approaches. en. *J. Chem. Phys.* **140**, 024503 (2014).

[107] V. Stehr, R. F. Fink, B. Engels, J. Pflaum, and C. Deibel. Singlet Exciton Diffusion in Organic Crystals Based on Marcus Transfer Rates. en. *J. Chem. Theory Comput.* **10**, 1242 (2014).

[108] Y. Si, B. Yang, H. Qin, J. Yuan, S. Wang, H. Chen, and Y. Zhao. Atomistic Modeling of Triplet–Triplet Energy-Transfer Rates from Drug (S)-Propranolol to (R)-Cinacalcet in Human α1-Acid Glycoprotein. *J. Phys. Chem. C* **119**, 8014 (2015).

[109] L. Sudha Devi, M. K. Al-Suti, C. Dosche, M. S. Khan, R. H. Friend, and A. Köhler. Triplet energy transfer in conjugated polymers. I. Experimental investigation of a weakly disordered compound. *Phys. Rev. B Condens. Matter* **78**, 045210 (2008).

[110] N.-E. Lee, J.-J. Zhou, L. A. Agapito, and M. Bernardi. Charge transport in organic molecular semiconductors from first principles: The bandlike hole mobility in a naphthalene crystal. *Phys. Rev. B Condens. Matter* **97**, 115203 (2018).

[111] F. Brown-Altvater, G. Antonius, T. Rangel, M. Giantomassi, *et al.* Band gap renormalization, carrier mobilities, and the electron-phonon self-energy in crystalline naphthalene. *Phys. Rev. B: Condens. Matter Mater. Phys.* (2020).

[112] W. P. Su, J. R. Schrieffer, and A. J. Heeger. Solitons in Polyacetylene. *Phys. Rev. Lett.* **42**, 1698 (1979).

[113] J. Aragó and A. Troisi. Regimes of exciton transport in molecular crystals in the presence of dynamic disorder. en. *Adv. Funct. Mater.* **26**, 2316 (2016).

[114] Y. Jiang, Z. Shuai, and M. Liu. Roles of Long-Range Hopping, Quantum Nuclear Effect, and Exciton Delocalization in Exciton Transport in Organic Semiconductors: A Multiscale Study. *J. Phys. Chem. C* **122**, 18365 (2018).

[115] Z. Li, X. Zhang, and G. Lu. Exciton diffusion in disordered small molecules for organic photovoltaics: insights from first-principles simulations. en. *J. Phys. Condens. Matter* **26**, 185006 (2014).

[116] X. Zhang, Z. Li, and G. Lu. First-principles simulations of exciton diffusion in organic semiconductors. *Phys. Rev. B Condens. Matter* **84**, 235208 (2011).

[117] A. M. Alvertis and E. A. Engel. Importance of vibrational anharmonicity for electron-phonon coupling in molecular crystals. *Phys. Rev. B Condens. Matter* **105**, L180301 (2022).

[118] R. A. Marcus. Electron transfer reactions in chemistry. Theory and experiment. *Rev. Mod. Phys.* **65**, 599 (1993).

[119] D. G. Bossanyi *et al.* Emissive spin-0 triplet-pairs are a direct product of triplet-triplet annihilation in pentacene single crystals and anthradithiophene films. en. *Nat. Chem.* **13**, 163 (2021).

[120] T. D. Lee, F. E. Low, and D. Pines. The Motion of Slow Electrons in a Polar Crystal. *Phys. Rev.* **90**, 297 (1953).

[121] W. H. Sio, C. Verdi, S. Poncé, and F. Giustino. Polarons from First Principles, without Supercells. *Phys. Rev. Lett.* **122**, 246403 (2019).

[122] W. H. Sio, C. Verdi, S. Poncé, and F. Giustino. Ab initio theory of polarons: Formalism and applications. *Phys. Rev. B Condens. Matter* **99**, 235139 (2019).

[123] T. Förster. Zwischenmolekulare energiewanderung und fluoreszenz. en. *Ann. Phys.* **437**, 55 (1948).

[124] D. L. Dexter. A Theory of Sensitized Luminescence in Solids. *J. Chem. Phys.* **21**, 836 (1953).

[125] M. R. Filip, J. B. Haber, and J. B. Neaton. Phonon Screening of Excitons in Semiconductors: Halide Perovskites and Beyond. en. *Phys. Rev. Lett.* **127**, 067401 (2021).

[126] K. Takanabe. Photocatalytic water splitting: quantitative approaches toward photocatalyst by design. *ACS Catalysis* **7**, 8006 (2017).

[127] L. M. Herz. How Lattice Dynamics Moderate the Electronic Properties of Metal-Halide Perovskites. *J. Phys. Chem. Lett.* **9**, 6853 (2018).

[128] X. Ai, E. W. Evans, S. Dong, A. J. Gillett, H. Guo, Y. Chen, T. J. H. Hele, R. H. Friend, and F. Li. Efficient radical-based light-emitting diodes with doublet emission. *Nature* **563**, 536 (2018).

[129] R. J. Elliot. Intensity of the Optical Absorption by Excitons. *Phys. Rev.* **108**, 1384 (1957).

[130] A. Miyata, A. Mitioglu, P. Plochocka, O. Portugall, J. T.-W. Wang, S. D. Stranks, and H. J. Snaith. Direct Measurement of the Exciton Binding Energy and Effective Masses for Charge Carriers in Organic-Inorganic Tri-Halide Perovskites. *Nat. Phys.* **11**, 582 (2015).

[131] P. C. Makado and N. C. McGill. Energy levels of a neutral hydrogen-like system in a constant magnetic field of arbitary strength. *J. Phys. Chem. C: Solid State Physics* **19** (1986).

[132] S. D. Mahanti and C. M. Varma. Effective Electron and Hole Interactions in a Polarizable Field. *Phys. Rev. Lett.* **25**, 1115 (1970).

[133] S. Albrecht, L. Reining, R. Del Sole, and G. Onida. Ab initio calculation of excitonic effects in the optical spectra of semiconductors. *Phys. Rev. Lett.* **80**, 4510 (1998).

[134] B. Malone and M. L. Cohen. Quasiparticle semiconductor band structures including spin-orbit interactions. *J. Phys. Condens. Matter.* **25**, 105503 (2013).

[135] M. R. Filip and F. Giustino. *GW* Quasiparticle Band Gap of the Hybrid Organic-Inorganic Perovskite $CH_3NH_3PbI_3$: Effect of Spin-Orbit Interaction, Semicore Electrons, and Self-Consistency. *Phys. Rev. B* **90** (2014).

[136] D. Y. Qiu, F. H. da Jornada, and S. G. Louie. Optical Spectrum of MoS2: Many-Body Effects and Diversity of Exciton States. *Phys. Rev. Lett.* **111**, 216805 (2013).

[137] S. Refaely-Abramson, D. Y. Qiu, S. G. Louie, and J. B. Neaton. Defect-induced modification of low-lying excitons and valley selectivity in monolayer transition metal dichalcogenides. *Phys. Rev. Lett.* **121**, 167402 (2018).

[138] F. Giustino, S. G. Louie, and M. L. Cohen. Electron-Phonon Renormalization of the Direct Band Gap of Diamond. *Phys. Rev. Lett.*, 265501 (2010).

[139] G. Antonius, S. Poncé, P. Boulanger, M. Cotê, and X. Gonze. Many-Body Effects on the Zero-Point Renormalization of the Band Structure. *Phys. Rev. Lett.*, 215501 (2014).

[140] J. Noffsinger, E. Kioupakis, C. Van de Walle, S. G. Louie, and M. L. Cohen. Phonon-assisted optical absorption in silicon from first principles. *Phys. Rev. Lett.* **16**, 167402 (2012).

[141] M. Zacharias, C. E. Patrick, and F. Giustino. Stochastic approach to phonon-assisted optical absorption. *Phys. Rev. Lett.* **115**, 177401 (2015).

[142] A. Marini. Ab-Initio Finite-Temperature Excitons. *Phys. Rev. Lett.* **101**, 106405 (2008).

[143] F. Bechstedt, K. Seino, P. H. Hahn, and W. G. Schmidt. Quasiparticle bands and optical spectra of highly ionic crystals: AlN and NaCl. *Phys. Rev. B* **72**, 245114 (2005).

[144] A. Schleife, M. D. Neumann, N. Esser, Z. Galazka, A. Gottwald, J. Nixdorf, R. Goldhahn, and M. Feneberg. Optical properties of In_2O_3 from experimentand first-principles theory: influence of lattice screening. *New J. Phys.* **20**, 053016 (2018).

[145] F. Bechstedt and J. Forthmüller. Influence of screening dynamics on excitons in Ga2O3 polymorphs. *Appl. Phys. Lett.* **114**, 122101 (2019).

[146] M. Bokdam, T. Sander, A. Stroppa, S. Picozzi, D. D. Sarma, C. Franchini, and G. Kresse. Role of Polar Phonons into the Photo-Excited State of Metal Halide Perovskites. *Sci. Rep.* **6** (2016).

[147] P. Umari, E. Mosconi, and F. De Angelis. Infrared Dielectric Screening Determines the Low Exciton Binding Energy of Metal-Halide Perovskites. *J. Phys. Chem. Lett.* **9**, 620 (2018).

[148] J. Pollmann and H. Büttner. Effective Hamiltonians and Binding Energies of Wannier Excitons in Polar Semiconductors. *16*, 4480 (1977).

[149] E. O. Kane. Pollman-Büttner variational method for excitonic polarons. *Phys. Rev. B* **18**, 6849 (1978).

[150] M. Matsuura and H. Büttner. Optical Properties of Excitons in Polar Semiconductors: Energies, Oscillator Strengths,and Phonon Sidebands. *Phys. Rev. B* **21**, 679 (1980).

[151] S. Poncé, E. R. Margine, C. Verdi, and F. Giustino. EPW: Electron–phonon coupling, transport and superconducting properties using maximally localized Wannier functions. *Comp. Phys. Commun.* **209**, 116 (2016).

[152] M. Rohlfing and S. G. Louie. Electron-Hole Excitations in Semiconductors and Insulators. *Phys. Rev. Lett.* **81**, 2312 (1998).

[153] P. Hohenberg and W. Kohn. Inhomogeneous Electron Gas. *Phys. Rev.* **136**, B864 (1964).

[154] M. R. Linaburg, E. T. McClure, J. D. Majher, and P. M. Woodward. $Cs_{1-x}Rb_xPbCl_3$ and $Cs_{1-x}Rb_xPbBr_3$ Solid Solutions: Understanding Octahedral Tilting in Lead Halide Perovskites. *Chem. Mater.* **29**, 3507 (2017).

[155] R. J. Sutton, M. R. Filip, A. A. Haghighirad, N. Sakai, W. Bernard, F. Giustino, and H. J. Snaith. Cubic or Orthorhombic? Revealing the Crystal Structure of Metastable Black-Phase $CsPbI_3$ by Theory and Experiment. *ACS Energ. Lett.* **3**, 1787 (2018).

[156] J. P. Perdew and A. Zunger. Self-interaction correction to density-functional approximations for many-electrons systems. *Phys. Rev. B* **23**, 5048 (1981).

[157] P. Gianozzi *et al.* QUANTUM ESPRESSO: a modular and open-source software project for quantum simulations of materials. *J. Phys.: Condens. Matter.* **21** (2009).

[158] M. J. van Setten, M. Giantomassi, E. Bousquet, M. J. Verstraete, D. R. Hammann, X. Gonze, and G.-M. Rignanese. Training and grading a 85 element optimized norm-conserving pseudopotential table. *Comp. Phys. Commun.* **226**, 39 (2018).

[159] M. R. Filip, G. E. Eperon, H. J. Snaith, and F. Giustino. Steric engineering of metal-halide perovskites with tunable band gaps. *Nat. Commun.* **5** (2014).

[160] J. Deslippe, G. Samsonidze, M. Jain, M. L. Cohen, and S. G. Louie. Coulomb-hole summations and energies for GW calculations with limited number of empty orbitals: A modified static remainder approach. *Phys. Rev. B* **87**, 165124 (2013).

[161] M. R. Filip, C. Verdi, and F. Giustino. *GW* Band Structures and Carrier Effective Masses of $CH_3NH_3PbI_3$ and Hypothetical Perovskites of the Type $APbI_3$: A = NH_4, PH_4, AsH_4 and SbH_4. *J. Phys. Chem. C* **119**, 25209 (2015).

[162] C. L. Davies, M. R. Filip, J. B. Patel, T. W. Crothers, C. Verdi, A. D. Wright, R. L. Milot, F. Giustino, M. B. Johnston, and L. M. Herz. Bimolecular Recombination in Methylammonium Lead Triiodide Perovskite is an Inverse Absorption Process. *Nat. Commun.* **9** (2018).

[163] F. Brivio, K. T. Butler, A. Walsh, and M. van Schilfgaarde. Relativistic quasiparticle self-consistent electronic structure of hybrid halide perovskite photovoltaic absorbers. *Phys. Rev. B* **89**, 155204 (2014).

[164] L. Leppert, T. Rangel, and J. B. Neaton. Towards predictive band gaps for halide perovskites: Lessons from one-shot and eigenvalue self-consistent GW. *Phys. Rev. Mater.* **3**, 103803 (2019).

[165] J. Wiktor, U. Rothlisberger, and A. Pasquarello. Predictive Determination of Band Gaps of Inorganic Halide Perovskites. *J. Phys. Chem. Lett.* **8**, 5507 (2017).

[166] Z. Yang *et al. ACS Energ. Lett.* **2**, 1621 (2017).

[167] K. Heindrich, H. Künzel, and J. Treusch. Optical properties and electronic structure of CsPbCl3 AND CsPbBr3. *Solid State Commun.* **25**, 887 (1978).

[168] Q. Zhang, R. Su, X. Liu, T. C. Sum, and Q. Xiong. High-quality whispering-gallery-mode lasing from cesium lead halide perovskite nanoplatelets. *Adv. Func. mater* **26**, 6238 (2016).

[169] M. Baranowski, P. Plochocka, R. Su, L. Legrand, T. Barisien, F. Bernardot, Q. Xiong, C. Testelin, and M. Chamarro. Exciton binding energy and effective mass of CsPbCl3: a magneto-optical study. *Photon. Res.* **8**, A50 (2020).

[170] M. Schlipf, S. Ponce, and F. Giustino. Carrier Lifetimes and Polaronic Mass Enhancement in the Hybrid Halide Perovskite $CH_3NH_3PbI_3$ from Multiphonon Fröhlich Coupling. *Phys. Rev. Lett.* **121**, 086402 (2018).

[171] J. Laflamme Janssen, M. Côté, S. G. Louie, and M. L. Cohen. Electron-phonon coupling in C60 using hybrid functionals. *Phys. Rev. B* **81**, 073106 (2010).

[172] Many-Body Effects on the Zero-Point Renormalization of the Band Structure. *Phys. Rev. Lett.* **112**, 215501 (2011).

[173] S. Gao, Y. Liang, C. D. Spataru, and L. Yang. Dynamical Excitonic Effects in Doped Two-Dimensional Semiconductors. en. *Nano Lett.* **16**, 5568 (2016).

[174] D. Y. Qiu, F. H. da Jornada, and S. G. Louie. Screening and many-body effects in two-dimensional crystals: Monolayer MoS_2. *Phys. Rev. B* **93**, 235435 (2016).

[175] A. Chernikov, T. C. Berkelbach, H. M. Hill, A. Rigosi, Y. Li, O. B. Aslan, D. R. Reichman, M. S. Hybertsen, and T. F. Heinz. Exciton Binding Energy and Nonhydrogenic Rydberg Series in Monolayer WS_2. *Phys. Rev. Lett.* **113**, 076802 (2014).

[176] G. Wang, A. Chernikov, M. M. Glazov, T. F. Heinz, X. Marie, T. Amand, and B. Urbaszek. Colloquium: Excitons in atomically thin transition metal dichalcogenides. *Rev. Mod. Phys.* **90**, 021001 (2018).

[177] G. Moody *et al.* Intrinsic homogeneous linewidth and broadening mechanisms of excitons in monolayer transition metal dichalcogenides. *Nature Communications* **6**, 8315 (2015).

[178] P. Dey, J. Paul, Z. Wang, C. E. Stevens, C. Liu, A. H. Romero, J. Shan, D. J. Hilton, and D. Karaiskaj. Optical Coherence in Atomic-Monolayer Transition-Metal Dichalcogenides Limited by Electron-Phonon Interactions. *Phys. Rev. Lett.* **116**, 127402 (2016).

[179] F. Cadiz *et al.* Excitonic Linewidth Approaching the Homogeneous Limit in MoS_2-Based van der Waals Heterostructures. *Phys. Rev. X* **7**, 021026 (2017).

[180] P. Giannozzi, S. de Gironcoli, P. Pavone, and S. Baroni. Ab initio calculation of phonon dispersions in semiconductors. *Phys. Rev. B* **43**, 7231 (1991).

[181] A. Marini. Ab Initio Finite-Temperature Excitons. *Phys. Rev. Lett.* **101**, 106405 (2008).

[182] A. Molina-Sánchez, M. Palummo, A. Marini, and L. Wirtz. Temperature-dependent excitonic effects in the optical properties of single-layer MoS_2. *Phys. Rev. B* **93**, 155435 (2016).

[183] J. Hopfield. On the energy dependence of the absorption constant and photoconductivity near a direct band gap. *Journal of Physics and Chemistry of Solids* **22**, 63 (1961).

[184] Y. Toyozawa. Interband effect of lattice vibrations in the exciton absorption spectra. *Journal of Physics and Chemistry of Solids* **25**, 59 (1964).

[185] B. Segall and G. D. Mahan. Phonon-Assisted Recombination of Free Excitons in Compound Semiconductors. *Phys. Rev.* **171**, 935 (1968).

[186] J. Jiang, R. Saito, K. Sato, J. S. Park, G. G. Samsonidze, A. Jorio, G. Dresselhaus, and M. S. Dresselhaus. Exciton-photon, exciton-phonon matrix elements, and resonant Raman intensity of single-wall carbon nanotubes. *Phys. Rev. B* **75**, 035405 (2007).

[187] S. Shree *et al.* Observation of exciton-phonon coupling in $MoSe_2$ monolayers. *Phys. Rev. B* **98**, 035302 (2018).

[188] E. Cannuccia, B. Monserrat, and C. Attaccalite. Theory of phonon-assisted luminescence in solids: Application to hexagonal boron nitride. *Phys. Rev. B* **99**, 081109 (2019).

[189] M. Selig, G. Berghäuser, A. Raja, P. Nagler, C. Schüller, T. F. Heinz, T. Korn, A. Chernikov, E. Malic, and A. Knorr. Excitonic linewidth and coherence lifetime in monolayer transition metal dichalcogenides. *Nature Communications* **7**, 13279 (2016).

[190] D. Christiansen *et al.* Phonon Sidebands in Monolayer Transition Metal Dichalcogenides. *Phys. Rev. Lett.* **119**, 187402 (2017).

[191] S. Brem, M. Selig, G. Berghaeuser, and E. Malic. Exciton Relaxation Cascade in two-dimensional Transition Metal Dichalcogenides. *Scientific Reports* **8**, 8238 (2018).

[192] S. Brem, J. Zipfel, M. Selig, A. Raja, L. Waldecker, J. D. Ziegler, T. Taniguchi, K. Watanabe, A. Chernikov, and E. Malic. Intrinsic lifetime of higher excitonic states in tungsten diselenide monolayers. *Nanoscale* **11**, 12381 (2019).

[193] T. A. Huang, M. Zacharias, D. K. Lewis, F. Giustino, and S. Sharifzadeh. Exciton–Phonon Interactions in Monolayer Germanium Selenide from First Principles. *The Journal of Physical Chemistry Letters* **12**, 3802 (2021).

[194] S. Reichardt and L. Wirtz. Nonadiabatic exciton-phonon coupling in Raman spectroscopy of layered materials. *Science Advances* **6** (2020). eprint: `https://advances.sciencemag.org/content/6/32/eabb5915.full.pdf`.

[195] X. Li, J. T. Mullen, Z. Jin, K. M. Borysenko, M. Buongiorno Nardelli, and K. W. Kim. Intrinsic electrical transport properties of monolayer silicene and MoS_2 from first principles. *Phys. Rev. B* **87**, 115418 (2013).

[196] F. Guo, Z. Liu, M. Zhu, and Y. Zheng. Electron–phonon scattering limited hole mobility at room temperature in a MoS2 monolayer: first-principles calculations. *Phys. Chem. Chem. Phys.* **21**, 22879 (2019).

[197] M. Schlipf and F. Gygi. Optimization algorithm for the generation of ONCV pseudopotentials. *Computer Physics Communications* **196**, 36 (2015).

[198] F. da Jornada, D. Qiu, and S. G. Louie. Nonuniform sampling schemes of the Brillouin zone for many-electron perturbation-theory calculations in reduced dimensionality. *Phys. Rev. B* **95**, 035109 (2017).

[199] A. Thränhardt, S. Kuckenburg, A. Knorr, T. Meier, and S. W. Koch. Quantum theory of phonon-assisted exciton formation and luminescence in semiconductor quantum wells. *Phys. Rev. B* **62**, 2706 (2000).

[200] F. Rossi and T. Kuhn. Theory of ultrafast phenomena in photoexcited semiconductors. *Rev. Mod. Phys.* **74**, 895 (2002).

[201] V. Perebeinos, J. Tersoff, and P. Avouris. Effect of Exciton-Phonon Coupling in the Calculated Optical Absorption of Carbon Nanotubes. *Phys. Rev. Lett.* **94**, 027402 (2005).

[202] F. Schweiner, J. Main, and G. Wunner. Linewidths in excitonic absorption spectra of cuprous oxide. *Phys. Rev. B* **93**, 085203 (2016).

[203] L. F. Huang, P. L. Gong, and Z. Zeng. Correlation between structure, phonon spectra, thermal expansion, and thermomechanics of single-layer MoS_2. *Phys. Rev. B* **90**, 045409 (2014).

[204] G. Antonius, S. Poncé, E. Lantagne-Hurtubise, G. Auclair, X. Gonze, and M. Côté. Dynamical and anharmonic effects on the electron-phonon coupling and the zero-point renormalization of the electronic structure. *Phys. Rev. B* **92**, 085137 (2015).

Appendix A

Definitions and Deviations

A.1 Wannier Exciton Overlaps and Projection Matrices

In the electron, $\mathbf{r}_e$, and hole, $\mathbf{r}_h$ coordinates, the exciton wavefunction, $\Psi_{S\mathbf{Q}}(\mathbf{R}, \mathbf{r})$ is expressed as

$$\Psi_{S\mathbf{Q}}(\mathbf{r}_e, \mathbf{r}_h) = \sum_{cv\mathbf{k}} A^{S\mathbf{Q}}_{cv\mathbf{k}}\ \psi_{c\mathbf{k}+\mathbf{Q}/2}(\mathbf{r}_e)\ \psi^{\star}_{v\mathbf{k}-\mathbf{Q}/2}(\mathbf{r}_h).$$

Introducing average and relative coordinates,

$$\begin{aligned} \mathbf{r}_e &= \mathbf{R} + \mathbf{r}/2 \\ \mathbf{r}_h &= \mathbf{R} - \mathbf{r}/2 \end{aligned}$$

wehave

$$\Psi^{S\mathbf{Q}}(\mathbf{R}, \mathbf{r}) = e^{i\mathbf{Q}\cdot\mathbf{R}} \sum_{cv\mathbf{k}} A^{S\mathbf{Q}}_{cv\mathbf{k}+\mathbf{Q}/2} e^{i\mathbf{k}\cdot\mathbf{r}} u_{c\mathbf{k}+\mathbf{Q}/2}(\mathbf{R} + \mathbf{r}/2) u^{\star}_{v\mathbf{k}-\mathbf{Q}/2}(\mathbf{R} - \mathbf{r}/2).$$

The cell-periodic part of the exciton wavefunction, $F_{S\mathbf{Q}}(\mathbf{R}, \mathbf{r})$ is readily read off as

$$F_{S\mathbf{Q}}(\mathbf{R}, \mathbf{r}) = \sum_{cv\mathbf{k}} A^{S\mathbf{Q}}_{cv\mathbf{k}} e^{i\mathbf{k}\cdot\mathbf{r}} u_{c\mathbf{k}+\mathbf{Q}/2}(\mathbf{R} + \mathbf{r}/2) u^{\star}_{v\mathbf{k}-\mathbf{Q}/2}(\mathbf{R} - \mathbf{r}/2). \tag{A.1}$$

To run Wannier90, we must provide the code with overlaps between cell-periodic parts of the exciton wavefunction at neighboring **Q**-pts which we denote

$$M_{SS'}(\mathbf{Q}, \mathbf{B}) = \langle F_{S\mathbf{Q}} | F_{S'\mathbf{Q}+\mathbf{B}} \rangle$$

$$M_{SS'}(\mathbf{Q}, \mathbf{B}) = \sum_{\substack{cv\mathbf{k} \\ c'v'\mathbf{k}'}} [A^{S'\mathbf{Q}}_{c'v'\mathbf{k}'}]^{\star} A^{S\mathbf{Q}+\mathbf{B}}_{cv\mathbf{k}} \times$$

$$\left[\int_{\text{xtal}} d\mathbf{r}_e e^{-i(\mathbf{k}'-\mathbf{k})\cdot\mathbf{r}_e} u^{\star}_{c'\mathbf{k}'+\mathbf{Q}/2}(\mathbf{r}_e) u_{c\mathbf{k}+\mathbf{Q}/2+\mathbf{B}/2}(\mathbf{r}_e)\right] \left[\int_{\text{xtal}} d\mathbf{r}_h e^{i(\mathbf{k}'-\mathbf{k})\cdot\mathbf{r}_h} u_{v'\mathbf{k}'-\mathbf{Q}/2}(\mathbf{r}_h) u^{\star}_{v\mathbf{k}-\mathbf{Q}/2-\mathbf{B}/2}(\mathbf{r}_h)\right]$$

The integral over $\mathbf{r}_e$ and $\mathbf{r}_h$ give delta functions in $\mathbf{k}$ and $\mathbf{k}'$ so that

$$M_{SS'}(\mathbf{Q},\mathbf{B}) = \sum_{cc'vv'\mathbf{k}} [A^{S'\mathbf{Q}}_{c'v'\mathbf{k}}]^\star A^{S\mathbf{Q}+\mathbf{B}}_{cv\mathbf{k}} \left\langle u_{c'\mathbf{k}+\mathbf{Q}/2} | u_{c\mathbf{k}+\mathbf{Q}/2+\mathbf{B}/2}\right\rangle \left\langle u_{v\mathbf{k}-\mathbf{Q}/2-\mathbf{B}/2} | u_{v'\mathbf{k}-\mathbf{Q}/2}\right\rangle$$

To run Wannier90 we also need to make some initial guess for the localized Wannier orbitals, which we denote $H_J(\mathbf{R},\mathbf{r})$, and project this guess onto unperturbed Bloch exciton orbital $\Psi_{S\mathbf{Q}}(\mathbf{R},\mathbf{r})$, we denote this projection

$$A_{SJ}(\mathbf{Q}) = \langle \Psi_{S\mathbf{Q}} | H_J \rangle \,.$$

Our initial guess, $H_J(\mathbf{R},\mathbf{r})$, is related to its Fourier transform, $H^{J\mathbf{Q}}_{\mathbf{k}}$, through

$$H_J(\mathbf{R},\mathbf{r}) = \sum_{\mathbf{kQ}} H^{J\mathbf{Q}}_{\mathbf{k}} e^{i\mathbf{k}\cdot\mathbf{r}} e^{i\mathbf{Q}\cdot\mathbf{R}}.$$

The same function can be re-expressed in the electron and hole coordinate $H_J(\mathbf{r}_r,\mathbf{r}_h)$ takes the form

$$H_J(\mathbf{r}_e,\mathbf{r}_h) = \sum_{\mathbf{kQ}} H^{J\mathbf{Q}}_{\mathbf{k}} e^{i(\mathbf{k}+\mathbf{Q}/2)\cdot\mathbf{r}_e} e^{-i(\mathbf{k}-\mathbf{Q}/2)\cdot\mathbf{r}_h}.$$

Using these definitions

$$\begin{aligned}
A_{SJ}(\mathbf{Q}) &= \sum_{cv\mathbf{k}\mathbf{k}'\mathbf{Q}'} [A^{S\mathbf{Q}}_{cv\mathbf{k}}]^\star H^{J\mathbf{Q}'}_{\mathbf{k}'} \left\langle \psi_{c\mathbf{k}+\mathbf{Q}/2} | \mathbf{k}'+\mathbf{Q}'/2\right\rangle \left\langle \mathbf{k}'-\mathbf{Q}'/2 | \psi_{v\mathbf{k}+\mathbf{Q}/2}\right\rangle \\
&= \sum_{cv\mathbf{k}\mathbf{k}'\mathbf{Q}'} [A^{S\mathbf{Q}}_{cv\mathbf{k}}]^\star H^{J\mathbf{Q}'}_{\mathbf{k}'} \sum_{\mathbf{G}_e\mathbf{G}_h} c^\star_{c\mathbf{k}+\mathbf{Q}/2}(\mathbf{G}_e) c_{v\mathbf{k}-\mathbf{Q}/2}(\mathbf{G}_h)\; \delta_{\mathbf{k}+\mathbf{Q}/2+\mathbf{G}_e,\mathbf{k}'+\mathbf{Q}'/2}\; \delta_{\mathbf{k}-\mathbf{Q}/2+\mathbf{G}_h,\mathbf{k}'-\mathbf{Q}'/2},
\end{aligned}$$

where $\psi_{n\mathbf{k}}(\mathbf{r}) = \sum_{\mathbf{G}} c_{n\mathbf{k}}(\mathbf{G}) e^{i(\mathbf{k}+\mathbf{G})\cdot\mathbf{r}}$ with $\mathbf{G}$ denoting a reciprocal lattice vector. The delta functions enforce the condition

$$\begin{aligned}
\mathbf{k}' &= \mathbf{k} + \mathbf{G}_{ave} \\
\mathbf{Q}' &= \mathbf{Q} + \mathbf{G}_{rel}
\end{aligned}$$

where $\mathbf{G}_{ave} = (\mathbf{G}_e + \mathbf{G}_h)/2$ and $\mathbf{G}_{rel} = \mathbf{G}_e - \mathbf{G}_h$. Our final expression is then

$$\langle \Psi_{S\mathbf{Q}} | H_J \rangle = \sum_{cv\mathbf{k}} [A^{S\mathbf{Q}}_{cv\mathbf{k}}]^\star \sum_{\mathbf{G}_{ave}\mathbf{G}_{rel}} H^{J\mathbf{Q}+\mathbf{G}_{rel}}_{\mathbf{k}+\mathbf{G}_{ave}} c^\star_{c\mathbf{k}+\mathbf{Q}/2}(\mathbf{G}_{ave} + \mathbf{G}_{rel}/2) c_{v\mathbf{k}-\mathbf{Q}/2}(\mathbf{G}_{ave} - \mathbf{G}_{rel}/2). \tag{A.2}$$

Up to this point, everything have been general, now we assume that $H^J(\mathbf{R},\mathbf{r})$ is separable in average and relative coordinates so that $H^J(\mathbf{R},\mathbf{r})$ can be written in the form

$$H^J(\mathbf{R},\mathbf{r}) = f^{j_1}(\mathbf{R}) g^{j_2}(\mathbf{r}),$$

where J is understood to be a composite index which uniquely identifies each j_1, j_2 pair, symbolically $J = (j_1, j_2)$. It follows immediately

$$H^{J\mathbf{Q}+\mathbf{G}_{rel}}_{\mathbf{k}+\mathbf{G}_{ave}} = f^{j_1}_{\mathbf{Q}+\mathbf{G}_{rel}} g^{j_2}_{\mathbf{k}+\mathbf{G}_{ave}},$$

where

$$f^{j}_{\mathbf{k}} = \int f^{j}(\mathbf{r}) e^{-i\mathbf{k}\cdot\mathbf{r}} d^3\mathbf{r}.$$

In this work we take $f^j(\mathbf{r})$ to be hydrogenic in form

$$f^j(\mathbf{r}) = \frac{1}{\sqrt{\pi a^3}} e^{-r/a},$$

as discussed in the main text.

A.2 Multiband Lang-Firsov Polaron Transformation

To derive the explicit form of $\mathcal{H}^{\rm pol}$, it is sufficient to consider how each operator in $\mathcal{H}^W$ transforms under the similarity transform introduced in Eq. 4.9. We find

$$\begin{aligned} e^{\mathcal{S}} c^\dagger_{m\mathbf{R}} e^{-\mathcal{S}} &= c^\dagger_{m\mathbf{R}} \theta^\dagger_{m\mathbf{R}} \\ e^{\mathcal{S}} b^\dagger_{\mathbf{q}\nu} e^{-\mathcal{S}} &= b^\dagger_{\mathbf{q}\nu} - \sum_{m\mathbf{R}} c^\dagger_{m\mathbf{R}} c_{m\mathbf{R}} \frac{e^{i\mathbf{q}\cdot\mathbf{R}} \mathcal{G}^W_{mm\nu}(\mathbf{0},\mathbf{q})}{\omega_{\mathbf{q}\nu}}, \end{aligned} \tag{A.3}$$

where

$$\theta^\dagger_{m\mathbf{R}} = \exp\left[-\frac{1}{N_{\mathbf{q}}} \sum_{\nu\mathbf{q}} \frac{e^{-i\mathbf{q}\cdot\mathbf{R}} \mathcal{G}^W_{mm\nu}(\mathbf{0},\mathbf{q})}{\omega_{\mathbf{q}\nu}} \right]. \tag{A.4}$$

After these transformations the polaron Hamiltonian reads

$$\begin{aligned} \mathcal{H}^{\rm pol} = & \sum_{nm\mathbf{R}\mathbf{R}'} V_{mn}(\mathbf{R}-\mathbf{R}') c^\dagger_{m\mathbf{R}} c_{n\mathbf{R}'} \theta^\dagger_{m\mathbf{R}} \theta_{n\mathbf{R}'} \\ & + \sum_{\mathbf{q}\nu} \omega_{\mathbf{q}\nu} \left(b^\dagger_{\mathbf{q}\nu} - \sum_{m\mathbf{R}} c^\dagger_{m\mathbf{R}} c_{m\mathbf{R}} \frac{e^{i\mathbf{q}\cdot\mathbf{R}} \mathcal{G}^W_{mm\nu}(\mathbf{0},\mathbf{q})}{\omega_{\mathbf{q}\nu}} \right) \left(b_{\mathbf{q}\nu} - \sum_{m\mathbf{R}} c^\dagger_{m\mathbf{R}} c_{m\mathbf{R}} \frac{e^{-i\mathbf{q}\cdot\mathbf{R}} \mathcal{G}^W_{mm\nu}(\mathbf{0},\mathbf{q})}{\omega_{\mathbf{q}\nu}} \right) \\ & + \sum_{mn\mathbf{R}\mathbf{R}'\mathbf{q}\nu} e^{-i\mathbf{q}\cdot\mathbf{R}} \mathcal{G}^{\rm W}_{mn\nu}(\mathbf{R}-\mathbf{R}',\mathbf{q}) c^\dagger_{m\mathbf{R}} c_{n\mathbf{R}'} \theta^\dagger_{m\mathbf{R}} \theta_{n\mathbf{R}'} \\ & \times \left(b^\dagger_{-\mathbf{q}\nu} + b_{\mathbf{q}\nu} - 2 \sum_{m\mathbf{R}} c^\dagger_{m\mathbf{R}} c_{m\mathbf{R}} \frac{e^{-i\mathbf{q}\cdot\mathbf{R}} \mathcal{G}^W_{mm\nu}(\mathbf{0},\mathbf{q})}{\omega_{\mathbf{q}\nu}} \right), \end{aligned} \tag{A.5}$$

where

$$\theta^\dagger_{m\mathbf{R}} \theta_{n\mathbf{R}'} = \exp\left[\frac{1}{N_{\mathbf{q}}} \sum_{\mathbf{q}\nu} e^{-i\mathbf{q}\cdot\mathbf{R}'} \frac{\mathcal{G}_{nn\nu}(\mathbf{0},\mathbf{q}) - \mathcal{G}_{mm\nu}(\mathbf{0},\mathbf{q}) e^{-i\mathbf{q}\cdot(\mathbf{R}-\mathbf{R}')}}{\omega_{\mathbf{q}\nu}} (b_{\mathbf{q}\nu} - b^\dagger_{-\mathbf{q}\nu}) \right]. \tag{A.6}$$

When only local exciton-phonon coupling terms are retained, a cancellation occurs and $\mathcal{H}^{\mathrm{pol}}$ reduces to

$$\mathcal{H}^{\mathrm{pol}} = \sum_{nm\mathbf{R}\mathbf{R}'} V_{mn}(\mathbf{R}-\mathbf{R}')d^{\dagger}_{m\mathbf{R}}d_{n\mathbf{R}'} + \sum_{\mathbf{q}\nu}\omega_{\nu\mathbf{q}}b^{\dagger}_{\mathbf{q}\nu}b_{\mathbf{q}\nu} - \sum_{m\mathbf{R}}\Delta_{m\mathbf{R}}d^{\dagger}_{m\mathbf{R}}d_{m\mathbf{R}}, \tag{A.7}$$

where $d^{\dagger}_{m\mathbf{R}} = \theta_{m\mathbf{R}} = \theta^{\dagger}_{m\mathbf{R}}c^{\dagger}_{m\mathbf{R}}$.

A.3 Connection Between the Semiconductor Bloch Equations and Analytic Expressions for the Exciton Lineshape

The absorption spectrum can be calculated from the time-propagation results of the $\mathbf{Q}=0$ exciton polarizaiton under a delta function pulse. We introduce the light-exciton coupling term in the exciton basis,

$$H_L(t) = -e\mathbf{E}(t)\cdot\sum_{S}\left(\mathbf{\Omega}^{S}P^{S\dagger}_{\mathbf{0}} + \mathbf{\Omega}^{S*}P^{S}_{\mathbf{0}}\right), \tag{A.8}$$

where $\Omega^{S} \equiv \sum_{cv\mathbf{k}} d_{cv\mathbf{k}}\psi^{S*}_{cv\mathbf{k}}$ is the optical transition operator in the exciton basis with the optical transition matrix element $d_{cv\mathbf{k}}$ in the Kohn-Sham basis. The full equation of motion with the off-diagonal self-energy is written as

$$\frac{\partial P^{S}_{\mathbf{0}}}{\partial t} = \frac{1}{i\hbar}\left(E_{S\mathbf{0}} - i\gamma + \Sigma_{S\lambda\mathbf{0}}\right)P^{\lambda}_{\mathbf{0}} + \frac{1}{i\hbar}e\mathbf{E}(t)\cdot\mathbf{\Omega}^{S}. \tag{A.9}$$

where summation over the λ index is understood. Diagonalizing the following Hamiltonian:

$$H_{SS'} = E_{S\mathbf{0}}\delta_{SS'} + \Sigma_{SS'} \tag{A.10}$$

we obtain renormalized eigenvectors and rotation matrices T, we can use the later to rotate the semiconductor Bloch equations into the exciton-phonon basis to find:

$$\frac{\partial \tilde{P}^{S}_{\mathbf{0}}}{\partial t} = \frac{1}{i\hbar}\left(\tilde{E}_{S\mathbf{0}} + i\tilde{\Gamma}_{S\mathbf{0}}\right)\tilde{P}^{S}_{\mathbf{0}} + \frac{1}{i\hbar}e\mathbf{E}(t)\cdot\tilde{\mathbf{\Omega}}^{S}.$$

Fourier transforming and solving for $\tilde{P}^{S}_{\mathbf{0}}(\omega)$:

$$\tilde{P}^{S}_{\mathbf{0}}(\omega) = \frac{e\widetilde{\Omega^{S}}E}{\left(\hbar\omega - \tilde{E}_{S\mathbf{0}} - i\tilde{\Gamma}_{S\mathbf{0}}\right)}. \tag{A.11}$$

The total polarization is computed by

$$\begin{aligned}P_{tot}(\omega) &= e\sum_S \left(\Omega^{S*}P^S(\omega) + \Omega^S P^{S*}(\omega)\right)\\ &= e\sum_S \left(\tilde{\Omega}^{S*}\tilde{P}^S(\omega) + \tilde{\Omega}^S \tilde{P}^{S*}(\omega)\right)\end{aligned}$$

Plugging in, we find:

$$\epsilon_2(\omega) = \mathrm{Im}\frac{P_{tot}(\omega)}{\epsilon_0 E} = \frac{\pi e^2}{\hbar\epsilon_0}\mathrm{Im}\left[\sum_S \frac{(\Omega^* T)_S (T^{-1}\Omega)_S}{\hbar\omega - \tilde{E}_S - i\tilde{\Gamma}_S}\right] \tag{A.12}$$

$$= \frac{\pi e^2}{\hbar\epsilon_0}\sum_S \mathrm{Re}[(\Omega^* T)_S (T^{-1}\Omega)_S]\frac{\tilde{\Gamma}_S}{(\omega - \tilde{E}_S)^2 + \tilde{\Gamma}_S^2} + \mathrm{Im}[(\Omega^* T)_S (T^{-1}\Omega)_S]\frac{\omega - \tilde{E}_S}{(\omega - \tilde{E}_S)^2 + \tilde{\Gamma}_S^2} \tag{A.13}$$

A result previously derived by Toyozawa, which clearly shows the symmetric and asymmetric contributions to the exciton absorption. We have numerically verified that $\epsilon_2(\omega)$ computed with this expression and via propagation of the semiconductor Bloch equations, gives the same result. Finally to connect with Eqn. 4 of the main text we note that the rotation matrices T can be used to rotate the energy denominator appearing above back to the exciton basis, explicitly:

$$\sum_S (\Omega^* T)_S \frac{1}{\hbar\omega - \tilde{E}_S - i\tilde{\Gamma}_S}(T^{-1}\Omega)_S = \sum_{\lambda\lambda'}\Omega^*_\lambda \frac{1}{\omega - E_\lambda\delta_{\lambda\lambda'} - \mathrm{Re}\Sigma_{\lambda\lambda'} + i\Gamma_{\lambda\lambda'}}\Omega_{\lambda'}$$

Taking this as our staring point we find:

$$\begin{aligned}\epsilon_2(\omega) &= \frac{\pi e^2}{\hbar\epsilon_0}\mathrm{Im}\left[\sum_{\lambda\lambda'}\Omega^*_\lambda \frac{1}{\omega - E_\lambda\delta_{\lambda\lambda'} - \mathrm{Re}\Sigma_{\lambda\lambda'} + i\Gamma_{\lambda\lambda'}}\Omega_{\lambda'}\right]\\ &\approx \frac{\pi e^2}{\hbar\epsilon_0}\sum_{\lambda\lambda'}\Omega^*_\lambda \frac{1}{\omega - E_\lambda - \mathrm{Re}\Sigma_\lambda - i\Gamma_\lambda}\Gamma_{\lambda\lambda'}\frac{1}{\omega - E_{\lambda'} - \mathrm{Re}\Sigma_{\lambda'} + i\Gamma_{\lambda'}}\Omega_{\lambda'}\\ &= \frac{\pi e^2}{\hbar\epsilon_0 N_{\mathbf{q}}}\sum_{S\nu\mathbf{q}}\left|\sum_\lambda \frac{G_{S\lambda\nu}(0,\mathbf{q})\Omega_\lambda}{\omega - E_\lambda - \ \mathrm{Re}\Sigma_\lambda - i\Gamma_\lambda}\right|^2 \delta(\omega - E_{S\mathbf{q}} \mp \omega_{\nu q})\end{aligned}$$

where in going from line 1 to 2, we have dropped off-diagonal terms in the denominator (while retaining them in the numerator). In the last step we used the definition of $\Gamma_{\lambda\lambda'}$:

$$\Gamma_{\lambda\lambda'} = \frac{1}{N_{\mathbf{q}}}\sum_{n\nu,\mathbf{q}} G^*_{n\lambda\nu}(0,\mathbf{q})G_{n\lambda'\nu}(0,\mathbf{q})\left(\frac{1}{2} \pm \frac{1}{2} + N_{\nu\mathbf{q}}\right)\delta(\omega - E_{n\mathbf{q}} \mp \hbar\omega_{\nu\mathbf{q}})$$

no approximation is made in this step. As emphasized above, this term can be conveniently interpreted with second order perturbation theory. In the diagonal approximation we consider terms with $\lambda = \lambda'$ and obtain,

$$\begin{aligned}\epsilon_2^{\text{diag}}(\omega) &\approx \frac{\pi e^2}{\hbar\epsilon_0}\sum_\lambda \Omega_\lambda^* \frac{1}{\omega - E_\lambda - \text{Re}\Sigma_\lambda - i\Gamma_\lambda}\Gamma_{\lambda\lambda}\frac{1}{\omega - E_\lambda - \text{Re}\Sigma_\lambda + i\Gamma_\lambda}\Omega_\lambda \\ &= \frac{\pi e^2}{\hbar\epsilon_0 N_{\mathbf{q}}}\sum_{S\nu\mathbf{q}}\sum_\lambda \left|\frac{G_{S\lambda\nu}(0,\mathbf{q})\Omega_\lambda}{\omega - E_\lambda - \ \text{Re}\Sigma_\lambda - i\Gamma_\lambda}\right|^2 \delta(\omega - E_{S\mathbf{q}} \mp \omega_{\nu\mathbf{q}}).\end{aligned}$$

Equivalently, we can plug $T = I$, $\tilde{E}_S = E_S$, $\tilde{\Gamma}_S = \Gamma_S$ into the Eq. A.13 and get the usual Lorentzian spectrum

$$\epsilon_2^{\text{diag}}(\omega) \approx \frac{\pi e^2}{\hbar\epsilon_0}\sum_S |\Omega_S|^2 \frac{\Gamma_S}{(\omega - E_S)^2 + \Gamma_S^2}.$$

Comparing the diagonal approximation with the full expression, we can see the difference from the interference effects due to the cross terms discussed above text.